GEOPHYSICAL INVESTIGATIONS OF FAULT SYSTEMS NEAR CADIZ, CALIFORNIA AND THEIR IMPACT ON THE HYDROLOGY OF BONANZA SPRINGS

A Thesis

Presented to the

Faculty of

California State Polytechnic University, Pomona

In Partial Fulfillment

Of the Requirements for the Degree

Master of Science

In

Geology

By

Peter Flores

2020

SIGNATURE PAGE

THESIS:	GEOPHYSICAL INVESTIGATIONS OF FAULT SYSTEMS NEAR CADIZ, CALIFORNIA AND THEIR IMPACT ON THE HYDROLOGY OF BONANZA SPRINGS
AUTHOR:	Peter Flores
DATE SUBMITTED:	Spring 2020
	Department of Geological Sciences

Dr. Jascha Polet _____
Thesis Committee Chair
Geological Sciences

Dr. Stephen Osborn _____
Geological Sciences

Dr. Nick Van Buer _____
Geological Sciences

ABSTRACT

Bonanza Springs is one of several oases in the eastern Mojave that rely on aquifer systems fed by long term precipitation recharge. Many desert species depend on the spring as it acts as one of the few watering spots for the region. There are currently plans to extract groundwater from the Fenner Valley alluvial aquifer, approximately 15 km to the south of the spring. A previous report has suggested that two fault zones, one trending northeast and the other northwest, meet at Bonanza Springs, creating a hydrologic disconnect between the aquifer to the north feeding the spring and the aquifer in the Fenner Valley. However, there is limited literature available on the geology of the area and no detailed geophysical surveys have been performed. This study aims to enhance our understanding of the subsurface structure in the area and better assess the effects groundwater extraction would have on Bonanza Springs. To investigate the presence of the two proposed fault zones, several geophysical surveying techniques were employed, including ground based magnetics, VLF (Very Low Frequency), and DC (Direct Current) resistivity surveys. Total magnetic field intensity surveys were performed within the study area around Bonanza Springs, while numerous VLF profiles were measured across the proposed northwest and northeast trending fault lines. Magnetic anomalies suggest the presence of a linear feature corresponding with the mapped location of the northwest trending fault. Anomalies in the VLF data across the northwest trending fault indicate several highs that correlate with the linear feature in the magnetic data. Conversely, magnetic and VLF data show no features that would correspond to the presence of the northeast trending fault. Resistivity surveying across the northeast trending fault observed a continuous zone of low resistivity at approximately 5 m of depth interpreted as the groundwater table. There is no apparent offset in the resistivity data that would suggest the presence of a hydraulic barrier. Lack of responses in the VLF and magnetic data and the absence of groundwater offset from resistivity surveying along and across the northeast trending fault suggest no hydraulic disconnect at Bonanza Springs between the aquifer system feeding the spring and the alluvial aquifer to the south.

Table of Contents

List of Figures

List of Tables

1 Introduction

The Mojave is an arid desert occupying approximately 125,000 km^2 and spanning south-eastern California and southern Nevada. Averaging roughly 2-3 inches of rain a year (although 4-7 inches is not uncommon in particularly wet years), it is considered the driest desert in North America. Due to this arid climate, there exists a common perception of the Mojave Desert as an oppressive and desolate landscape devoid of life. This is perhaps an unfair and certainly untrue perspective. The Mojave is home to many different species of flora and fauna, with over 200 plant species specifically endemic to the region (Stermer & Matull, 2003). Many of these desert species rely on natural springs and oases found throughout the Mojave that often act as the only sources of water in an otherwise arid environment. One of these natural watering areas is Bonanza Springs. Located in the eastern Mojave, Bonanza Springs offers fresh water resources to many riparian plant species and acts as a rare watering spot for Mojave desert wildlife. There has been little study in this area and a greater understanding of the geologic and hydrologic structures behind springs like Bonanza is necessary to recognize any potential impacts against such a limited resource.

1.1 Bonanza Springs

Bonanza Springs is one of several natural spring-fed oases in the eastern Mojave desert, located approximately 150 km southeast of Barstow, adjacent to the unincorporated community of Cadiz (Figure 1). A diverse array of desert species is dependent upon the existence of the spring as it acts as one of the few natural watering spots and riparian environments for the region. The spring is bounded by a small mountain range to its immediate north and a large alluvial valley, the Fenner Valley, 15 km to its south (Figure 2). Beneath the Fenner Valley is a large alluvial aquifer system with an estimated storage capacity between 17 and 34 million acre-feet (SMWD, 2011). Due to the presence of this

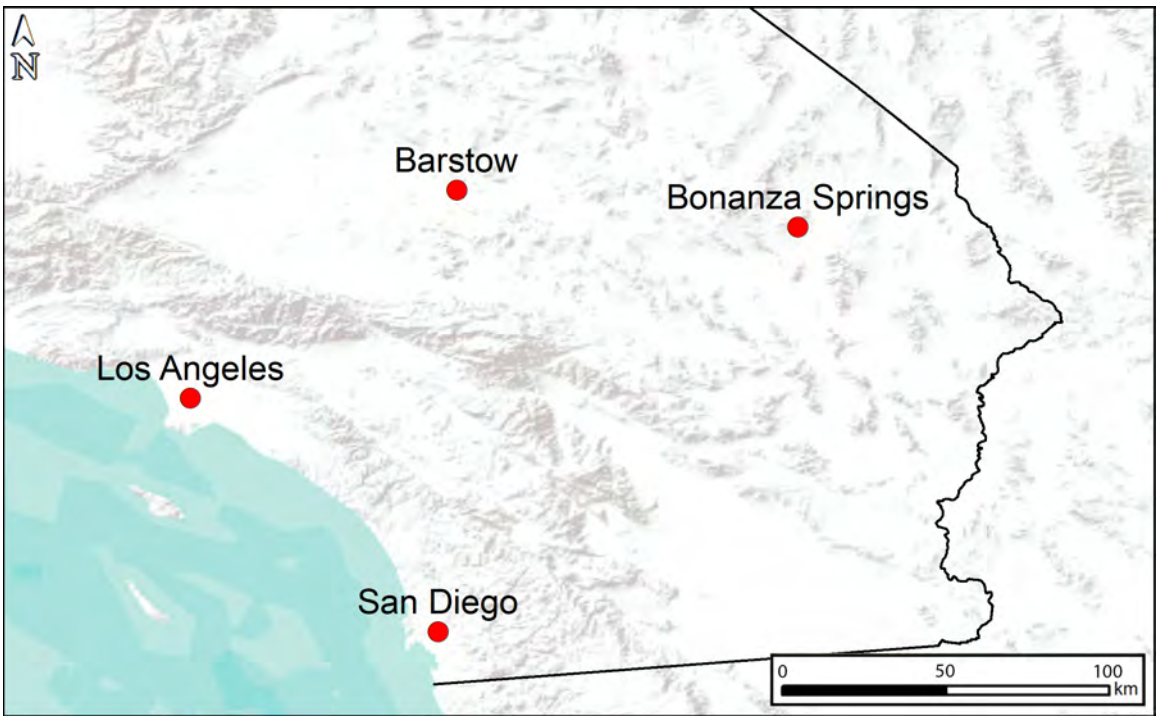

Figure 1: Relief map of Southern California showing the location of Bonanza Springs relative to major cities.

large, previously untapped, aquifer system, there have been proposals from a private natural resources company, Cadiz Inc., to extract groundwater from the Fenner Valley aquifer and sell it to southern California water providers for urban use. An environmental impact report was issued by Cadiz Inc., hereafter referred to as the Cadiz Report (Kenney & Foreman, 2018), on the effects any drawdown on the alluvial aquifer will have on the spring. However, limited geologic studies or geophysical surveys have been conducted of the immediate area: two United States Geological Survey (USGS) field reports of adjacent areas (Miller & Yount, 2002; Miller et al., 2007) and several technical documents associated with the project (Foreman, 2010; SMWD, 2011; Brown, 2013; Kenney & Foreman, 2018). The goal of this study is to increase our knowledge of the subsurface structure in the area around Bonanza Springs to help address the question what effect, if any, groundwater drawdown may have on the springs itself.

1.1.1 Cadiz Water Project

Cadiz Inc. is a private natural resources company that owns approximately 160 km^2 of land in and around Cadiz (Figure 2). Currently they maintain a small agricultural field that is sustained by small scale pumping, but since 2001 the company has had plans to extract significant volumes of groundwater from the Fenner Valley aquifer for sale to local water districts and municipalities. The Cadiz Valley Water Conservation, Recovery, and Storage Project, as it is officially called, would be a large scale operation with the goal of extraction up to 50,000 acre-feet per year of groundwater from the alluvial aquifer system and selling the water to water agencies such as the Metropolitan Water District and the Santa Margarita Water District among other Southern California water Agencies (SMWD, 2011). The company asserts that large amounts of groundwater are lost to evaporation and that the Cadiz Water Project would instead use that water to serve urban areas (Kenney & Foreman, 2018). They estimate that extracted groundwater from the project would provide water for an estimated 400,000 people per year in Southern California. To address worries the water project would negatively impact the natural desert springs that may rely on this

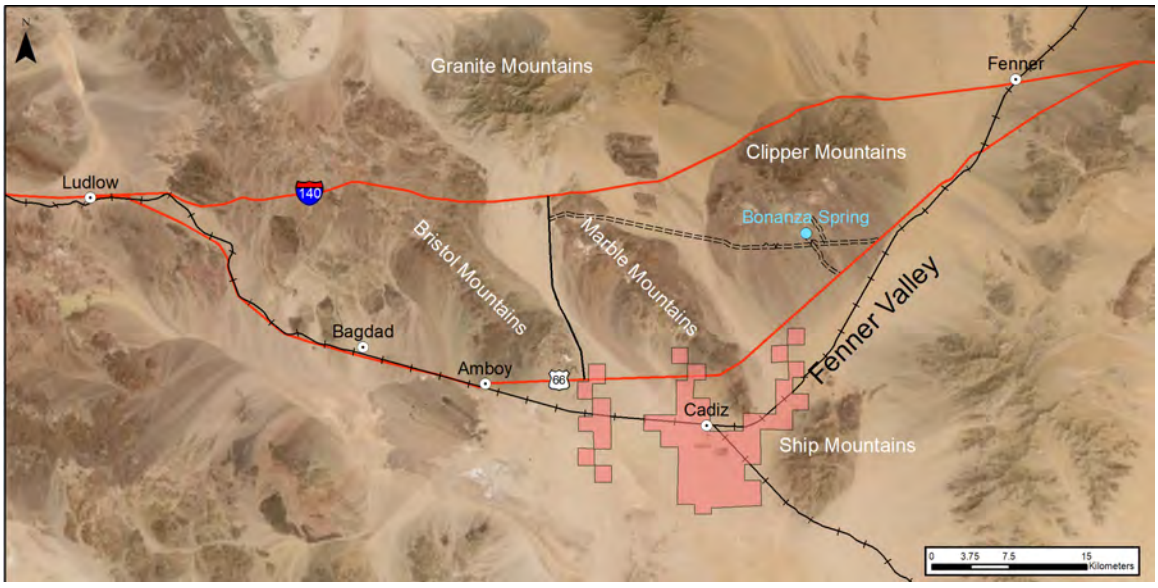

Figure 2: Satellite map of Bonanza Springs and the surrounding area. Red polygons to the south of the spring represent areas of private land owned by Cadiz, Inc. Location of private property from Kenney and Foreman (2018).

groundwater, Cadiz Inc. has issued a report, the Bonanza Springs Impact Assessment Report (Kenney & Foreman, 2018), that examined the local hydrology of Bonanza Springs and how groundwater recharges, travels through the subsurface, and any expected impacts pumping will have on the spring.

1.2 Geology and Tectonic Setting

Bonanza Springs is located in the Basin and Range Geomorphic Province within the eastern California Shear zone. The spring itself is situated on the southern flank of the Clipper Mountains with igneous rock units associated with Miocene aged extensional tectonics, typical of this area, exposed throughout. Numerous faults, jointing, and fractures have been mapped as part of an environmental impact review issued by Cadiz Inc. (Figure 3). The faults as identified and mapped in the area by Kenney and Foreman (2018), are left-lateral strike-slip that exhibit near vertical dips. They trend mostly in a northwest-southeast direction, and are likely associated with shear resulting from block rotation occurring during regional extension and crustal thinning (Miller & Yount, 2002). About a dozen of these fault zones show evidence of Quarternary movement in the areas around Cadiz and the Fenner Valley (Brown, 2013). In addition to the faults and fractures mapped via field site visits, the Cadiz Report also identified potential faults and fractures from aerial imagery. The Cadiz Report identified several geologic units in the southern Clipper Mountains around the spring. Currently, there exists little literature on the area to provide corroborating ages or rock descriptions. The authors of the Cadiz Report, instead, correlated earlier documents on adjacent areas with field observations to determine rock units for their study; specifically a USGS geologic map of the East Mojave National Scenic Area (Miller et al., 2007), the southern most extent of which includes the northern edge of the Clipper Mountains, and a USGS field report on the Fort Irwin area (Miller & Yount, 2002) to the north of the spring.

There are three primary groups of rock units in the Bonanza Springs area: alluvial aquifer units, subvolcanic igneous intrusive rocks, and younger Miocene aged igneous ex-

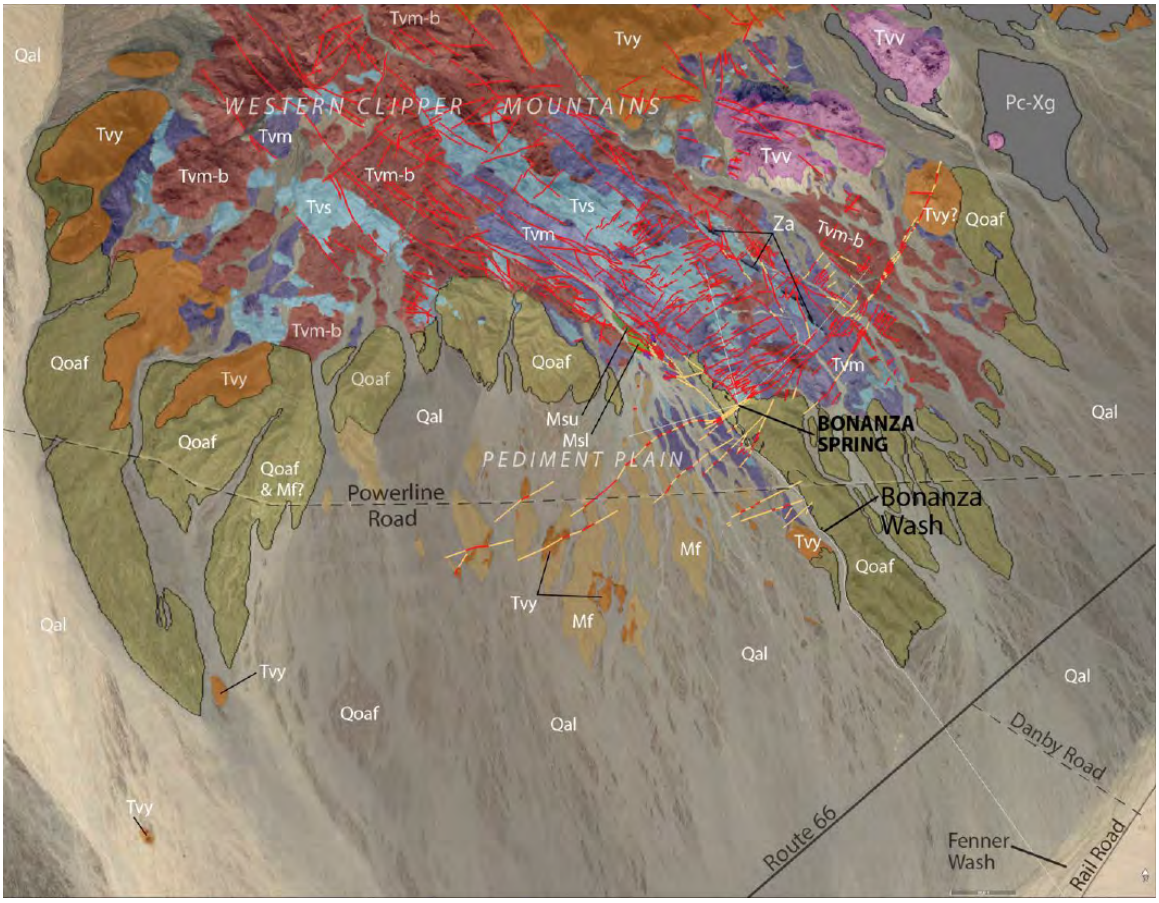

Figure 3: Geologic map of Bonanza Springs and the surrounding Western Clipper Mountains. Red lines indicate faults and fractures observed in the field. Yellow lines represent faults or fractures projected from imagery data. From Kenney and Foreman (2018).

trusive rocks. Both the older and younger sedimentary alluvium make up the primary alluvial aquifer unit. The igneous extrusive units are grouped as mafic basalt flows and silicic rhyolite ashfall tuffs, while the igneous intrusive units are basalt and gabbro tabular intrusive bodies, vents, and dikes emplaced at very shallow depths of less than 1 km. These shallowly emplaced units appear within the Clipper Mountains region and do not extend into the Fenner Valley. According to a 2007 USGS mineral study of the northern Clipper mountains, most of the Miocene igneous activity occurred after the deposition of the Peach Springs tuff, putting the age range of the oldest igneous extrusive layer at approximately 18.5-20 Ma (Miller et al., 2007). Further to the southwest extending into the Fenner Valley, there is a thin Miocene aged sedimentary unit interbedded at depth with the igneous extru-

sive unit that continues into the valley as a potentially mixed sedimentary and igneous unit. These interbedded units are further overlain by younger alluvium basin fill that serves as the primary alluvial aquifer unit for the Fenner Valley aquifer.

The geology of the aquifer bearing units in the valley below can be broken up into three sections: an upper (younger) alluvial aquifer; a lower (older) alluvial aquifer; and a bedrock aquifer consisting of Tertiary fanglomerate, and fractured and faulted granitic rock (SMWD, 2011). The upper alluvial aquifer is composed of stream deposited Quaternary sediments ranging in depth from 60-250 m. The lower alluvial aquifer consists of older sediments made up of interbedded sand, gravel, silt, and clay that likely extends to a depth of 1.8 km. The third aquifer unit lies beneath the older alluvial aquifer fill where exploratory wells have found groundwater. Groundwater storage in this third aquifer unit is likely due to secondary porosity features from fractured bedrock.

1.3 Hydrogeology of Bonanza Springs

The Cadiz Report examined the field geology of the area around Bonanza Springs and is responsible for much of the knowledge of the local geology. The report determined that Bonanza Springs is being recharged from a catchment basin that exists in the Clipper Mountains just north of the spring itself. The basin is bounded to its north and south by a zone of northwest-southeast trending faults that follows the general orientation of faults and fractures in the Mojave Desert area. These bounding zones were identified and determined via field observation and mapping of the field site area around Bonanza Springs and the Clipper Mountains. The report also asserts that there exists an additional fault zone bounding the basin at its southeast that is composed of northeast-southwest trending faults and fractures (Figure 4). This fault zone, however, was identified via projection of potential fault zone locations that trend perpendicular to the majority of mapped faults in the area. Some of the geologic structures in the area (geologic units, dikes, potential faults) were not mapped during field site visits, but rather via aerial imagery observations done using

Google Earth Pro (Kenney & Foreman, 2018).

Within the area of Bonanza Springs, there are three principal water bearing units as described in an earlier section. Groundwater movement through the alluvial sedimentary units is controlled by primary porosity, while movement through the two intrusive and extrusive units are controlled by secondary porosity. While the alluvial units are the primary water bearing units within the Fenner Valley, closer to Bonanza Springs they are more like zones of variable saturation. As would be expected, the alluvial unit has high transmissivity and hydraulic conductivity values that range from a few feet per day to tens of feet per day (Kenney & Foreman, 2018). The hydrological parameters of the extrusive unit are unknown, as the report indicates that no sampling has been done at that layer. However, it is noted from the literature that transmissivity values for slightly fractured to highly fractured volcanics commonly range from 10s to 1,000s of ft^2 per day (Krásny & Sharp Jr, 2007).

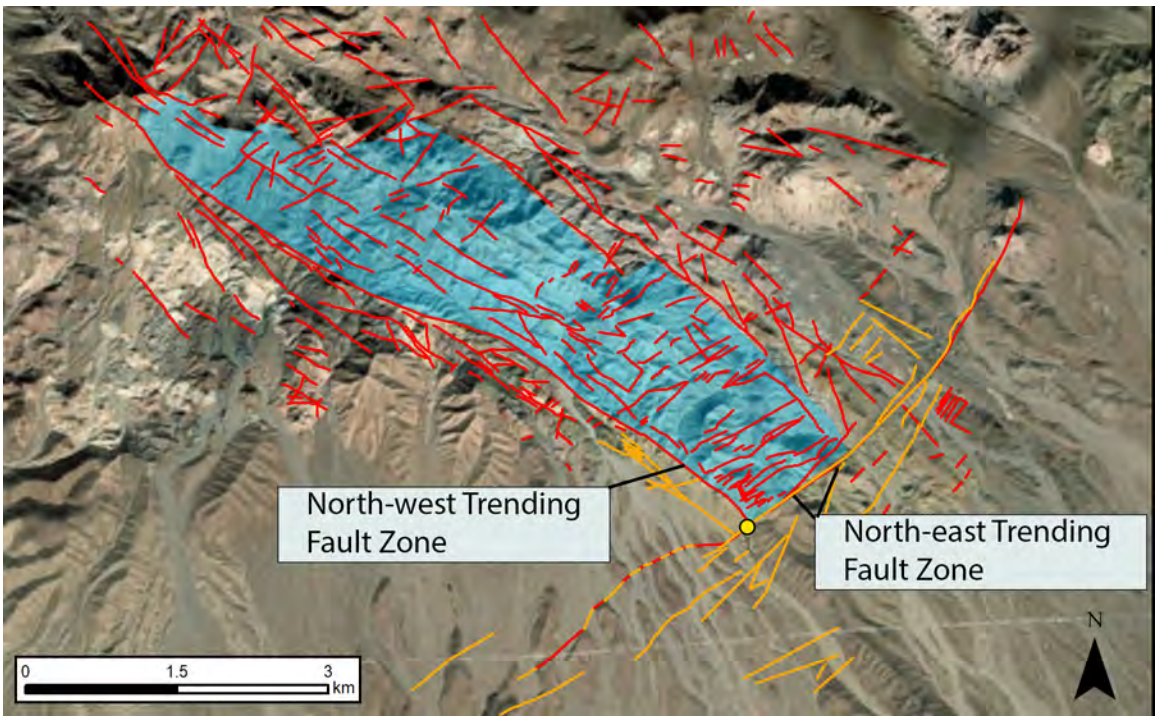

Figure 4: Map of the area around Bonanza Springs indicating the presence and locations of the catchment basin and fault bounding zones. Blue area indicates the area of the catchment basin. Yellow dot is the location of the spring. Red lines are faults and fractures mapped from field observations while yellow lines represent projected faults or fractures based on observations of satellite imagery made as part of the Cadiz Report. Adapted from Kenney and Foreman (2018).

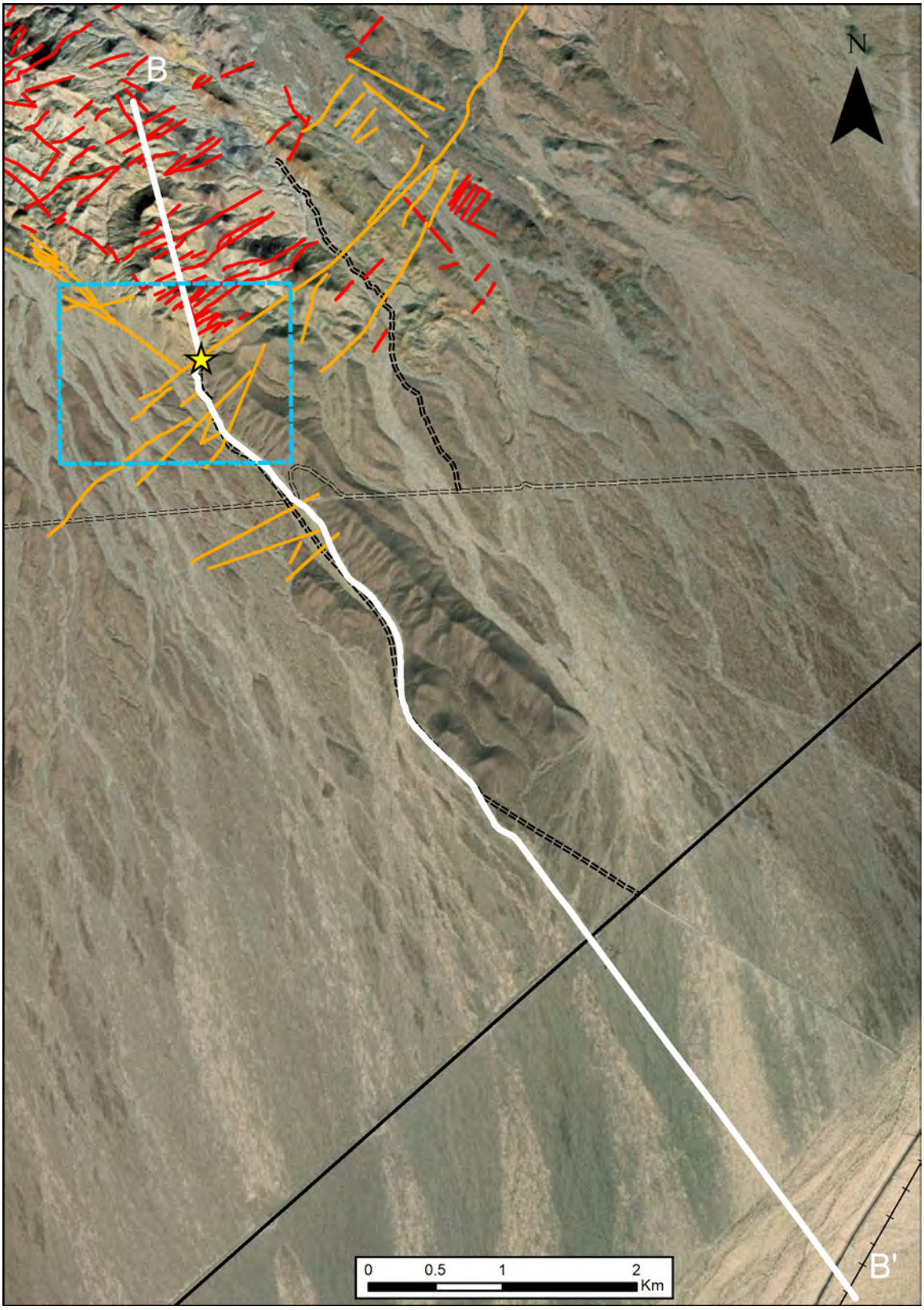

Figure 5: Map of Bonanza Springs and surrounding area. Numerous faults, jointing, and fractures have been mapped as part of an environmental impact review issued by Cadiz Inc. (Kenney & Foreman, 2018). Red lines identify fractures and faults verified from field visits. Yellow lines indicate projected faults. Blue box indicates study area in Figure 8. Bonanza Springs is indicated by the yellow star.

The intrusive units are a group of highly fractured Early Miocene igneous rocks, whose compositions range from silicic to mafic. Due to the highly fractured nature of the rock, the transmissivity values of these units likely range from 10 to several 100s of ft^2 per day and the storage capacity likely sits around 5 percent (Kenney & Foreman, 2018).

1.3.1 Recharge Rates of the Fenner Watershed Basin

A previous study has estimated the volume of groundwater naturally stored within the aquifer units of the Fenner Watershed to range from 13 to 23 million acre-feet (Brown, 2013). Under the current version of the Cadiz Project, groundwater is to be extracted at a rate of 50,000 acre-feet per year from the Fenner Valley aquifer system for a 50-year time period. Due to the arid conditions of the Mojave Desert, annual precipitation and recharge rates are very variable, so an accurate estimate of annual recharge to the Fenner watershed is not confidently known. Based on hydrologic modeling, the company estimates that they can extract up to 75,000 acre-feet per year and not greatly impact the long term storage capacity of the aquifer system. To account for "worst-case conditions" due to changing climate, conservative annual recharge calculations of 16,000 and 5,000 acre-feet per year were used in the estimates for longevity of the program (SMWD, 2011). However, as part of a USGS 2000 review of a Draft Cadiz Project Environmental Planning Technical Report, the USGS calculated the annual recharge rate of the Fenner basin to range between 2,000 - 10,000 acre-feet per year (USGS, 2000).

1.3.2 Groundwater Flow and Recharge at Bonanza Springs

Bonanza Springs is recharged from the catchment basin in the Clipper Mountains to the spring's immediate north. Groundwater flow modeling by a third party in preparation for the Environmental Impact Report estimates the long term annual precipitation recharge in the Clipper Mountains to be about 2,400 acre-feet per year (Foreman, 2010). The catchment basin (see Figure 4) is approximately 2,350 acres with an annual recharge rate in

the basin specifically of 190 acre-feet per year. The groundwater level within the basin is at a higher elevation than the surface of Bonanza Springs itself. The Cadiz Report found groundwater levels at 90 to 150 m below the ground surface approximately 1.6 km to the east of Bonanza Springs (Kenney & Foreman, 2018). Based on these depths, a saturated zone may range from as much as 60 to 120 m in thickness within the intrusive unit, upgradient of the spring.

The limits of the catchment basin were identified based on the convergence of two bounding faults zones, one trending northwest and one trending northeast (Figure 4), that Cadiz Inc. believes are acting as barriers to groundwater flow. The report hypothesizes that the spring is recharged when mounding of groundwater occurs to the north of the northeast trending bounding fault zone, and water discharges at the surface from higher elevations along the mountain slope and travels across the surface of the fault zone, falling into a smaller sub-basin that feeds the spring. Any groundwater present in this sub-basin is further separated from the primary alluvial aquifer by the presence of an interbedded sedimentary layer located between the extrusive and intrusive igneous units (Figure 6). This sedimentary unit is estimated to act as an aquiclude separating the spring sub-basin and the Fenner Valley aquifer based on projected groundwater levels from monitoring wells maintained by Cadiz Inc. (Kenney & Foreman, 2018). The report concludes that these hydraulic disconnects separate the source of water at Bonanza Springs from the primary alluvial aquifer and that any extraction of the Fenner Valley aquifer would have no impact on the groundwater level of Bonanza Springs or its northern catchment basin.

1.3.3 Effects of Faulting

The Cadiz Report indicates that abundant small scale faults and fractures were identified throughout the study area through onsite field visits and analysis of satellite imagery. The majority of observed faults were found to have near vertical dips and exhibit slight strike slip displacements ranging from tens of inches to several feet based on field visits

from Kenney and Foreman (2018). It was also noted that many of the faults exhibited calcite and quartz secondary mineralizations that were, in places, several feet thick. The report asserts that the converging northwest trending and northeast trending fault zones are acting as a hydraulic barrier between Bonanza Springs and the northern catchment basin. There exist numerous examples in the literature of faults acting as hydraulic barriers to regional groundwater flow in sediments and lithified rock (Illman et al., 2009; Marler & Ge, 2003; Heynekamp et al., 1999) and the structural controls faulting has on groundwater levels is well known (Figure 7). In addition to acting as barriers, there is also a conduit effect that commonly occur along fault zones. Clay rich soils within well developed fault cores create enhanced zones of permeability along strike of the fault. Parallel, as well as vertical, migration of fluids along the fault plane are often found in fault zones that have simultaneous reduced permeability perpendicular to the fault (Faulkner et al., 2010; Bense, Van den Berg, & Van Balen, 2003; Evans et al., 1997; Caine et al., 1996). Occurring in vertical faulting due to the offset of horizontal layers, strike-slip faulting also exhibits similar conduit-barrier permeability interactions due to cataclasis and particle reorientation. These effects are largely controlled by clay content in the fault zone especially in unconsolidated

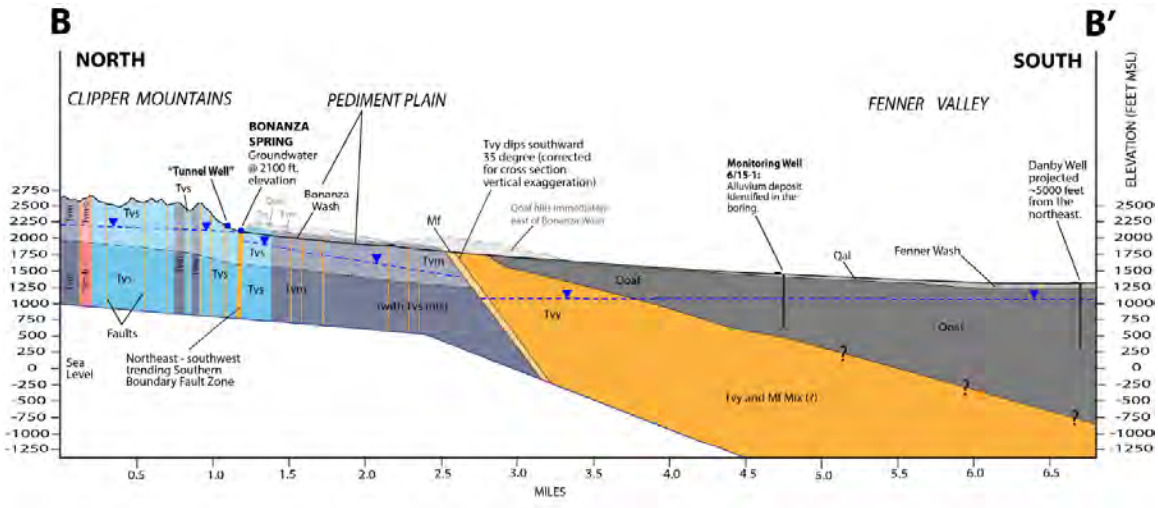

Figure 6: Cross-section of Bonanza Springs running from north to south. Map view of crosssection line visible in Figure 5. Presumed hydraulic barrier to groundwater flow indicated by thick vertical yellow line at approximately 1.2 miles. Modified from Kenney and Foreman (2018).

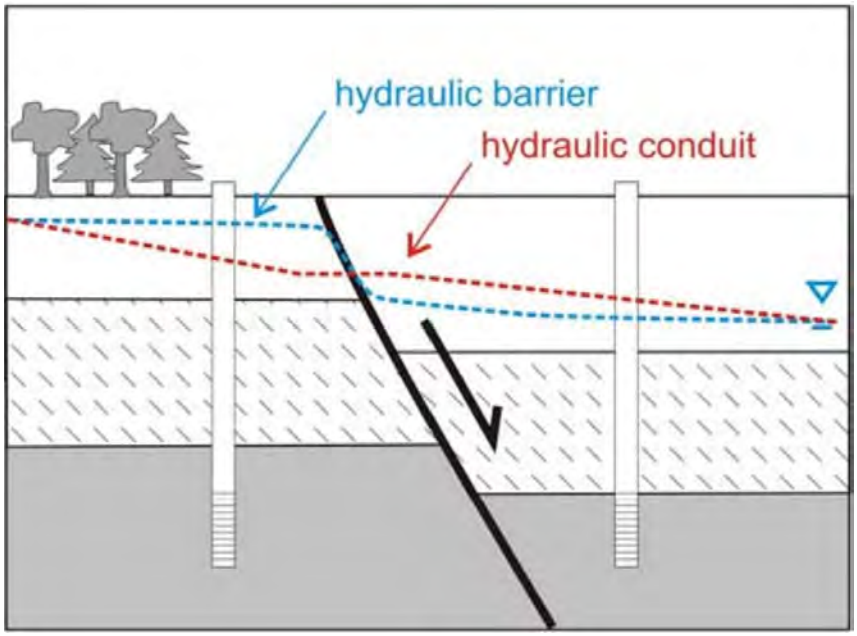

Figure 7: Normal faulting commonly acts as a hydraulic barrier to groundwater flow. Dashed blue line is the groundwater level while the dashed red line represents the hydraulic head. Faulting acts as a groundwater barrier creating non-uniform and non-continuous layers of groundwater in the subsurface. From Bense et al. (2013).

and loosely consolidated formations (Bense et al., 2013; Caine & Minor, 2009).

Motion and strain along a fault can reduce, as well as increase, the permeability within a fault zone (Figure 7). For crystallized or volcanic rock units that have low primary permeability, movement along a fault and the resultant particulate flow can lead to a rearrangement of the pore network and in some cases increase pore size distribution (Bense, Van Balen, & De Vries, 2003). This action can increase secondary permeability along the damage zone of the fault and increase groundwater flow through the fault zone. It is the increase in fracture networks near the faults around Bonanza Springs that allow the normally low permeability of the volcanic units to accommodate groundwater storage and motion.

While faulting can potentially increase groundwater movement across the damage zone, at the fault core it commonly acts a a barrier to groundwater flow. In unconsolidated to loosely consolidated rocks, fault displacements lead to particulate flow that can result in the mixing of unlithified rock of differing grain sizes. This occurs at both the sedimentary bedding and grain size scale, and commonly leads to a reduction of permeability due to the

creation of a more poorly sorted sediment mixture (Rawling & Goodwin, 2006). Generation of fault gouge and breccia in the fault core is extremely common for crystalline rocks and reduces the permeability across the fault plane itself. Hydrogeologic structures of volcanic rocks in fault zones are found to be very similar to those crystalline rock faulting processes and brecciation in the fault core is very common (Evans et al., 1997). Crystalline and volcanic rock laboratory tests have shown that the damage zone becomes a highly permeable zone parallel to the fault plane, while the fault core becomes a low permeability barrier parallel and perpendicular to the fault (Bense & Person, 2006).

Other factors exist that could enhance or decrease fault zone permeability including compaction and cementation of unlitified rock, dissolution and cementation in fracture networks, and alteration of regional stress field in fracture networks (Bense et al., 2013). In particular for water saturated areas, any fluids carrying reactive solutes through fault zones could enhance or decrease permeability through precipitation of minerals into pore spaces (Zhang et al., 2008). While true for carbonate rocks and minerals this precipitation has been observed in crystalline rocks as well; laboratory and empirical observations have shown that quartz is commonly dissolved and re-precipitated in crystalline fault cores reducing their permeability (Bense et al., 2013; Chester & Logan, 1986).

1.4 Geophysical Investigations

In their report Cadiz Inc. states that, "[Bonanza] spring's discharge is localized within a fractured rock system that is hydraulically separated from the alluvial regional groundwater system in Fenner Valley" and that, "perennial spring discharge is controlled by the existence of two bounding faults." (Kenney & Foreman, 2018). They conclude that there is no connection to the existence of Bonanza Springs and the presence of groundwater in the Fenner Valley's alluvial aquifer system and that any reduction in groundwater level will not affect discharge at the spring. However, recent studies of the area shed doubt on the hydraulic separation between Fenner Valley and Bonanza Springs. One study, using

different hydraulic modeling that considers complex mixing of shallow alluvial groundwater sources, has identified Bonanza Springs as being in hydraulic communication with the basin aquifer systems surrounding the Clipper Mountains (Zdon, Davisson, & Love, 2015). A more recent isotope geochemical analysis of water samples taken from Bonanza, and other perennial desert springs, states that the age of water discharging from the local springs suggests a source of groundwater much older than precipitation recharge from mountain regions (Love & Zdon, 2018). Coupled with these new hydraulic modeling and geochemical studies on the potential hydraulic connections between local springs and ground water aquifers, a geophysical study of the Bonanza Springs area will serve to further enhance our understanding of the region. This study aims to use geophysical surveying of the two proposed fault systems that meet at Bonanza Springs to identify any potential fault zone structural controls of groundwater flow and discharge at the spring (Figure 8).

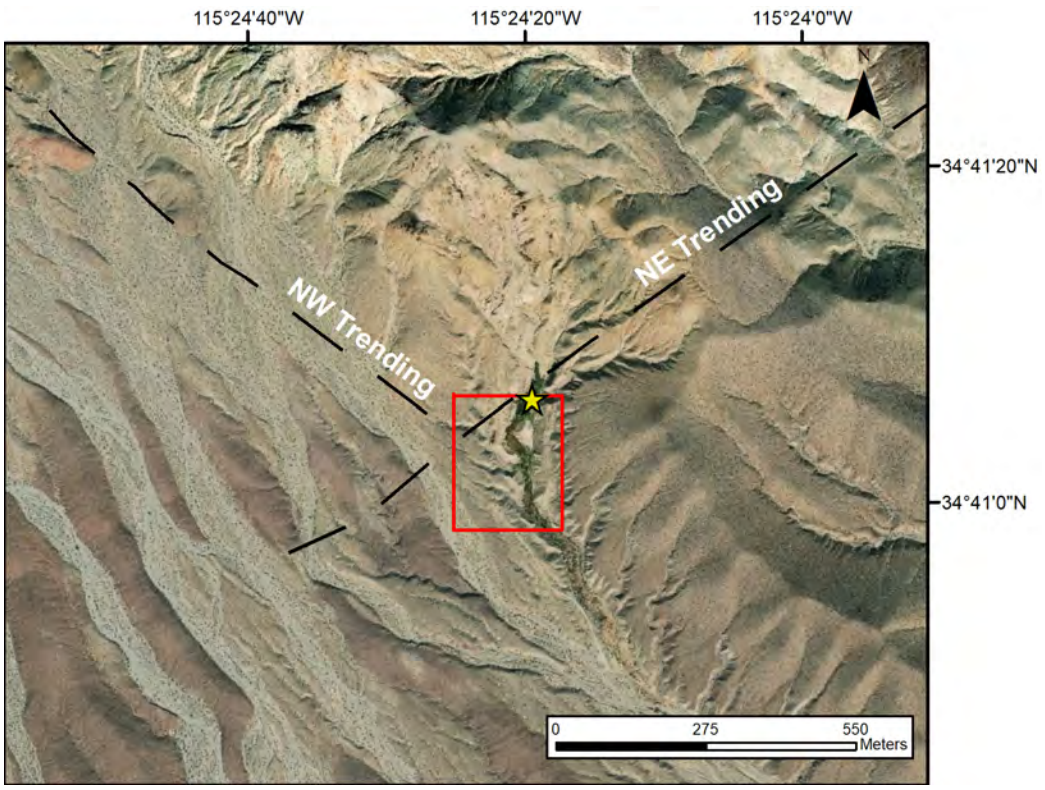

Figure 8: Map of the extent of magnetic and VLF surveys with the two fault zones of interest represented by black dashed lines. Red box indicates area in Figure 43 where the resistivity surveying took place. Yellow star indicates the location of Bonanza Springs.

2 Methods

The Cadiz report has suggested that two fault zones, one trending northeast and the other trending northwest, meet at Bonanza Springs, creating a hydrologic disconnect between the aquifer system feeding the spring and the aquifer in the Fenner Valley (Kenney & Foreman, 2018). It is believed that the spring is fed via groundwater from the Clipper Mountains to the north. Kenney and Foreman hypothesize that the converging fault structures create a hydraulic barrier preventing continuous flow of groundwater down gradient to the south and into the Fenner Valley alluvial aquifer. Instead, groundwater mounds at the hydraulic barrier and discharges at the surface, creating the spring. Therefore, there is no connection between the two aquifer systems and any drawdown in the Fenner Valley will not effect the ultimate source of groundwater feeding the spring. However, there is limited literature available on the geology of the area and no detailed geophysical surveys have been performed. This study aims to enhance our understanding of the subsurface structure in the area and better assess the effects the proposed groundwater extraction would have on Bonanza Springs. This aim was achieved by employing several geophysical surveying techniques including ground based magnetics, VLF (Very Low Frequency), and DC (Direct Current) resistivity surveys.

2.1 Very Low Frequency

The Very Low Frequency (VLF) survey makes use of military communications towers that transmit in the 5-25 kHz radio frequency range. This method was popularized in the early 70s, but has more recently seen a renewed interest due to its portability, the non-invasive nature of the surveying, and speed of data collection. VLF investigations can be used for a wide variety of purposes and there is ample evidence in the literature for its effective use in geologic, hydrogeologic, and even archaeological surveys (McNeill & Labson, 1991; Dailey et al., 2015; Timur, 2012). VLF is ideal for locating shallow subsur-

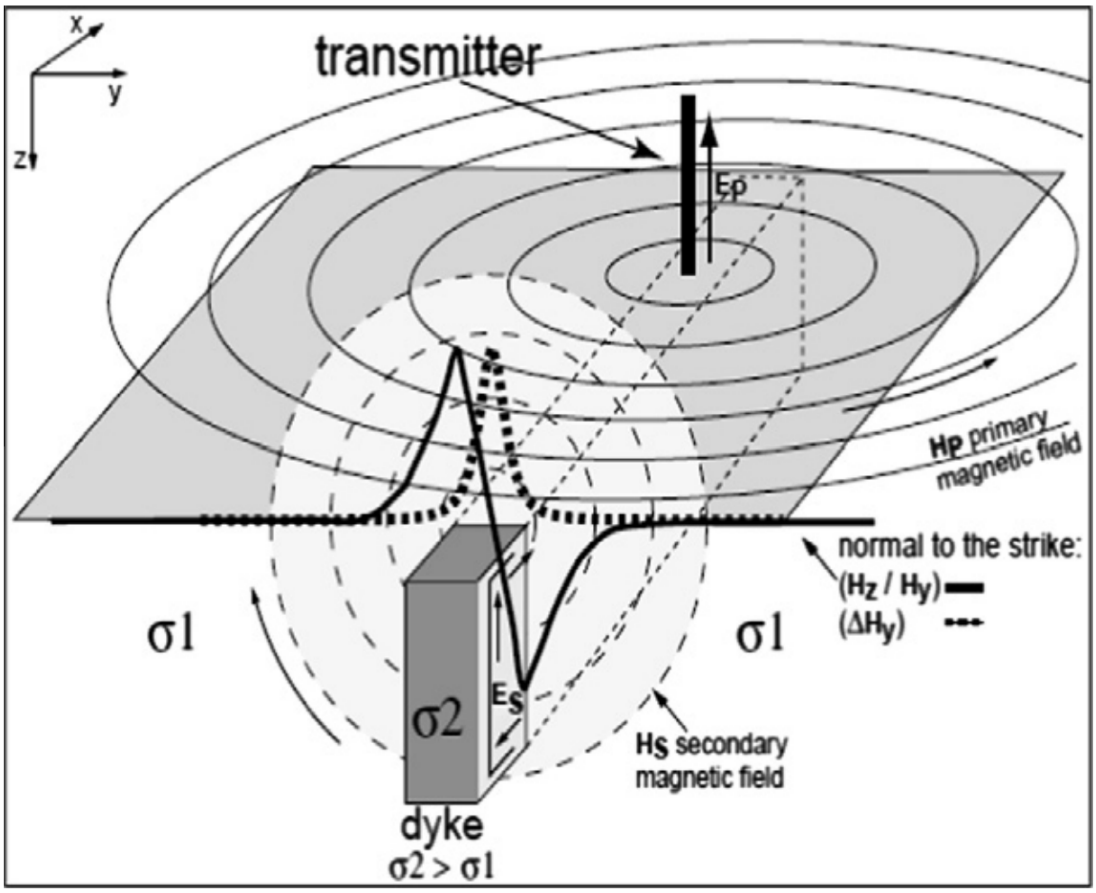

Figure 9: VLF field radiating from a transmitter. The electric (Ep) and magnetic (Hp) components of the primary EM field induce secondary electric (Es) and magnetic (Hs) components through the fields' interactions with a planar conducting body. Figure from Bosch and Müller (2001).

face fault zones due to its sensitivity to conductive structures, such as water saturated fault zones (Phillips & Richards, 1975). If the converging dextral fault zones north of Bonanza Springs are acting as a barrier to groundwater flow, as the Cadiz Report suggests, then VLF surveying would produce a significant conductive response across those fault planes.

The electromagnetic (EM) waves broadcast by VLF stations contain vertical electric and horizontal magnetic field components that are perpendicular to one another. At distances of tens of kilometers from the transmitter it can be assumed that the field components are traveling as waves in a horizontal plane. The magnetic component of the primary field penetrates into the ground and as it passes through a buried planar conductive structure, such as a dike or fault, it induces a secondary electric field within that structure. This

secondary electric field will, in turn, induce a secondary horizontal magnetic field with components oscillating in and out of phase with the primary field (Figure 9). This secondary field interacts with the primary field, polarizing it and causing a tilt, with the tilt angle directly proportional to the strength of the magnetic component of the induced field (Saydam, 1981). The strength of the secondary magnetic field depends on several factors, such as the conductivity of the buried structure, the dimensions and depth of the structure, the orientation of the structure with respect to the propagation direction of the primary field, and the resistivity contrast between the conductor and surrounding medium (McNeill & Labson, 1991).

2.1.1 VLF - Data Collection

A GEM Systems GSM-19T Proton Precision Magnetometer with a VLF sensor attachment and Global Positioning System (GPS) antenna was used to collect the VLF survey data. The system also collects total magnetic intensity and GPS locations automatically when it is run in survey mode (see section 2.2), but VLF readings need to be triggered manually by the surveyor. The VLF sensor unit measures the in-phase and out-of-phase components of the induced secondary field (Figure 13) as a percentage of tilt. The strongest response is obtained when a buried conductor is oriented parallel to the ray path of the primary field as in Figure 9 and the survey crosses perpendicular to the conductor (McNeill & Labson, 1991). Because the locations of the VLF stations are fixed, it can be challenging to find a station that aligns favorably with the fault planes we are attempting to image. To assist with this limitation in profile orientation, the VLF system we used as part of this study is able to obtain readings from three different VLF stations with each measurement. The three source stations used for this study were station NSS located in Annapolis Maryland, station NLK located near Seattle Washington, and station NML located near LaMoure North Dakota, corresponding to frequencies 21.4 kHz, 24.8 kHz, and 25.2 kHz respectively (Table 1). To provide the most optimal results, survey profiles were planned perpendicular

to the trends of the fault zones as proposed by the Cadiz Report, with VLF readings taken every 15 m along the profile path. To ensure good coverage of the study area, multiple profiles were planned along the length of the fault zone around Bonanza Springs, where terrain permitted. This profile spacing is ideal for detecting the average wavelength of tilt anomalies generated for buried conductors and allows for a clearer interpretation of filtered readings (Fraser, 1969).

Based on observations of the collected data, each suspected fault zone had a VLF frequency that produced the strongest signal responses during surveying. As previously discussed, the strength of the induced secondary field components are largely dependent on the conductor orientation relative to the VLF transmitter. Data from the 24.8 kHz frequency station had the strongest signal for the north-west trending fault zone and data from the 25.2 kHz frequency had the strongest signal for the north-east trending zone. These two stations align roughly parallel with the trends of the respective fault zones. Figure 10 shows the unfiltered in-phase components of the three different frequencies from a VLF profile taken across the north-west trending fault zone. As can be seen in the data, the in-phase component at a frequency of 24.8 kHz shows a much higher signal response than the other two frequencies for this orientation. Similarly, Figure 11 shows a VLF profile across the north-east trending fault zone with a greater signal response in the 25.2 kHz frequency range. In some instances, the other frequencies can produce higher signal responses than the frequency that is expected to be optimal for that specific profile orientation and expected fault trend. Figure 12 , for example, shows a VLF profile across the north-west trending fault zone, where we expect a signal at 24.8 kHz to show the highest response. Yet for much of the profile's length, signals at 21.4 and 25.2 kHz are actually reporting equal or stronger re-

Station	Frequency	Location	Azimuth
NSS	21.4 kHz	Annapolis, MD	70.49
NLK	24.8 kHz	Seattle, WA	342.26
NML	25.2 kHz	LaMoure, ND	42.67

Table 1: Azimuth values from Bonanza Springs toward the locations of the station transmitters.

sponses. However, when viewing the signal strength within the raw data for this particular profile (Table 2), it is apparent that the readings taken at 24.8 kHz have consistently higher signal strength than the other two frequencies along this profile path and are more reliable. All VLF profiles performed as a part of this study with the unfiltered in-phase components of all recorded sources are available for viewing in Appendix A.

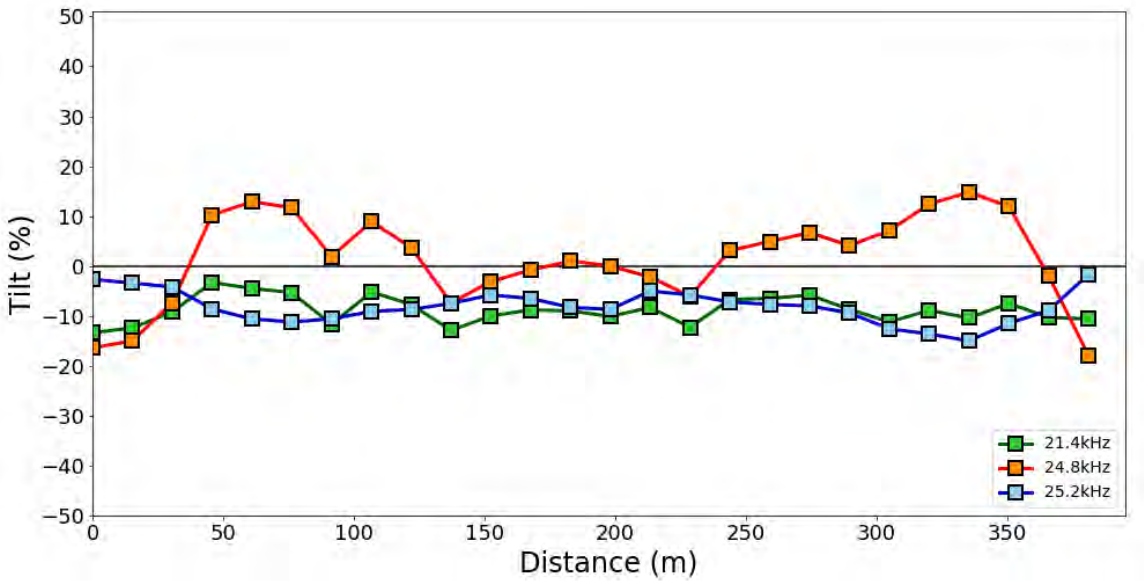

Figure 10: VLF profile D near Bonanza Springs (across the north-west trending fault zone) with the in-phase components of three different frequencies collected. Green, orange, and blue square symbols with lines are collected data points at frequencies of 21.4 kHz, 24.8 kHz, and 25.2 kHz respectively and represent the unfiltered VLF signal response. The signal at 24.8 kHz has the greatest response.

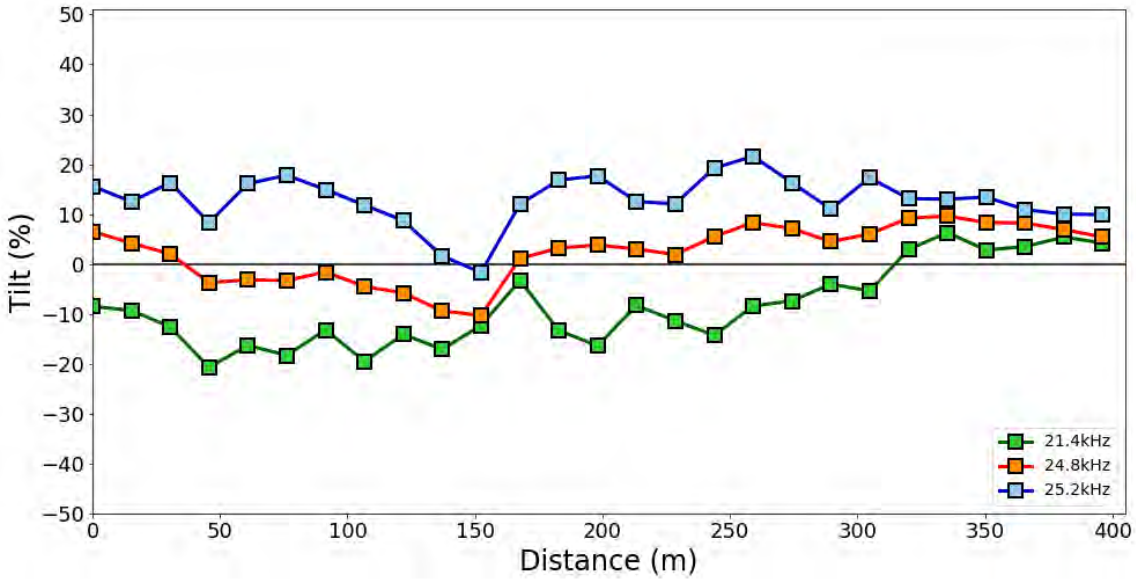

Figure 11: VLF profile I near Bonanza Springs (across the north-east trending fault zone) with the in-phase components of three different frequencies collected. All symbology as in Figure 10. The signal at 25.2 kHz has the greatest response.

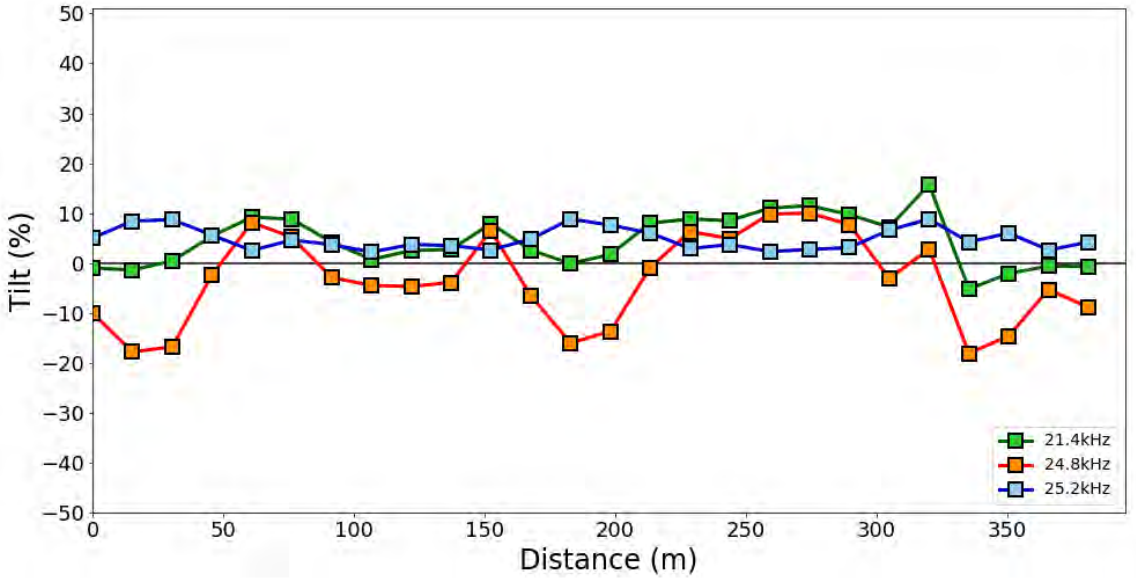

Figure 12: VLF profile C near Bonanza Springs (across the north-west trending fault zone) with the in-phase components of three different frequencies collected. All symbology as in Figure 10. Signals at 21.4 and 25.2 kHz have equal or greater responses than at 24.8 kHz.

distance (m)	21.4 kHz	24.8 kHz	25.2 kHz
0	5.52	10.31	5.87
15	5.96	8.68	5.71
30	5.85	8.02	5.79
45	5.77	7.68	5.75
60	5.85	8.17	5.62
75	6.09	8.38	5.87
90	5.85	8.84	5.72
105	5.65	9.43	5.72
120	5.97	8.55	5.77
135	5.66	8.97	5.64
150	5.72	8.99	5.73
165	5.78	9.4	5.75
180	5.68	8.21	5.6
195	5.78	8.06	5.7

Table 2: Values of signal quality for the first half of the VLF profile shown in Figure 12. Columns labeled with VLF frequencies show the signal quality value (SQ) in values of picoteslas for each of the VLF readings along the profile. Readings taken at 24.8 kHz have consistently higher signal strength. See section 2.1.2 for more information on the signal quality of the VLF measurements.

2.1.2 VLF - Data Processing

The Gemlink software provided by GEM Systems for use with the GSM-19T Magnetometer was used to extract the VLF data. Data files are stored as ASCII files and were sorted to contain the relevant parameters: latitude, longitude, sq (signal quality), time (of reading), kHz (VLF station frequency), ip (in-phase tilt component), op (out-of-phase tilt component), h1 (x-horizontal amplitude), h2 (y-horizontal amplitude), and pT (VLF total field strength). Before Fraser filtering, the data was pre-processed by removing readings with poor signal quality. The sq value field in the data consists of two digits that can range

from 0 - 9 in the format XY. X is equal to the measurement time, while Y is equal to the signal amplitude relative to the time length of the measurement. A value of 0 for X indicates measurement time is too short, while a value of 9 indicates max measurement time was accomplished. A value of 0 for Y means an unacceptable signal reading, while a value of 9 means the reading was obtained under optimal signal conditions. For this study, a measurement with an X or Y signal quality less than 8 was discarded. This criterion was applied for both VLF station readings and magnetic intensity readings (see section 2.2.2).

Once VLF data was collected, downloaded, and pre-processed and plotted (Figure 13), a Fraser filter was applied to assist in data interpretation (Figure 14). The Fraser Filter is one of the most widely used filtering techniques for analysis of VLF data. The filter has the effect of shifting all frequencies by 90 degrees, canceling geologic noise with a wavelength equal to the station spacing, and focusing the maximum amplitude for wavelengths of five times the station spacing (Fraser, 1969). The filter is applied to the tilt angle of the recorded in-phase component of the secondary field and smooths the data, transforming maximum peak values to a location directly over vertical subsurface conductors. When the survey passes over a buried strong conductor, it will appear as a zero crossing in the raw data, but once the data is Fraser filtered, the zero crossings are transformed into peaks enhancing the signal and better locating those signal peaks over the center of the conducting structure (Figure 9). A Python script was written to apply this Fraser filter and plot the data. Fraser lays out the filter operator function in his paper (Fraser, 1969) as:

$$f_{2,3} = (M_3 + M_4) - (M_1 + M_2)$$

where M_1, M_2, M_3, and M_4 are any four consecutive data points and the filtered function is plotted midway between points M_2 and M_3.

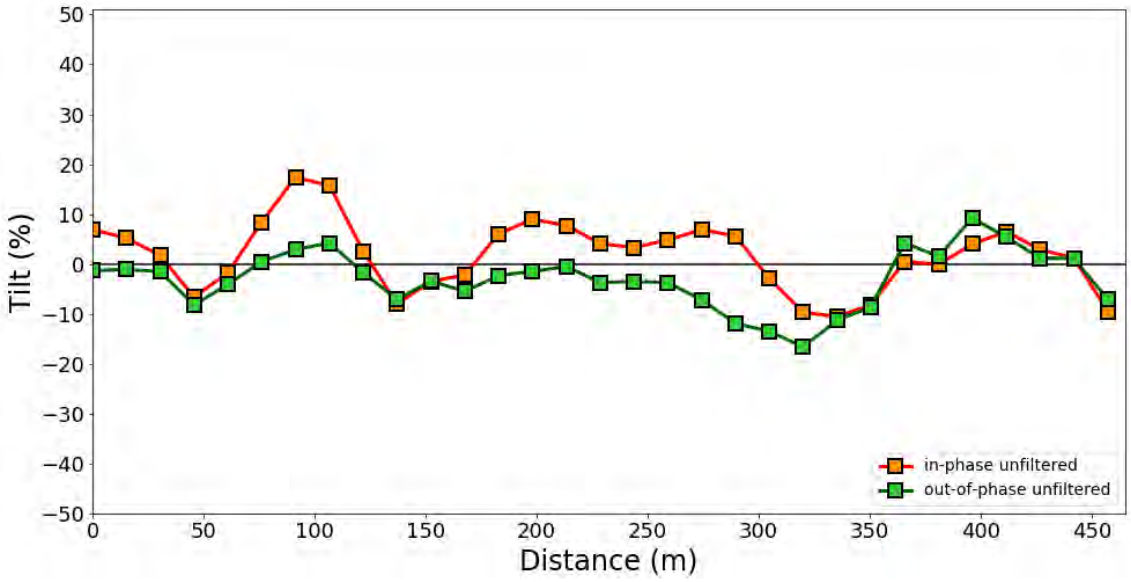

Figure 13: VLF profile near Bonanza Springs at 24 . 8 kHz. The orange squares and connecting line represent the in-phase unfiltered component of the secondary field. The green squares and the connecting line represent the out-of-phase unfiltered component of the secondary field.

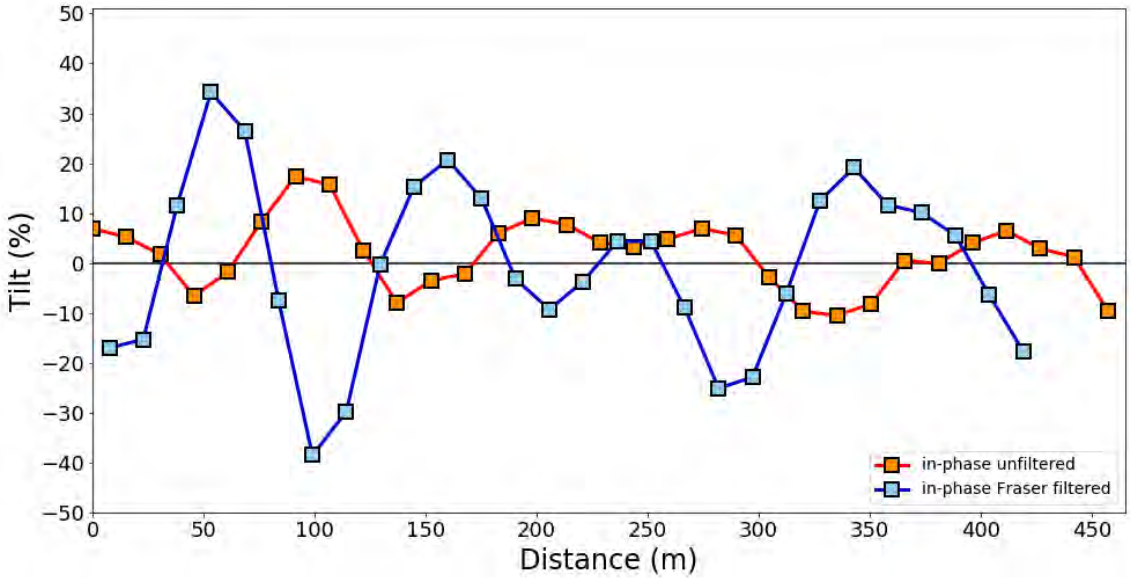

Figure 14: Same VLF data as Figure 13 with a Fraser filter applied. The blue squares and connecting line represent the in-phase Fraser filtered component of the secondary field. See section 2.1.2 for more information on the positioning of the Fraser filtered function values with respect to the unfiltered data points.

2.1.3 Example of Detection of Water Saturated Fault Zones Using VLF Surveying

The Mojave River Groundwater Basin (MRGB) has seen an increase in groundwater extraction to accommodate regional growth and development in the south-western Mojave. The central parts of the basin, in particular, have seen a significant decline in groundwater level that is hypothesized to be the result of dextral faults acting as hydrologic barriers to across-fault groundwater flow (Dailey et al., 2015). Similar to the Fenner Valley aquifer, the MRGB contains interconnected unconsolidated alluvial aquifer systems formed from older (Pleistocene to Pliocene) and younger (Holocene) alluvium. Dailey et al. (2015) performed a near-surface geophysical investigation within the MRGB to determine any potential effects of a major dextral fault, the Helendale Fault, may have on regional groundwater flow. This study involved an integrated approach that made use of LiDAR imaging and magnetic surveying to map fault surface traces and VLF profiling to identify conductive water saturated breccias along fault zones. Similar to the work done for this study, Dailey et al. (2015) were interested in testing the hypothesis that dextral faults and intersecting fault splays are acting as structural controls on groundwater flow. The authors expected to find significant conductive responses in the VLF signal when crossing these fault zones during profiling.

Nineteen VLF profiles were performed across or near the hypothesized surface traces of the Helendale Fault and its adjacent splays, and a four point linear Fraser Filter was applied to the data. Figure 15 shows the results of two VLF profiles across the mapped trace of the Helendale Fault and the corresponding response of the Fraser filtered VLF signal. A single well defined peak in the VLF data is visible along both profiles at the location of the fault, as would be expected for the water saturated conductive structure. Additionally, Dailey et al. noted that a moderate signal response near the beginning of both profiles likely indicated the location of a fault splay of the Helendal fault. Similar results across the rest of the VLF data combined with geochemical analysis from groundwater wells, indicated that the Helendale fault effectively separated aquifer systems in the MRGB by acting as a hydraulic barrier to across-fault lateral groundwater flow (Dailey et al., 2015).

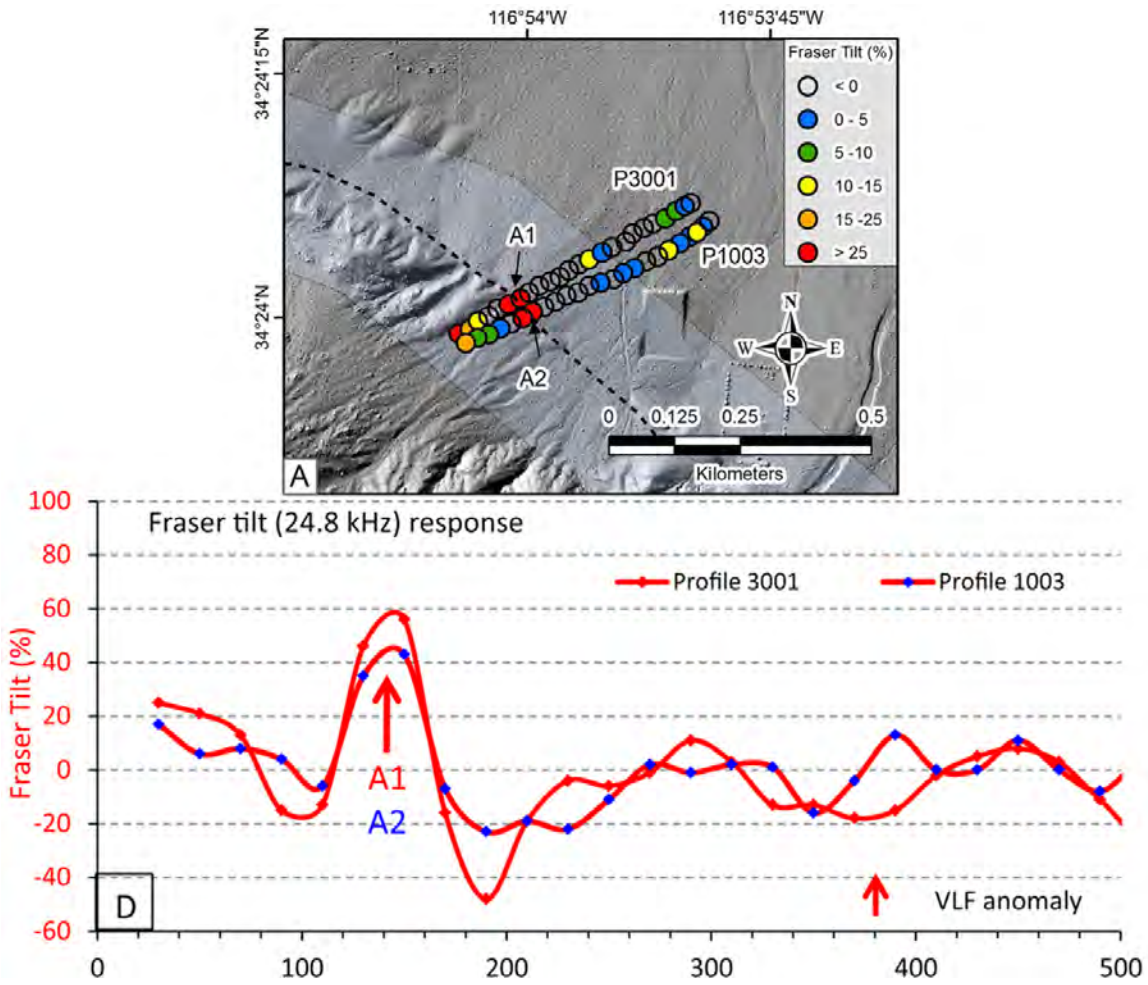

Figure 15: Top: Two VLF profiles across the mapped trace of the Helendale Fault within the Mojave River Groundwater Basin. VLF Fraser tilt scale similar to the scale used for this study. Bottom: Graph of Fraser tilt % versus distance for the two profiles shown in map above. Significant signal response near mapped location of the fault. Figure from Dailey et al. (2015).

2.2 Ground Based Magnetics

Measurements of the intensity of the magnetic field, both ground based and airborne, depend on fluctuations in Earth's magnetic field due to variations in Earth's outer core as well as lateral differences in the magnetic susceptibility of the local geology (Nabighian et al., 2005). When rocks bearing magnetic minerals are placed in an external magnetic field, they will generate their own induced magnetic field; this is described by the equation:

$$I = kH$$

where I is the strength of the induced field, k is the magnetic susceptibility, and H is the strength of the external field. Magnetic susceptibility varies greatly across different rock types (Figure 16), and even among similar rock types. This makes it difficult to determine the local geology from magnetic susceptibility alone, but it is relatively simple to quantify the magnitude of the induced field. The magnetometer used for our magnetic surveying measures the total field intensity of the survey area, a combination of the Earth's magnetic field and the induced secondary field from the local geology. Another component, remnant magnetization, contributes to the total magnetic field intensity and has an influence on magnetic survey interpretation, but in order to simplify magnetic survey analysis, remnant magnetization is often ignored or assumed to be colinear with the induced component (Zietz & Andreasen, 1967).

Magnetic surveying has a long history and wide applications in mineral exploration (Roux, 1967; Oldenburg et al., 1998), the oil and gas industry (Reynolds, Fishman, & Hudson, 1991; Spaid-Reitz & Eick, 1998), and even more recently in buried utility exploration (Rogers, Cassidy, & Dragila, 2005). It is also useful for identifying buried fault and fracture zones, as well as water saturated areas (Loera et al., 2015). Magnetic anomalies allow for the identification of faults, fault zones, and the mapping of volcanic and volcano-sedimentary units (Lopez-Loera, Urrutia-Fucugauchi, & Alva-Valdivia, 2010), similar en-

vironments to the geologic setting of Bonanza Springs. In particular, when looking for buried faults in igneous units, we expect to see high amplitude anomalous magnetic lows or magnetic minima due to the combination of fault gauge and the oxidation of magnetite to hematite (Henkel & Guzman, 1977). The oxidation of magnetic minerals, such as magnetite to hematite, results in minerals with much lower magnetic susceptibilities (Figure 16) and a lower intensity induced magnetic field. If the local geology of an area is largely igneous rock with magnetic minerals present, and a fault zone results in oxidation of those magnetic minerals, the result would be an area of largely magnetic highs with a sharp zone of magnetic lows aligned with the fault.

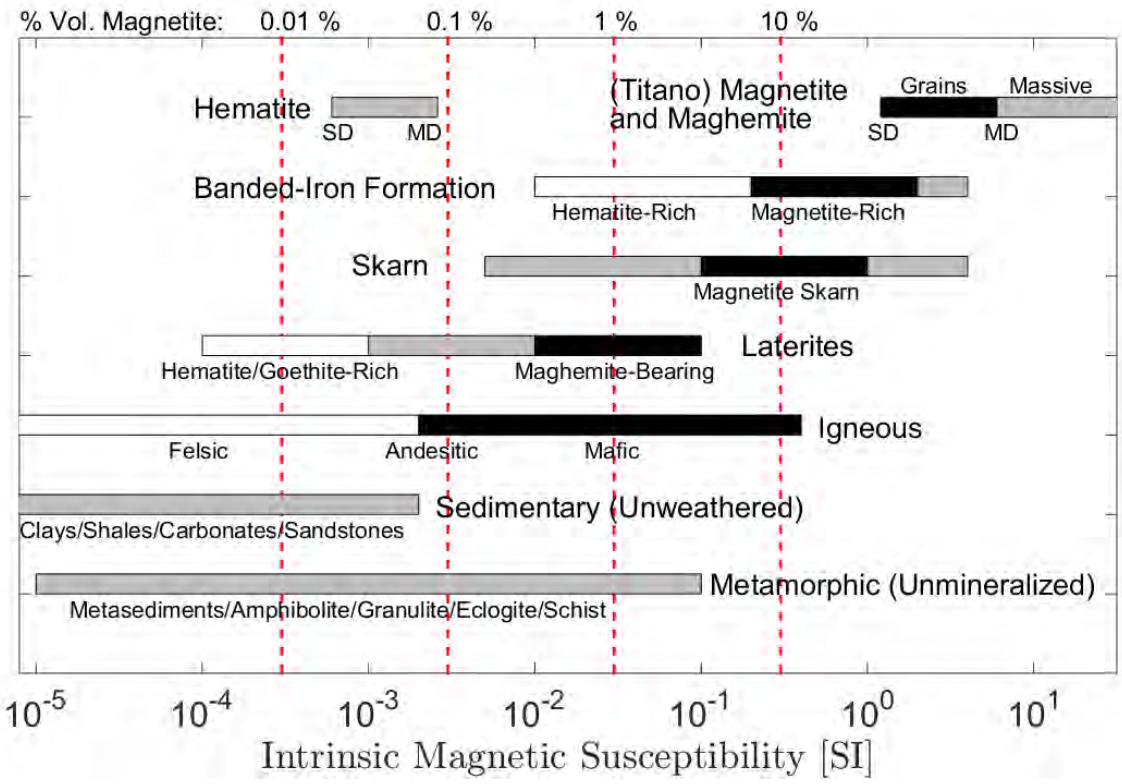

Figure 16: Variations in magnetic susceptibility of various rock types. Adapted from Clark and Emerson (1991).

2.2.1 Magnetics - Data Collection

A GEM Systems GSM-19T Proton Precession Magnetometer was used to collect ground based magnetic data within the survey area. It uses the same equipment setup as the VLF

method, but does not require use of the additional VLF sensor attachment. The magnetometer sensor consists of a cylindrical container containing a solenoid and filled with a proton rich kerosene-like fluid. The proton precession magnetometer works based on the spin of suspended protons as they move through a magnetic field as described by the Larmor precession equation (Hrvoic, 1996).

$$\overrightarrow{\omega} = \gamma \overrightarrow{B}$$

where $\overrightarrow{\omega}$ is the angular frequency of precession, γ is the gyromagnetic constant and $\overrightarrow{B}$ is the magnitude of an applied magnetic field. A large current is applied via the solenoid and it creates an induced magnetic field perpendicular to the Earth's magnetic field with which the protons then align themselves. When the current is then removed, the protons precess towards their original alignment with the ambient magnetic field and spin at an angular frequency that is directly proportional to the induced magnetic field. As they spin, they generate a magnetic field that is picked up by an electronic sensor within the container, that is then recorded by the computer unit as a field strength.

The system used in this study allows for a walking magnetics survey mode to be performed. Once in this mode, the magnetometer automatically collects a total field intensity reading and GPS location of said reading every two seconds. Surveys were organized in a grid pattern with multiple profiles parallel to each other and spaced 20-25 m apart where terrain allowed; this spacing allows for good resolution to observe the fault zones of interest in the magnetic data. The survey grids crossed the proposed fault zones perpendicularly across their lengths in the area around Bonanza Springs. During surveying, magnetic cleanliness was practiced by the surveyor to ensure capture of high quality data. Surveys were run in two-man teams, with the surveyor wearing the magnetometer and a guide leading the surveyor along the predetermined survey path several paces ahead. The guide also made observation of any metal detritus in the survey path, removing it from the surveyors path

and making a note of its position.

2.2.2 Magnetics - Data Processing

The GEM Link software is used to extract the magnetic data in a ASCII file format with data headers that include: latitude, longitude, elevation, nT (total field intensity), sq (signal quality), and time (of reading). Once the data has been extracted, it is pre-processed before any gridding and/or filtering. Data points are checked for signal quality with similar criteria as used for VLF surveying. Additionally, the total field intensity values of the surveys are graphed and any anomalously high or low values that are only a few samples wide are removed. These values typically also correlate with readings of poor signal quality and/or noted areas where the survey passed over small pieces of scrap metal. Before further processing, data is corrected for diurnal variations. Day to day minor variations in the Earth's magnetic field have a noticeable effect on survey data (Nabighian et al., 2005) even when surveying the same path only days later (Figure 17). To correct for this a "base traverse" was designated early on in the study; any additional surveys performed at a later time also crossed that base traverse, so they could be corrected. Figures 17 and 18 show the process of correcting for variations in the magnetic field. The offset in field intensity was identified and a correction factor was applied to line up the intensity values, the correction factor was then applied to the rest of the survey data for that day to correct for that diurnal variation. Any minor remaining variations between the base and survey profiles are likely due to variations in the walked profile path.

Because we apply a correction factor determined from a base survey that is located several hundred meters away from subsequent surveys, there will be slight variations in the Earth's magnetic field across those surveys. The magnetic field does vary with changing horizontal and vertical positions along the surface of the Earth. However, these variations were not considered for this study as the extent of the area of magnetic data collection was relatively short at approximately 1.5 km^2; any variations due to changing position in this

area would be minuscule. For example, we can consider an equation for the rate at which the vertical component of the magnetic field varies with horizontal position:

$$\frac{1}{r}\frac{dH_r}{d\theta} = -\frac{2M\sin\theta}{r^4} = -2\frac{H_E}{r}$$

and another for the rate at which the vertical component varies with vertical position:

$$\frac{dH_r}{dr} = -\frac{6M\cos\theta}{r^4} = -3\frac{Z_E}{r}$$

where H_E and Z_E are the horizontal and vertical components of the Earth's magnetic field and r is the radius of the Earth. At the latitude of Bonanza Springs ($35.69°$) where the National Oceanic and Atmospheric Administration's (NOAA) International Geomagnetic Reference Field (IGRF) database gives a horizontal magnetic component of 23,767.8 nT, this would roughly equal a variation of 7.5 nT/km with changing horizontal position. This is a relatively small variation when compared to variations expected due to changes in geologic signal in the 200 - 500 nT range. Similarly, at the same latitude and with a vertical component of 41,181.7 nT there would be rate of 0.02 nT/m of vertical change.

The Oasis Montaj software was used to further process and filter the magnetic survey data. A minimum-curvature gridding technique was applied that fits a surface to the dataset to interpolate between the actual readings taken during the survey, both between profile lines and between data points. This generates a model of total magnetic field intensity for the survey area by estimating values based on an inverse distance average within a specified cell size that is usually half the profile spacing (Swain, 1976). The shape of the magnetic anomalies that appear in the gridded data are largely dependent not just on the shape of the magnetic bodies in the subsurface, but on the inclination and declination of the Earth's magnetic field. To correct for this, a reduction to pole (RTP) filter was applied to the gridded surface. The RTP filter transforms the observed magnetic anomaly into the anomaly that would have been measured if the magnetization and ambient field were

both vertical (Baranov & Naudy, 1964), better locating the gridded anomalies above the causative bodies. This filter requires knowledge of the magnetic inclination and declination at the survey site, information that was obtained from the NOAA's IGRF database.

Significant effort was made to avoid any metal objects on the surface of the study area. However, the spring is adjacent to an old mine, and there remain various abandoned pieces of mining equipment strewn about the area. To reduce any influence of stray metal pieces on the data, an Upward Continuation (UC) was applied to the dataset. An upward continuation transforms the data as if it were recorded at a higher elevation. This has the effect of attenuating and minimizing any dipoles or short wavelength features that may result from shallowly buried metal interfering with the magnetic survey (Nabighian et al., 2005). Finally, a vertical first order tilt derivative was applied to the RTP corrected data to better emphasis shallower and weaker magnetic structures. The dependence of the tilt angle on the magnetization means that both strong and weak magnetic anomalies are treated with the same weight (Blakely, Connard, & Curto, 2016) useful for observing weaker magnetic anomalies associated with fault and fracture zones expected in this area.

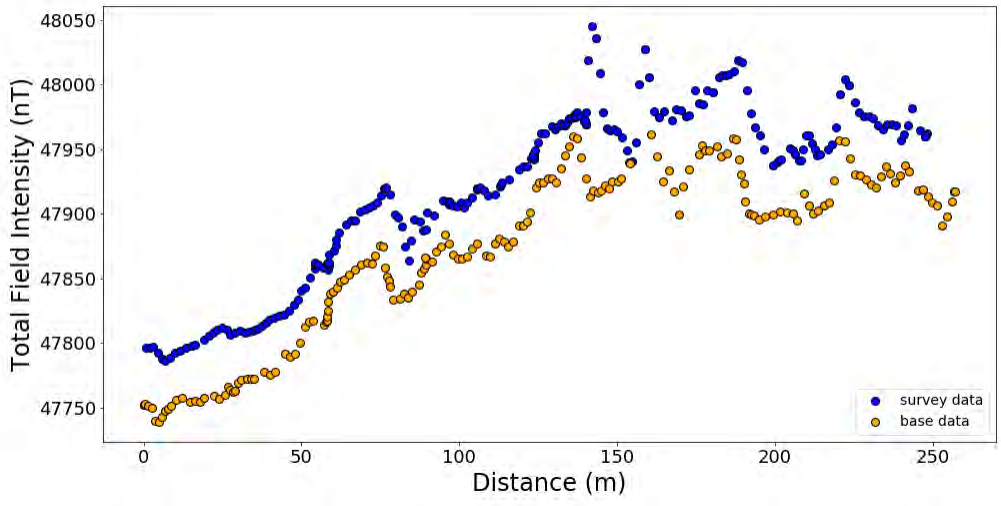

Figure 17: Graph of ground magnetic data of the base profile and data along the same path taken at a different day. Note the offset similar pattern of total field intensity.

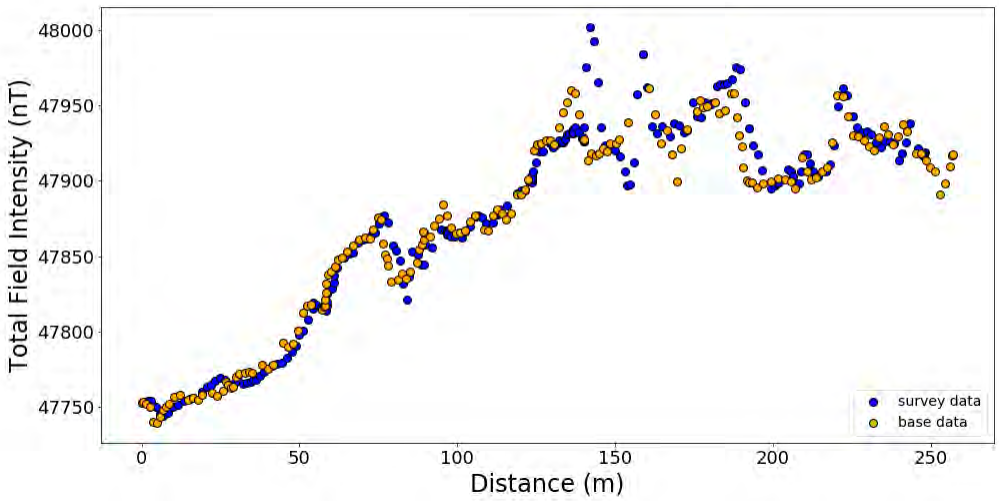

Figure 18: Base and survey data with a correction factor of 43 nT applied to the survey data to correct for the diurnal variations in the magnetic field. Remaining variations between profiles due to minor variations in profile paths.

2.2.3 Examples of Magnetic Expressions of Faulting and Water Saturated Zones

As previously discussed, it is hypothesized that Bonanza Springs is separated from its groundwater source by converging fault zones acting as hydraulic barriers. Ground-based magnetic and aeromagnetic surveys have been used to identify fault bounded saturated zones in arid and semi-arid zones. In the valley of San Luis Potosí (SLP) in central Mexico, fault bounded aquifer systems were identified using magnetic surveying for groundwater extraction to accommodate the growing population of the region (Loera et al., 2015). Large scale extensional faulting has created a series of normal faults that covers the Mesa Central Region of central Mexico. The extensional environment led to the formation of horst and graben structures that form the SLP valley and are responsible for normal faults that act as confining structures for local aquifer systems. The study made use of aeromagnetic data taken over the region to first identify areas with significant low magnetic anomalies and identifiable magnetic lineaments that may be associated with faulting structures (Figure 19). Once these low magnetic features were identified in the aeromagnetic dataset, ground-based magnetic surveys were run to target these areas and gather higher resolution

data. Figure 20 shows the results of profile a-b taken across two areas of magnetic lows to the north of the study area. The ground-based survey data agrees with the results of the aeromagnetic data,and indicates that there are two areas of significant magnetic lows along the profile path. The bottom topography profile of Figure 20 includes an illustration of potential saturated zones along the area's low magnetic anomalies. Further surveying identified additional sites with similar responses as in Figure 20. Exploratory drilling was performed at one of these sites and pump testing lead to yields of 70 liters-per-second indicating surveying successfully identified a heavily saturated groundwater zone (Loera et al., 2015).

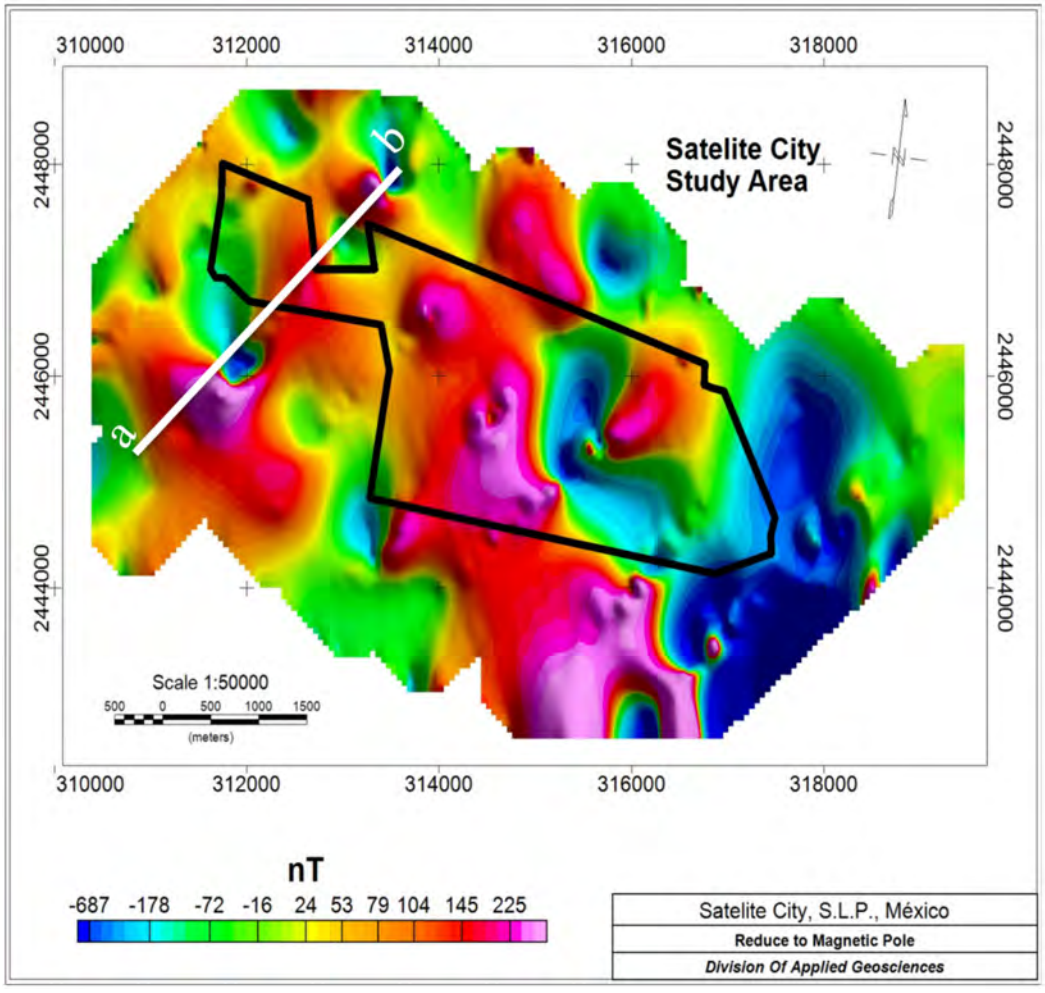

Figure 19: Aeromagnetic data of the study area within the SLP valley with an RTP filter applied. To identify zones of potential saturation, small areas of magnetic lows were located in the data and targeted with further ground based magnetic surveying (profile a-b). From Loera et al. (2015).

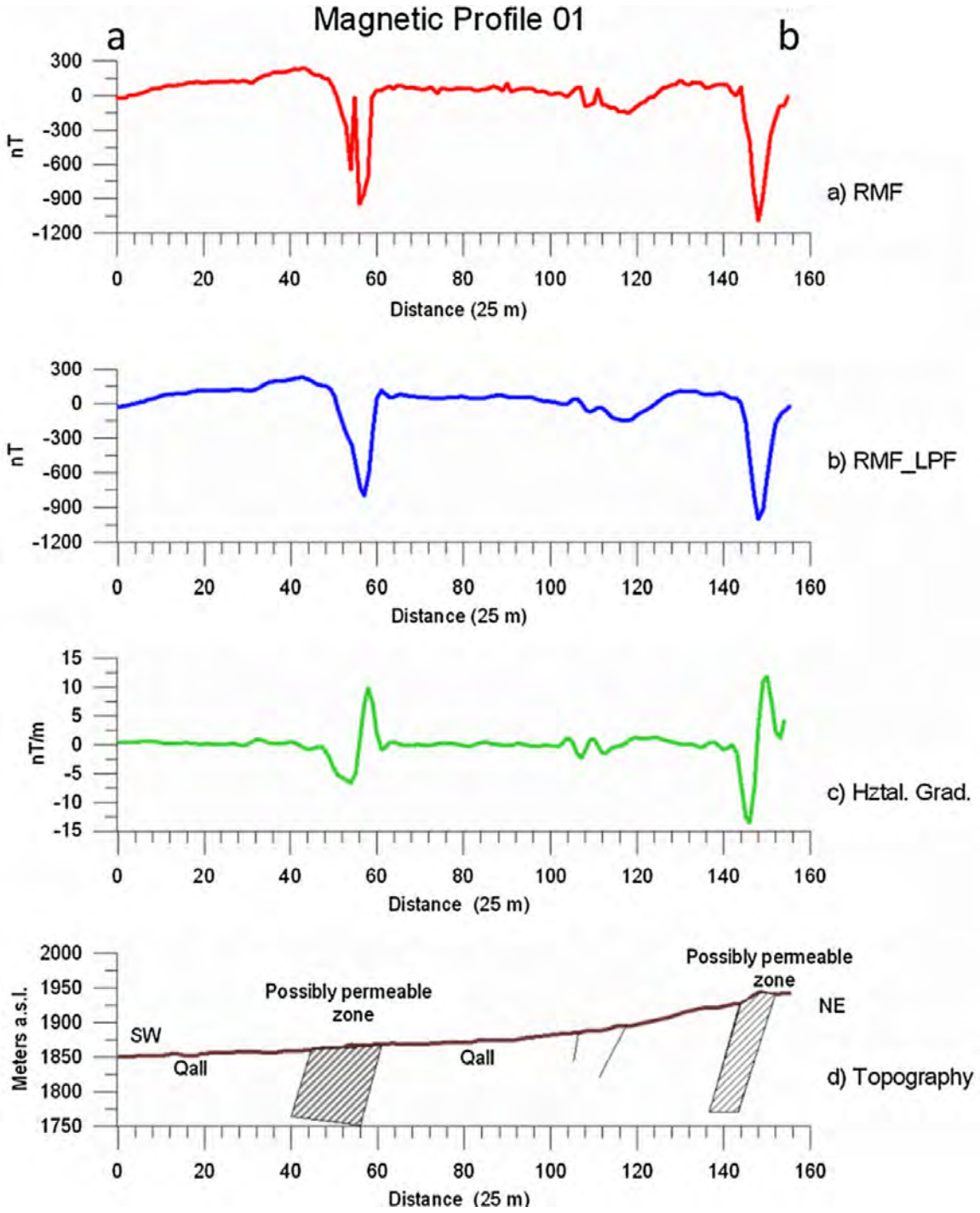

Figure 20: Magnetic data of profile a-b from Figure 19. Magnetic lows in the ground-based surveying match location of magnetic lows in the aeromag surveying. Red profile represents Residual Magnetic Field (RMF), the remaining value of field intensity once the contribution of the Earth's magnetic field is removed from the collected total field intensity. Blue profile is RMF values with a Low Pass Filter (LPF) applied. Green profile is the horizontal gradient of the magnetic field. Bottom profile is the topography of the profile path with inferred location of permeable zones from the magnetic lows in the above profiles. From Loera et al. (2015).

2.3 Direct Current Resistivity

Electrical resistivity tomography makes use of low frequency electrical current that is injected into the ground by two current carrying electrodes. The resulting potential difference is measured between two potential electrodes (Figure 21). Different rocks will have differing resistance to the applied current flow. Resistivity (ρ) differs from resistance (R) in that resistance depends on the volume and dimensions of a material, while resistivity does not: it is solely a physical property of a material. Resistivity varies over many orders of magnitude (Figure 22) even among similar rock types and depends largely on mineral content, porosity, pore size distribution, fluid saturation, and clay content (Ball et al., 2010).

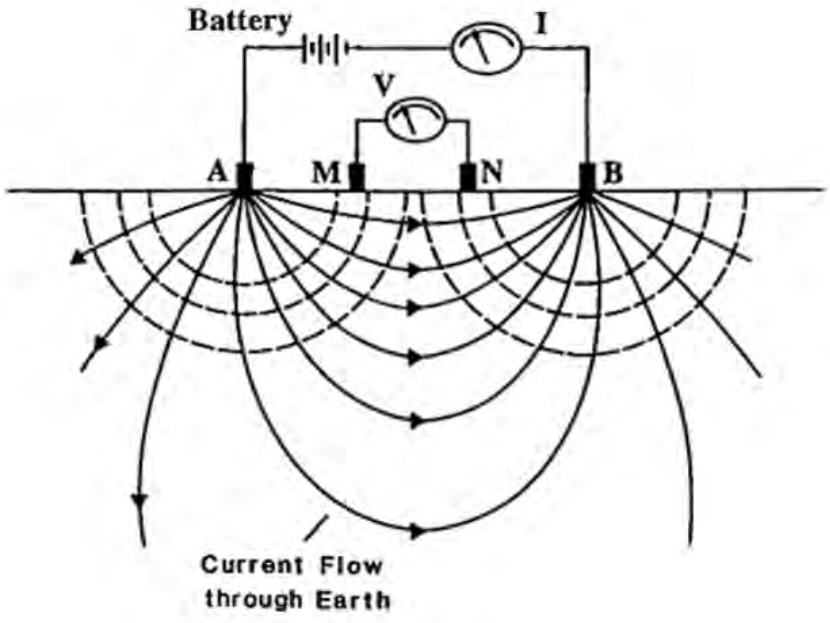

Figure 21: Simplified electrical resistivity survey in a homogeneous half-space. Voltage flows from current electrode A to current electrode B. Uncharged current electrodes M and N measure the electric potential. Solid lines represent current path and dashed lines represent equipotential lines. Modified from Benson et al. (1983).

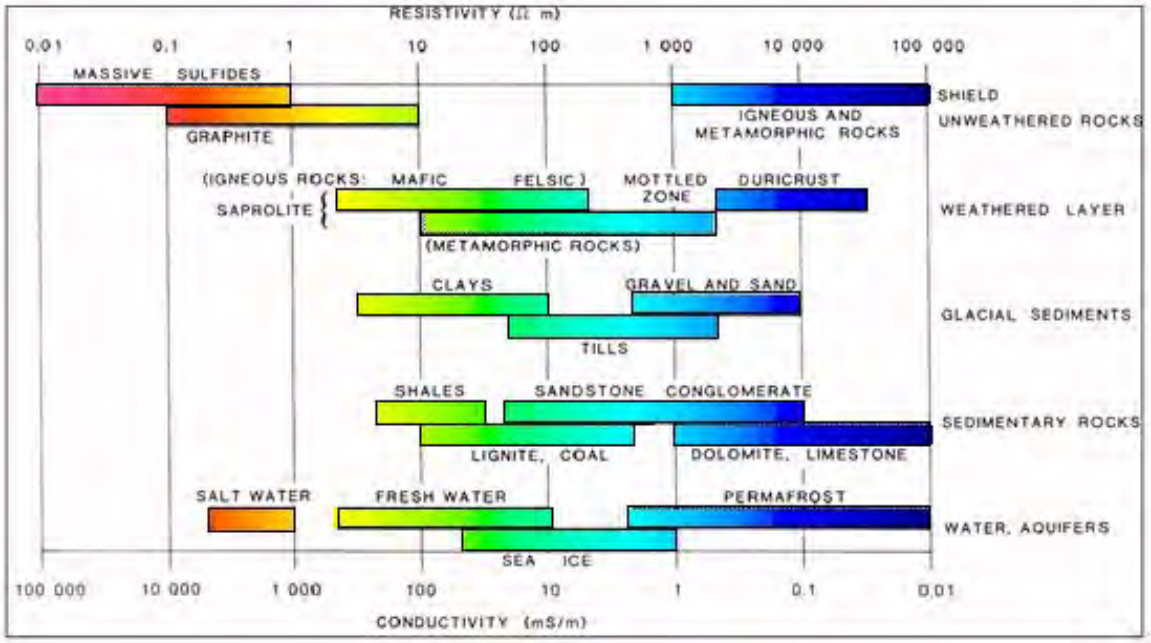

Figure 22: Chart of typical resistivity ranges for rocks. Modified from Palacky (1988).

Because groundwater is very conductive and fluid saturation plays such a large role in the resistivity of materials, DC resistivity surveys are very useful for detecting or characterizing aquifer systems or saturated zones (Parsekian et al., 2015). Modern resistivity surveys make use of multiple electrodes per survey line to automate and speed up data collection. Several electrodes are laid out and connected via a switching cable and a computer unit automatically switches the current and potential electrodes on the cable line. By increasing the spacing between active electrodes along this array, the injected current travels farther into the ground, allowing for more of the subsurface to be imaged (Figure 23). By moving the two sets of electrodes along the array, larger and more complex geologic structures can be effectively imaged. There are several different electrode configurations of multi-electrode arrays in use currently, the most common of which include: Wenner, Schlumberger, dipole-dipole, and pole-to-pole (Loke, 2000). Each array is more or less sensitive to various structures in the subsurface and each carries different survey advantages depending on the goal of the survey. It is important to note that, because the subsurface is not homogeneous and resistivity often varies with depth as wel as laterally, the data

measured and recorded during surveying are not the ”true” resistivity values, instead they are apparent resitivity (ρ_a) values. According to the equation:

$$\rho = \frac{2\pi\Delta V}{i}$$

resistivity depends on observed measurements of voltage (V) and current. Current has a preference towards areas of least resistance and will flow differently as it passes from one layer of resistivity into another layer, altering the total measured voltage. Variations in current flow will result in variations of measured apparent resistivity.

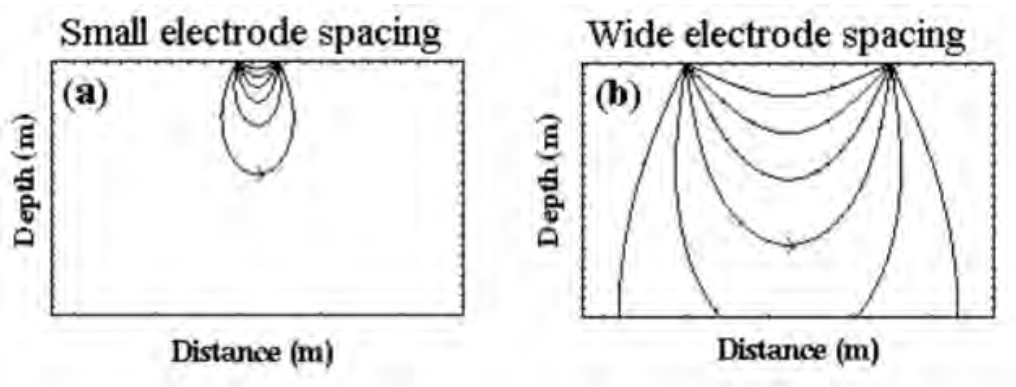

Figure 23: Simplified diagram demonstrating that with increased electrode spacing, current will travel deeper into the subsurface. From Carpenter et al. (2012).

2.3.1 Resistivity - Data Collection

This study seeks to determine if there are any vertical offsets in the groundwater table that may indicate mounding on the northern side of the fault zones. Such discontinuities in water table height may suggest the presence of a fault acting as a hydrologic barrier as was hypothesized in the Cadiz Report (Kenney & Foreman, 2018). To accomplish this, a SYSCAL Pro 24-Switch Unit was used with a Wenner array experimental set-up to investigate depth to the groundwater table in the area around Bonanza Springs. The Wenner array was chosen because it is sensitive to vertical changes in the subsurface resistivity, especially towards the center of the array (Loke, 2000). This provides good vertical resolu-

tion when attempting to image resistivity changes of subsurface structures with horizontal layering, such as the water table. A maximum electrode spacing of 10 m was used for a maximum survey length of 230 m; the Wenner array allows for a median investigation depth of 0.173 times the total survey length, or roughly 40 m of investigative depth at the center of the array for a length of 230 m. The resistivity surveys were designed to capture the expected change in groundwater level across the fault zones. To this end the survey lines were oriented so that the center of the array was located directly above the mapped location of the proposed fault zones in the Cadiz Report (Kenney & Foreman, 2018). In addition to performing surveys at 10 m electrode spacing, two more surveys were run at 5 m and then again at 2.5 m electrode spacing, using the same center point for all surveys. Reducing the electrode spacing reduces the maximum depth of investigation, but allows for higher resolution of the observed shallow subsurface structure.

The same set-up parameters were used for all surveys performed, only the electrode spacing was varied. A stack min of 2 and stack max of 4 was used with a q-value of 3. These parameters control the range of measurements made, with each reading taken for a combination of quadrupoles (two dipole pairs of current and potential electrodes) along the array. Stack min controls the minimum number of readings per quadrupole and stack max controls the maximum allowed. The q-value is the percentage of acceptable standard deviation between readings; if this value is reached before the amount of stack max readings is achieved, the SYSCAL Pro unit moves to the next quadrupole combination along the line. If the q-value is never reached, the unit performs the maximum number of readings indicated by the stack max. Readings that do not achieve a desirable q value are of lower quality and often filtered out during pre-processing. An n factor of 7 was also used for all resistivity surveys. The n factor is the ratio of the distance between the first dipole pair and second dipole pair of electrodes. This roughly correlates to the ”level” or depth of current penetration into the subsurface; with increasing levels meaning deeper surveying depth. Usually an n value of 7 is the maximum value used for surveying as anything greater leads

to inaccurate measurements due to very low potential values (Loke, 2000).

2.3.2 Resistivity - Data Processing

Once data was collected, it was extracted from the SYSCAL Pro unit via the IRIS Prosys II software for resistivity data management. The data was stored as a binary ASCII data file and before modeling was attempted, the data files were pre-processed using automatic filtering in Prosys II. The automatic filter works by identifying anomalously high and low resistivity values and eliminating them. Readings with high standard deviations ($>$20 %) are also identified and removed. Once this filtering is completed, the data can be exported in a file format that can be used with the inversion modeling software.

Geotomo's Res2DInv software was used to generate inversion models for the collected and filtered resistivity data. The pre-procesed files are first read into the software and the measured apparent resistivity values are used to construct a pseudo-section of those measurements. Then the measured apparent resistivity values are used to construct a preliminary depth model of the potential subsurface based on those measurements. Next, the software calculates predicted values of apparent resistivity for the preliminary subsurface depth model. These predicted values are used to generate a second pseudo-section of calculated apparent resistivity. The software then compares the calculated apparent resistivity values to the measured apparent resistivity values and based on the differences in the data, adjusts the depth model of the subsurface. A new synthetic apparent resistivity pseudo-section is then generated from this adjusted model and again compared to the actual measured values. This process repeats several times until depth model is generated whose calculated apparent resistivity values fits the measured values with a Root Mean Square (RMS) error of less than 5 percent. Once this is achieved, the software then generates a final figure with the psueudo-section of raw data values (Figure 24A), the final two-dimensional model of resistivity as a function of depth along the horizontal distance of the profile (Figure 24C), and a pseudo-section of predicted measurements based on this model (Figure 24B).

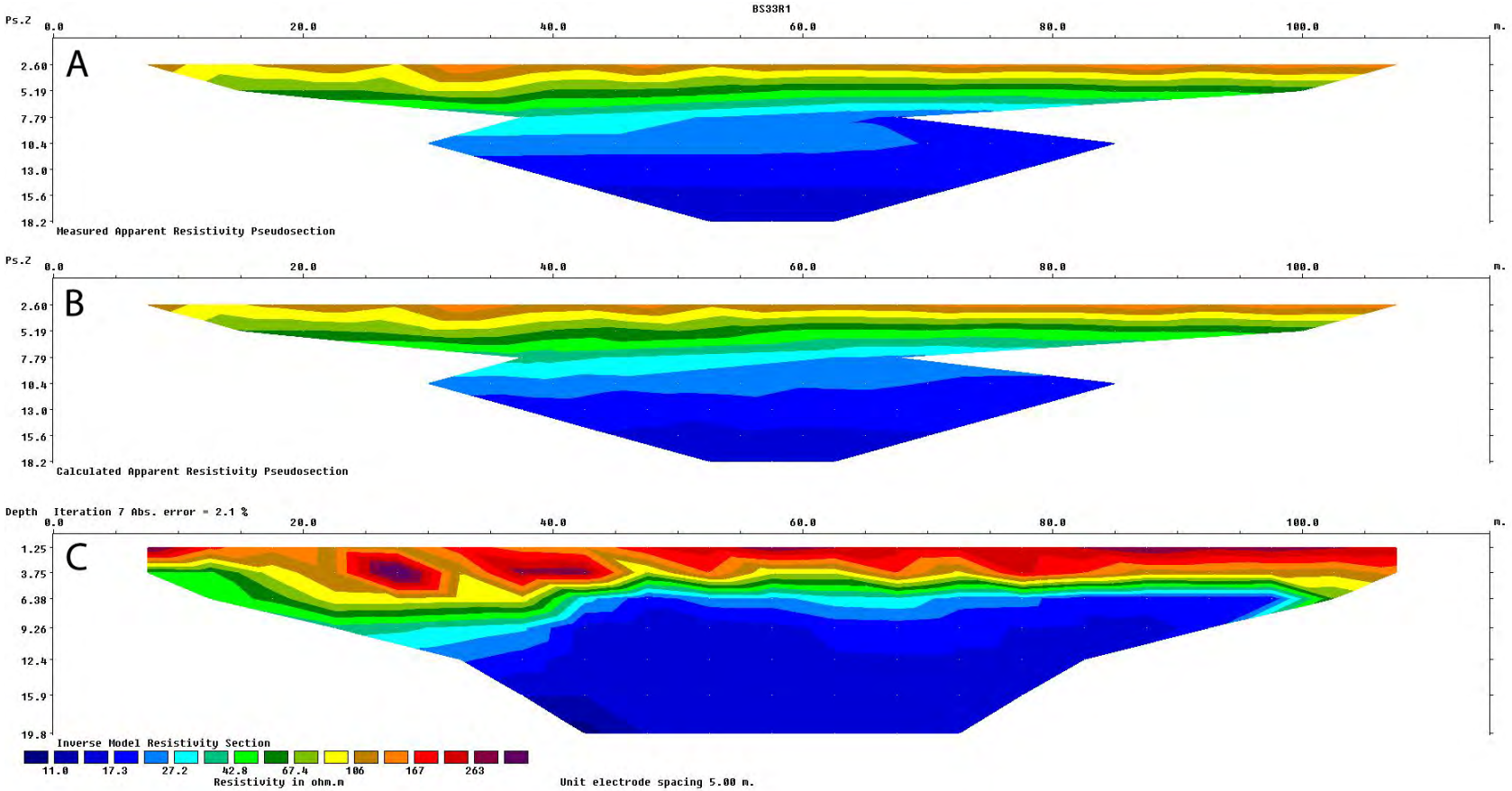

Figure 24: Res2DInv inversion model results for a resistivity profile conducted near Bonanza Springs. A) measurements are plotted as a pseudo-section B) Pseudo-section of calculated apparent resistivity values predicted based on the generated subsurface depth model. C) Inverse resistivity depth model. Missing ”slices” in the top two pseudo-sections due to the filtering out of low quality data points.

Figure 24 is the end result of the Res2DInv inversion process. Throughout this process multiple depth models are generate and the predicted apparent resistivity values of those models are compared to the actual measured apparent resistivity values. It is important to note that final depth model is only one potential model of the subsurface. An accurate depth model will have a low RMS error and a calculated psuedo-section that match very closely with the measured pseudo-section as Figure 24 demonstrates.

2.3.3 Example of Resistivity Imaging of Faults in Saturated Zones

Numerous previous studies have been carried out with DC resistivity surveying and imaging of shallow buried fault systems. An unknown splay of the Geleen fault within the Roer Valley of northeastern Belgium was successfully imaged based on electrical resistivity profiling (Vanneste, Verbeeck, & Petermans, 2008). Though active, the Galeen fault has a fairly low slip rate that results in faint geomorphic expressions of the fault at the surface of younger alluvial deposits. The valley within the study area consists of mostly alluvial sand and gravel deposits with the oldest surficial units dating from 15 kya, deposits not too dissimilar from the area around Bonanza Springs. Prior to any geophysical surveying, field reconnaissance was done to identify suspected areas of the Galeen fault splay from observed weak surface expressions of the fault. Survey sites were chosen based on this initial field work and electrical resistivity tomography surveying was done to determine if these inferred positions from early field analysis were accurate.

Figure 25 shows three inversion models for three profiles at different spacings taken across a suspected fault splay of the Geleen fault. (Vanneste et al., 2008) notes that low resistivity values in the profiles likely indicate areas of highly saturated sands and gravels and a depth to the water table can be seen at an elevation of approximately 36 m. A vertical offset of the water table can be observed in profile 25a, where purple arrows indicate the presumed position of the fault based on offsets in the resistivity values. Profile 25b shows a sharp, near vertical, contrast in resistivity values, while profile 25c has mapped a possible

location of the fault zone based on contrasts in resistivity values. Offsets and rapid sharp changes in resistivity values indicate some subsurface structure, the fault splay, acting as a minor barrier to the flow of groundwater. This splay of the Geleen fault was successfully identified in the resistivity data as a sharp near-vertical structure with lateral contrast in resistivity values and its position was later verified by trenching (Vanneste et al., 2008). Successful imaging of the fault splay indicates the resistivity method is useful for precise determination of the orientation and position of saturated shallow buried fault systems.

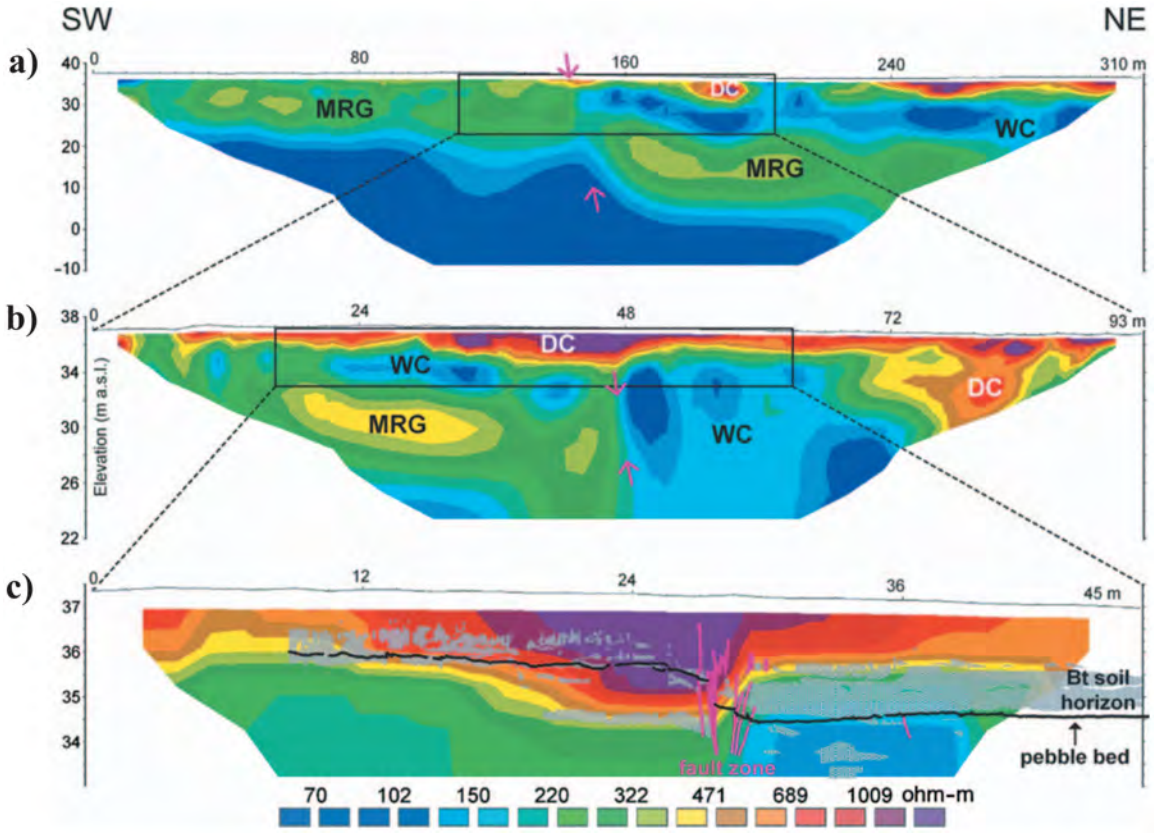

Figure 25: Inversion depth models for three resistivity profiles at three different electrode spacings taken across a suspected splay of the Geleen fault in northeastern Belgium. Purple arrows denote location of fault in the subsurface identified by offsets and incongruities in resistivity values. Labels correspond to units of the Maas River Gravels (MRG), Wet Cover Sands (WC), and Dry Covered Sands (DC). From Vanneste et al. (2008).

3 Results & Discussions

A series of geophysical surveys were performed around the area of Bonanza Springs to investigate the existence of two potential fault zones believed to converge near the spring. Magnetic and VLF profiling provided complementary datasets to help identify any significant structures within the subsurface. Resistivity surveys in the area presented a glimpse into the subsurface to help achieve a better understanding of how groundwater may be affected by the potential presence of faults in the area.

3.1 Ground Based Magnetics

Magnetic surveying gives us a view into the magnetic anomalies present in the Bonanza Springs area that are generated by local subsurface geologic features or structures. Figure 26 shows the extent of ground-based magnetic surveying performed around the area of Bonanza Springs, with red lines indicating the profile paths walked as part of this study. In order to capture suitable coverage of the suspected fault zones, profiles were oriented so that they crossed the previously mapped locations of the faults perpendicularly and covered large portions of the fault zones. A constant grid spacing of 30 m between adjacent parallel profile lines was generally adhered to, but the challenging terrain sometimes made this difficult to achieve, with the area to the immediate north of the springs being particularly difficult to traverse.

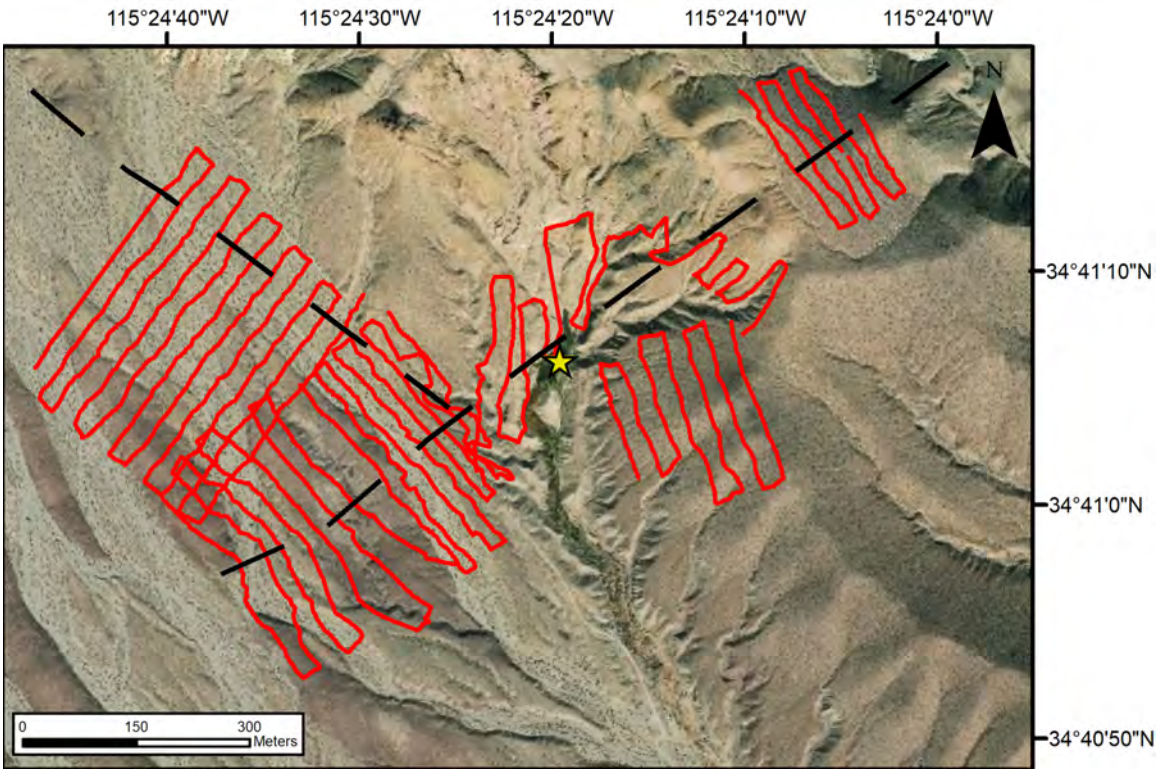

Figure 26: Map of Bonanza Springs with the profile paths walked for the ground-based magnetic survey indicated by red lines. Black dashed lines are the two suspected fault zones from Kenney and Foreman (2018), while the yellow star indicates Bonanza Springs.

Magnetic data was gridded via Oasis Montaj with a 10 m grid cell size to generate a base map of total field intensity values around the spring and across the two converging fault zones (Figure 27). The gridding function interpolates between the collected measurement points to generate a total intensity map. To help ensure the software is generating a reliable map of magnetic intensity values, the measured field intensity values were plotted on top of the gridded map using ArcMap. As can be seen in Figure 28, when a similar graduated color ramp is applied to the measurements, they match the colors of the gridded map product. No artifacts or spurious signals are apparent, increasing confidence in the results of the interpolation.

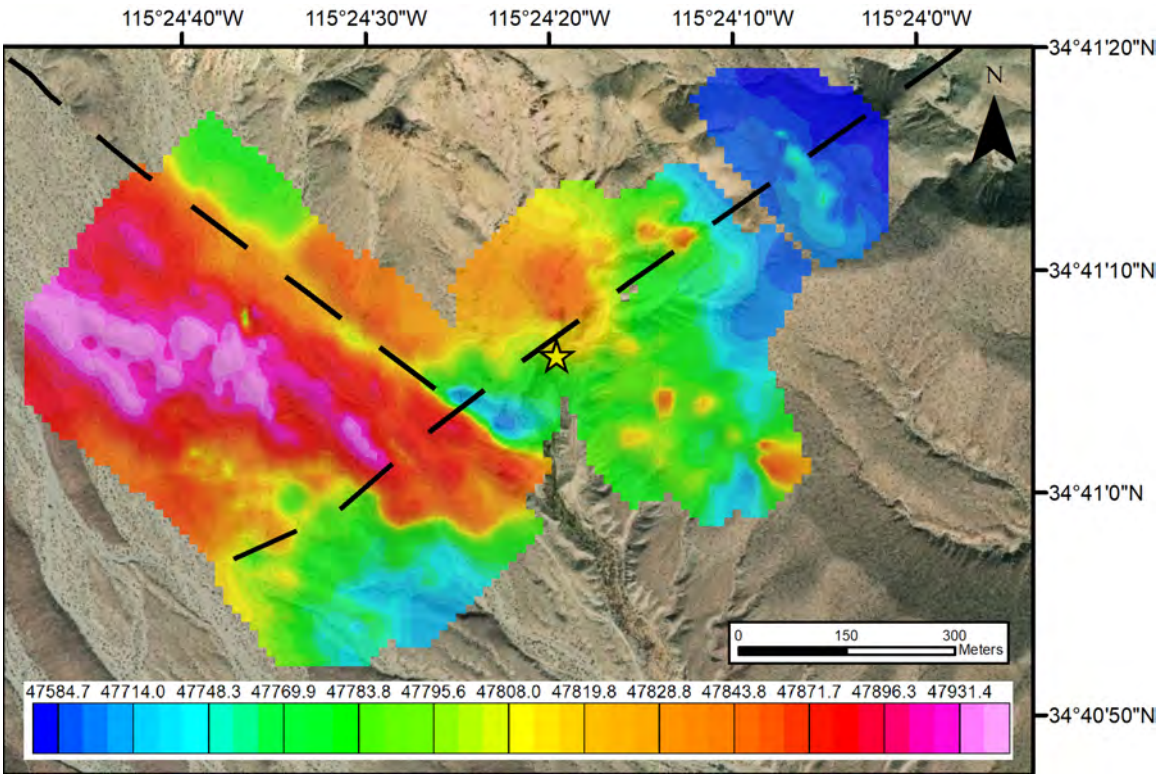

Figure 27: Total field magnetic intensity map of the Bonanza Springs area, gridded with Oasis Montaj. Color scale of total field intensity values in nanoteslas (nT) at bottom of map. Location of study area visible in Figures 5 and 8.

Figure 28: Interpolated total field intensity map of Bonanza Springs with collected data points overlain. Map shows a portion of the measurements across the north-west trending fault zone to demonstrate collected data values match contoured gridded values. Same color scale as Figure 27.

The magnetic anomalies observed around Bonanza Springs (Figure 27) provide insight into the geologic structures present in the subsurface. Specifically, we observe a high spatial gradient, between high intensity values to the south west and lower values to the northeast, in the magnetic data that aligns well linearly with the proposed location of the north-west trending fault zone. This feature cuts through an area of high total field intensity about 200 m west of the spring and is oriented in a similar strike to the mapped location of the fault zone. The feature continues further north-west along the trace of the proposed fault for approximately 260 m, until it transitions from a magnetic high to a relatively magnetic low that continues to loosely follow the fault trace. A similar linear feature is not observed along the north-east trending fault zone. An area to the south-west of the spring has a continuous magnetic high that crosses this proposed fault zone. There is no linear anomaly in the data with a similar strike and orientation as this proposed fault zone and the observed magnetic high does not appear to be offset by any faulting. North-east of the spring along the fault zone there are no identifiable linear features, only areas of low field intensity with a gradual transition from ranges of 47,760 nT to 47,580 nT farther north-east along the proposed fault. Additionally, there are magnetic anomalies with particularly high field intensity values of 47,900 - 47,950 nT to the west of the mapped north-west trending fault. There appears to be a grouping of thin linear features adjacent to this proposed fault zone that match its strike. Based on their high magnetic intensity values and thin, linear appearance, these features could potentially be part of a dike swarm. Tabular dike bodies were observed and reported by Kenney during field visits for the Bonanza Springs Impact Assessment Report (Kenney & Foreman, 2018).

An RTP filter was applied to better locate the magnetic anomalies in the data directly over the causative bodies that generate them (see section 2.2 for details on this method). This approach helps to simplify interpretation. Using a position of $34°41'8.1''$ N, $115°24'19.6''$ W and an elevation of 639 m (the coordinates of Bonanza Springs) the IGRF database calculated an inclination of $60.05°$ and a declination of +$11.39°$. These

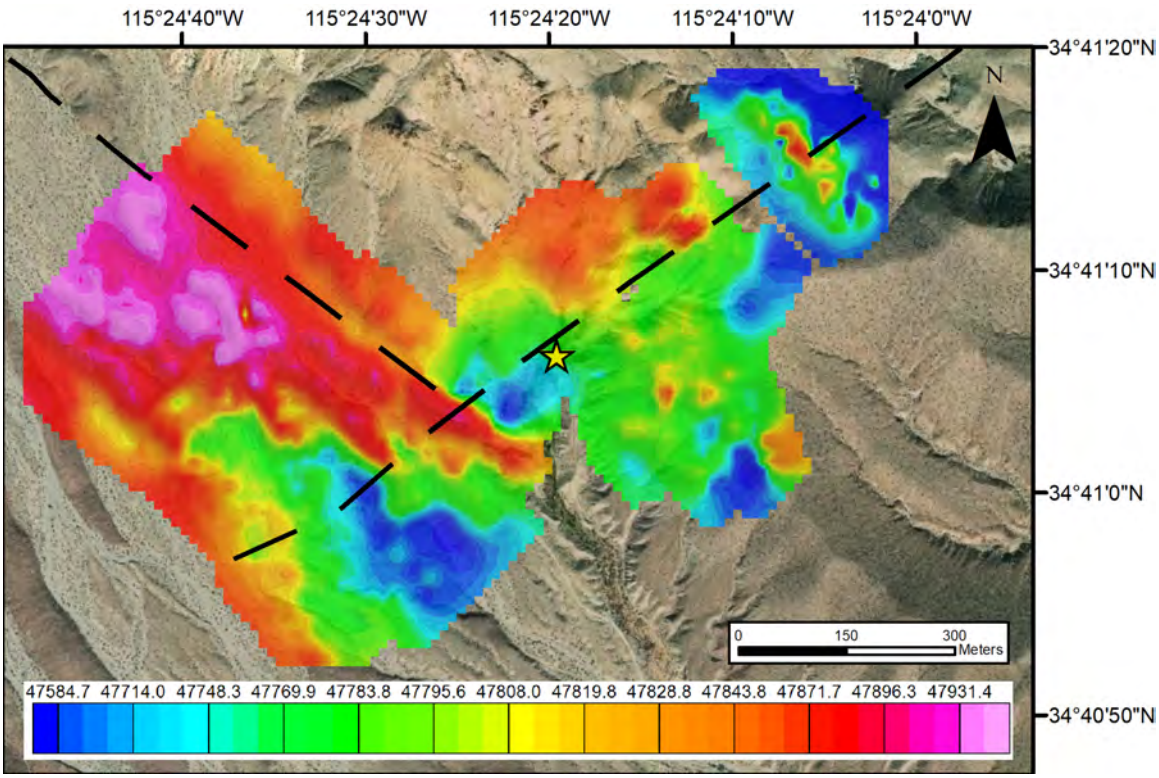

Figure 29: Total field magnetic intensity map of the Bonanza Springs area with an RTP filter applied. Same scale and symbology as Figure 27.

values were used to apply the RTP filter to the gridded data and the result can be seen in Figure 29. From comparisons between Figures 27 and 29 we can observe a slight shift in position of the magnetic anomalies. The linear anomalous feature along the north-west trending fault zone is still visible, although the change in total field intensity across the fault is slightly less significant. There are additional shifts in intensity values in the north-east areas of the grid and the south-west in the range of 200 - 280 nT.

As previously discussed, an abandoned mine is located just to the north of the spring itself, with derelict mining equipment and old scraps of metal consistently found throughout the study area. Great efforts were made to remove or avoid these highly conductive and magnetic sources, but judging from some small areas of magnetic highs to the spring's east, these attempts may not have been completely successful. To reduce and minimize the effect of these high amplitude shallow signals, an upward continuation was applied to the RTP filtered data. Figure 30 shows the data that has been upwardly continued by 10 m. This

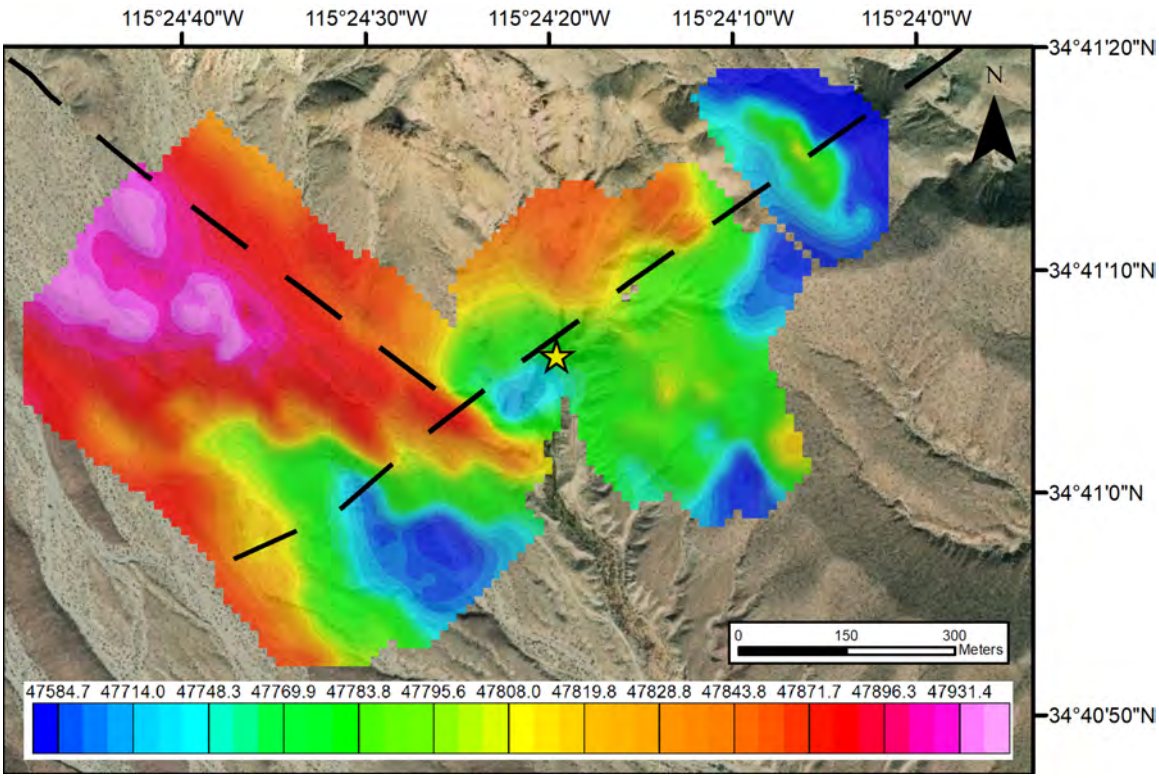

Figure 30: Total field magnetic intensity map of the Bonanza Springs area, with an RTP filter and upward continuation of 10 m applied. Same scale and symbology as Figure 27.

height was chosen because it eliminates or reduces much of the shallow signal noise, while preserving the geologic signal. There is a reduction in total field intensity of about 100 nT in the north-east area that saw an increase after the RTP filter was applied. The magnetic highs to the east of the spring are also mostly gone in the upwardly continued data. After the continuation was applied, the data shows smoothed magnetic high anomalies with no large changes in the shapes or positioning, indicating that the signals from local geologic bodies are largely intact and the filtering has not introduced significant bias in the data.

The final filter applied to the data was a vertical tilt derivative (Figure 31). As discussed in section 2.2.2, this procedure is useful because it enhances high frequency shallow geologic features and allows for weakly magnetic bodies to be weighted the same as higher magnetic values when gridded. From Figure 31 this filtering technique helps distinguish between magnetic highs and lows, we can see that the linear feature along the north-west trending fault zone becomes much more clear after the derivative is applied. The grouping

of linear magnetic highs to the west of the north-west trending fault is also much more apparent in the data. The final filtered data again indicates a zone of continues magnetic high that crosses the proposed north-east trending fault zone. If these magnetic highs are the result of dikes or differing rock units, then these structures appear to cross this proposed fault zone along its entire length unimpeded by any other structure and are not offset by any faulting. Conversely, there is a considerable gradient present across the north-west trending proposed fault zone, where a significant magnetic low is centered below the mapped location of this fault. The low is most prominent directly to the west of the spring, where the difference from the highest to lowest total field intensity is approximately 400 nT. This linear feature is present further along the fault's strike towards the north-west, where the trend appears to move off the mapped zone towards the north and broadens. Finally, there is another broad zone of magnetic lows south of the linear magnetic highs that continues across the proposed north-east trending fault zone. Due to the width of the low anomaly, this area may represent highly saturated damage zones associated with the north-west trending fault zone in the magnetic data. Alternatively, it could be an additional fault or grouping of fault splays, as it follows a similar strike to the north-west trending fault.

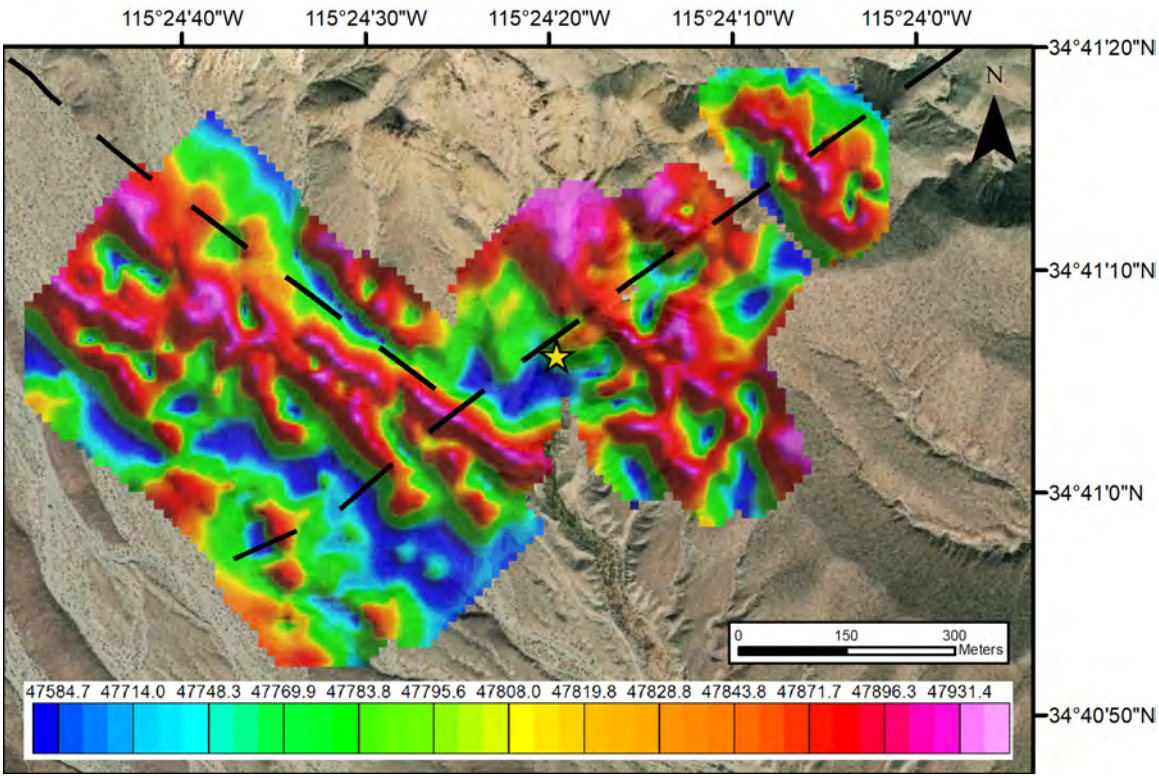

Figure 31: Total field magnetic intensity map of the Bonanza Springs area, with an RTP filter, upward continuation of 10 m, and a vertical tilt derivative applied. Same scale and symbology as Figure 27.

3.2 VLF

VLF profiling provides an additional dataset that complements the magnetic surveys that were also performed. Sixteen VLF profiles of varying lengths were completed perpendicular to both proposed fault zones thought to be acting as hydraulic barriers: five across the north-west trending and eleven across the north-east trending fault zone. Of the eleven profiles across the north-east trending zone, nine were performed south-west of the spring and two were carried out to its north-east (Figure 32). To improve image clarity, not all profiles were included in Figure 32 but are available in Appendix A. Measurements for three different VLF source stations were recorded along each profile, and since the strength in signal response of a conductor is determined by the orientation and geometry between source and conductor, each fault zone had a specific station that was expected to produce stronger anomalies than the others, based on its trend. The relative amplitudes of any anomalies are expected to be most pronounced for a conductor aligned parallel to the ray path of the VLF field and for a profile path running perpendicular to the conducting body. As shown in section 2.1.1, for the north-west trending fault zone, the NLK station near Seattle, Washington operating at 24.8 kHz showed the strongest anomalies, while station NML near LaMoure North Dakota operating at 25.2 kHz produced the optimal signal for the north-east trending fault. Therefore, these specific sources will be used in most of the summary maps in this section.

Figure 33 shows the Fraser filtered in-phase tilt components of the VLF survey profiles combined with the magnetic data from Figure 31. Analysis of the VLF data in this section will make use of the magnetic surveying to assist in the identification of buried subsurface conductors. The VLF profiles will be interpreted in detail and compared to results from the magnetic surveys. Fraser filtered values were placed on a scale similar to what was used by Dailey et al. (2015) in their characterization of structural controls on groundwater in the Mojave desert. The area they analyzed is similar to the study area around Bonanza Springs and also makes use of VLF data to identify fault structural controls on groundwater

flow. In their paper, Dailey et al. consider any VLF tilt response >25% significant and a similar criteria was used for this study. We considered signal response >25% significant, while responses between 10% and 20% where considered moderate. This criteria may be considered conservative, as Fraser (1969) notes in his paper that in optimal conditions 5% tilt may be significant and Dailey (2015) reports thresholds of 10% or 15% confirming conductive fault zones. Several of the profiles to the south-west of the spring along the north-east trending fault were spaced very close together. Therefore, to improve image clarity, only thirteen of the total sixteen profiles were included on Figure 33. Appendix A contains all unfiltered and filtered VLF measurements that were conducted as part of this study.

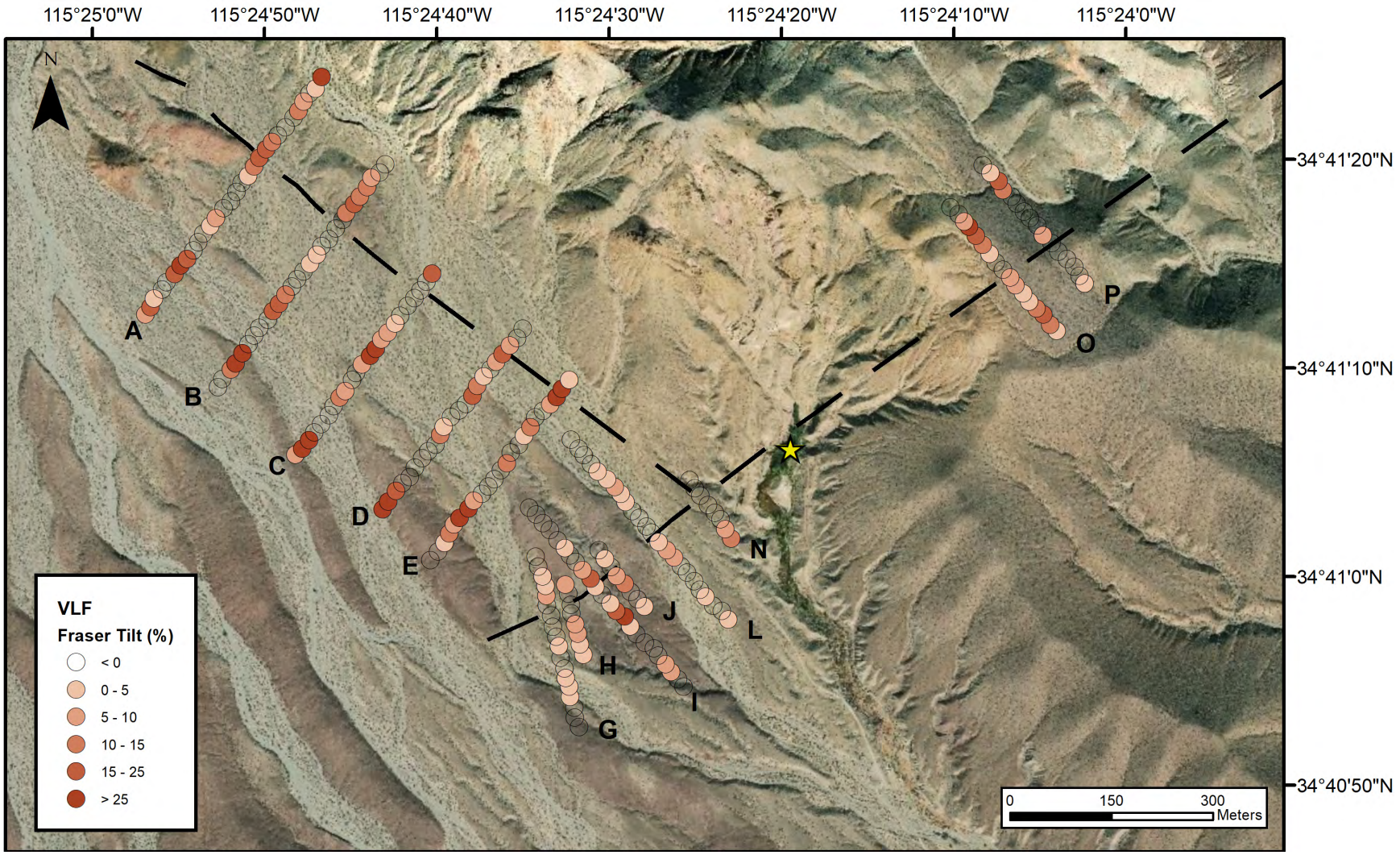

Figure 32: Map of VLF data with Fraser filtered tilt values displayed as points. Yellow star location of Bonanza Springs. Dashed black lines represent mapped location of fault zones from Kenney and Foreman (2018). Profiles across north-west trending fault shown for the 24.8 kHz frequency source and conducted from south-west to north-east. Profiles across north-east trending fault shown for the 25.2 kHz frequency and conducted from south-east to north-west.

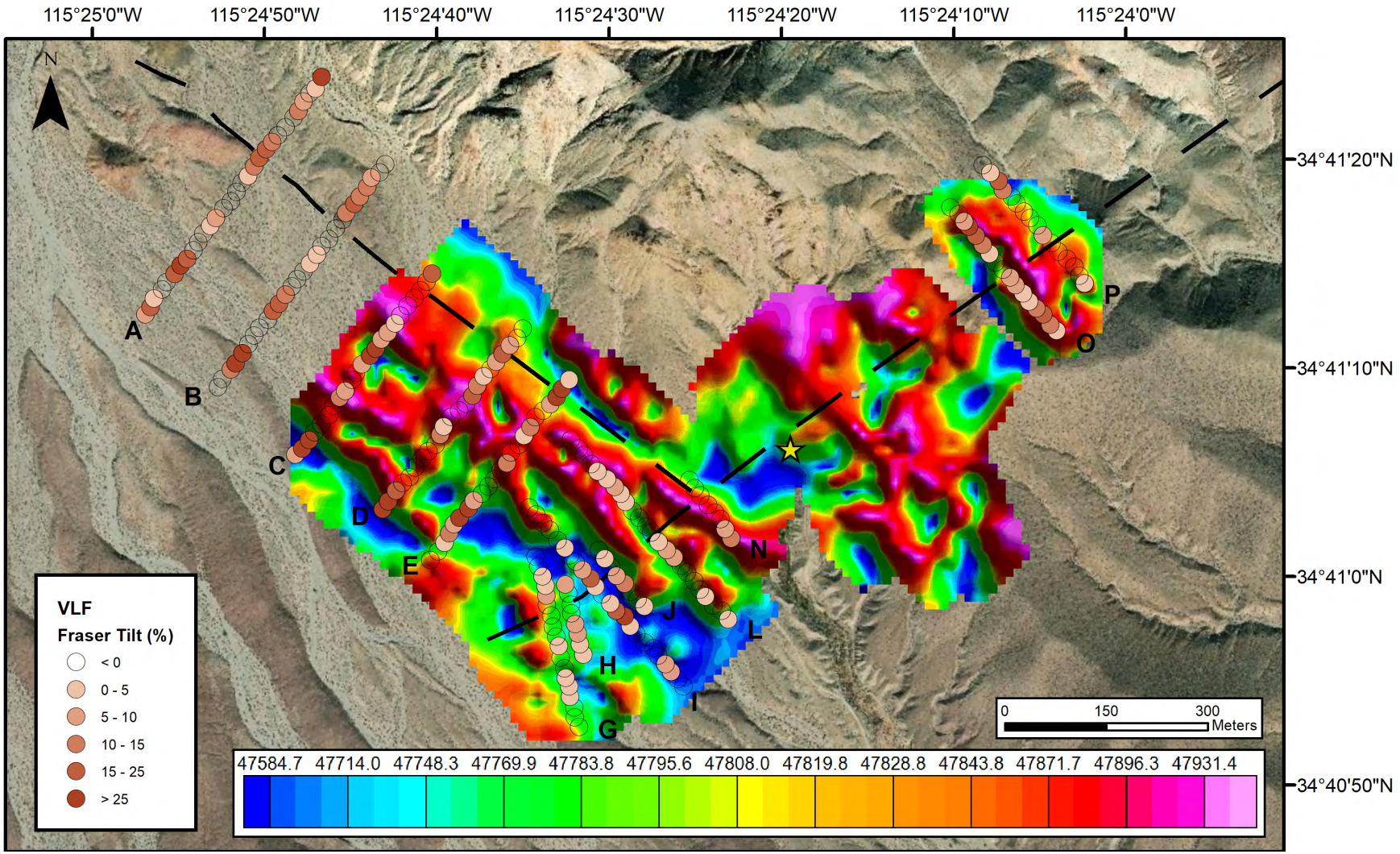

Figure 33: Map of VLF data overlain on the magnetic data described in Figure 31. Symbols, colors and lines as in Figure 32

Figure 34 contains the Fraser filtered values for VLF profile E, composed of 26 data points, and is approximately 380 m long. The mapped location of the north-west trending fault zone, as reported by Kenney and Foreman (2018), is represented by a black dashed line about 320 m along the profile length. There are two significant and broad peaks within profile E at 24.8 kHz, one at 31% tilt 100 m along the profile and another at 40% tilt 320 m along the profile. The second peak representing a 40% tilt is directly at the proposed location of the fault zone and correlates with the sharp total field intensity low in the vertical derivative magnetic data. The other peak representing a 31% tilt also correlates with a broad zone of magnetic lows discussed in the previous section. This 31% peak in the VLF data may further support the possible interpretation of that zone of magnetic lows as a broad saturated damage zone associated with the north-west trending fault zone or an additional highly conductive fault splay of similar strike.

VLF profile D includes 26 measurements over a 380 m long profile across the north-west trending fault zone (Figure 35). This profile contains one significant tilt signal peak

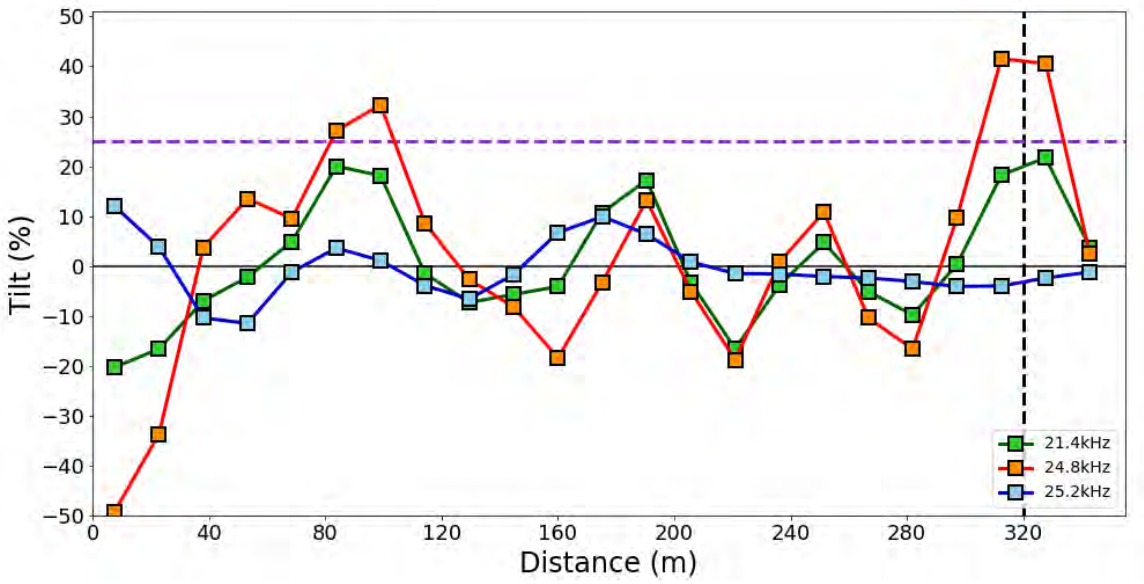

Figure 34: Fraser filtered in-phase tilt components for VLF profile E. Green, orange, and blue squares connected by lines represent Fraser filtered VLF data points at frequencies of 21.4 kHz, 24.8 kHz, and 25.2 kHz respectively and represent the Fraser filtered signal response. Fraser filtered points are located as discussed in section 2.1.3. Dashed vertical black line represents location of suspected fault zone along profile. Dashed horizontal green line indicates significant VLF measurement at >25% tilt.

for the 24.8 kHz source of 45% at 20 m along the profile path. From comparison with the magnetic data, this position correlates with another linear area of magnetic lows, although these lows are present on the outer edge of the interpolated grid. Since the gridding the data requires adjacent points to accurately interpolate values, the outer edges of the profile path produce less reliable results. There is another less significant peak of 16% at 220 m along the profile that also appears to correlate with a different linear magnetic low, a potential expression of a water saturated damage zone or small splay. There is another smaller peak of 16% tilt at approximately 300 m along the profile directly above the projected fault location. This is likely a further expression of the linear feature seen in profile E, although it is less conductive. The less conductive portion of this linear feature corresponds with a higher magnetic anomaly and may suggest the fault zone is less developed or less saturated in this location.

As in profile D, VLF profile C has a peak of 40% at about 20 m along its length (Figure 36). This peak also aligns with the linear magnetic low at the bottom edge of the magnetic grid, as well as with peaks in adjacent VLF profiles B and D. Another large peak exists at

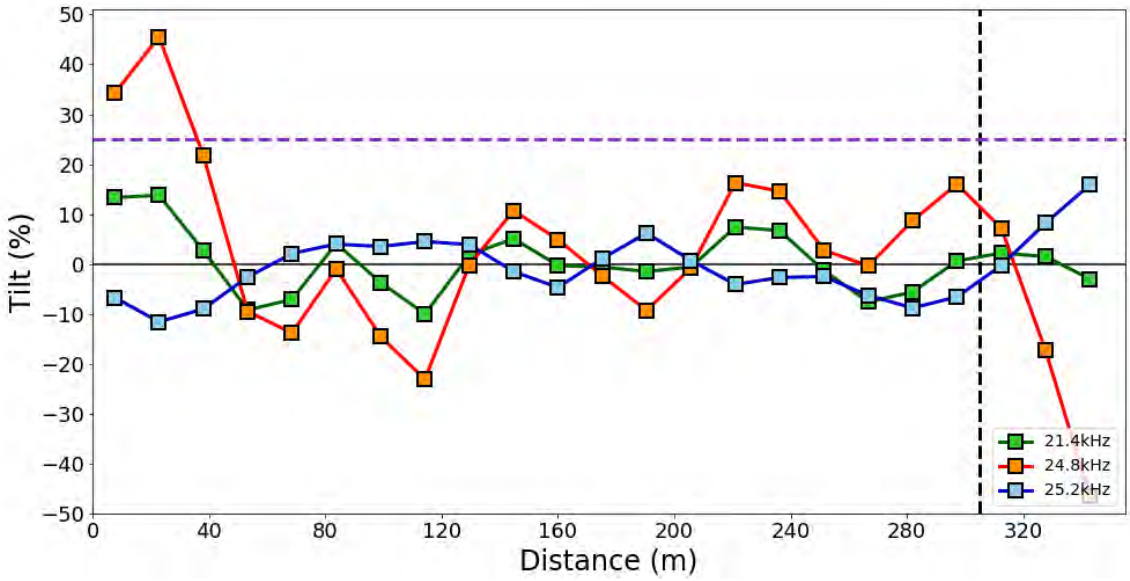

Figure 35: Fraser filtered in-phase tilt components for VLF profile D. All symbols, colors and lines as in Figure 34.

190 m along profile D of 35% tilt that corresponds with a linear magnetic low in the ground based magnetic data. Additionally, a less significant peak of 18.5% tilt is present at the end of profile D at the edge of the linear magnetic low feature to the north of the proposed fault. Similar to the response seen in profile D near the proposed fault zone, this more moderate VLF response could represent a younger and less developed fault zone or a fault zone that is not as saturated with groundwater. Alternatively, perhaps the fault strike is oriented at a greater azimuth and the VLF profiling is measuring the edge of a less conductive damage zone.

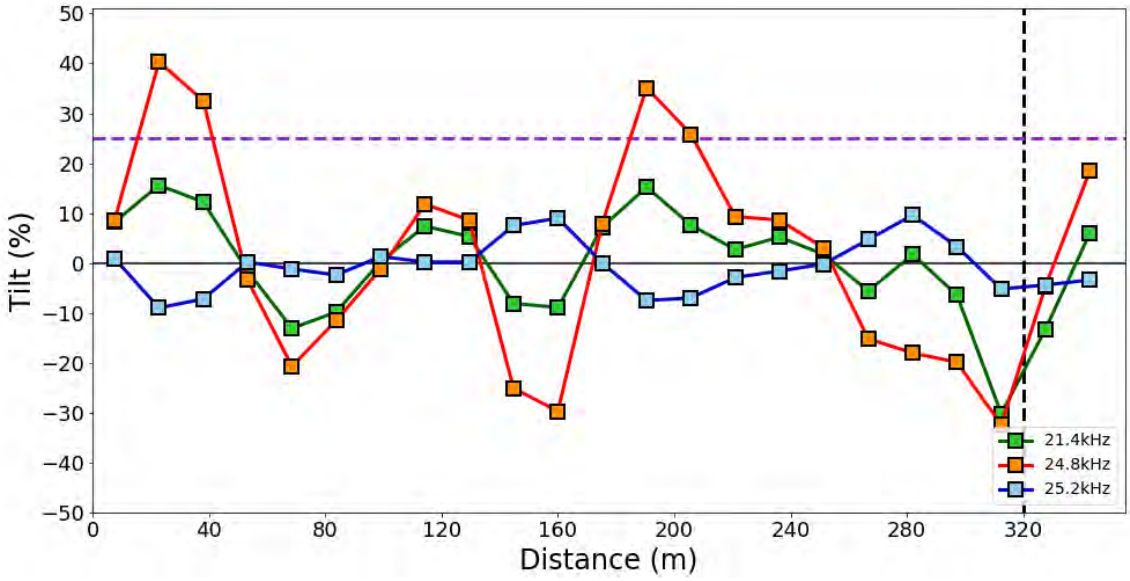

Figure 36: Fraser filtered in-phase tilt components for VLF profile C. All symbology as in Figure 34.

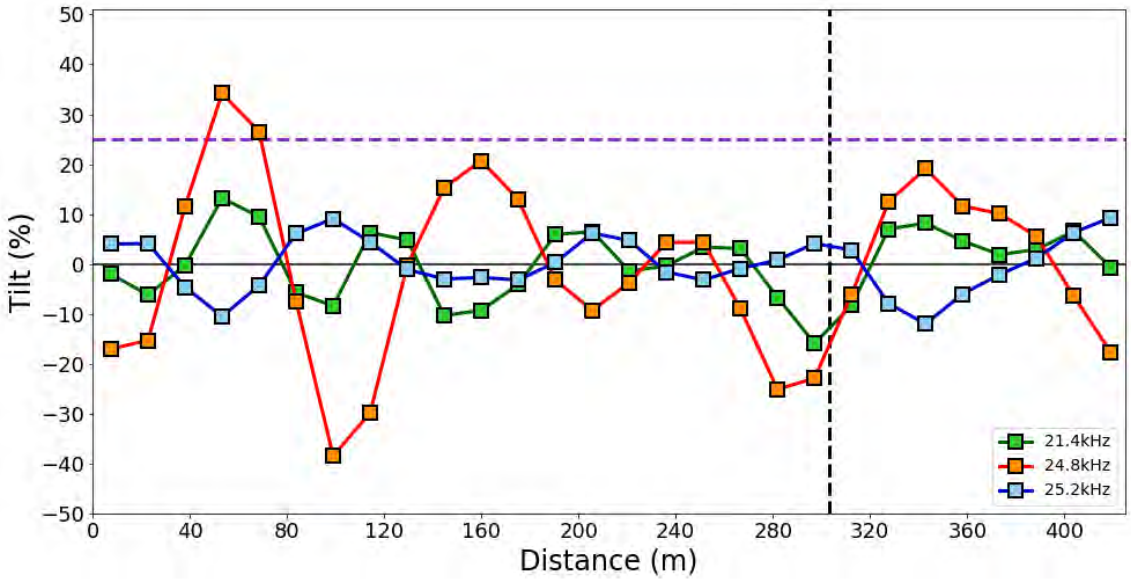

Figure 37: Fraser filtered in-phase tilt components for VLF profile B. All symbology as in Figure 34.

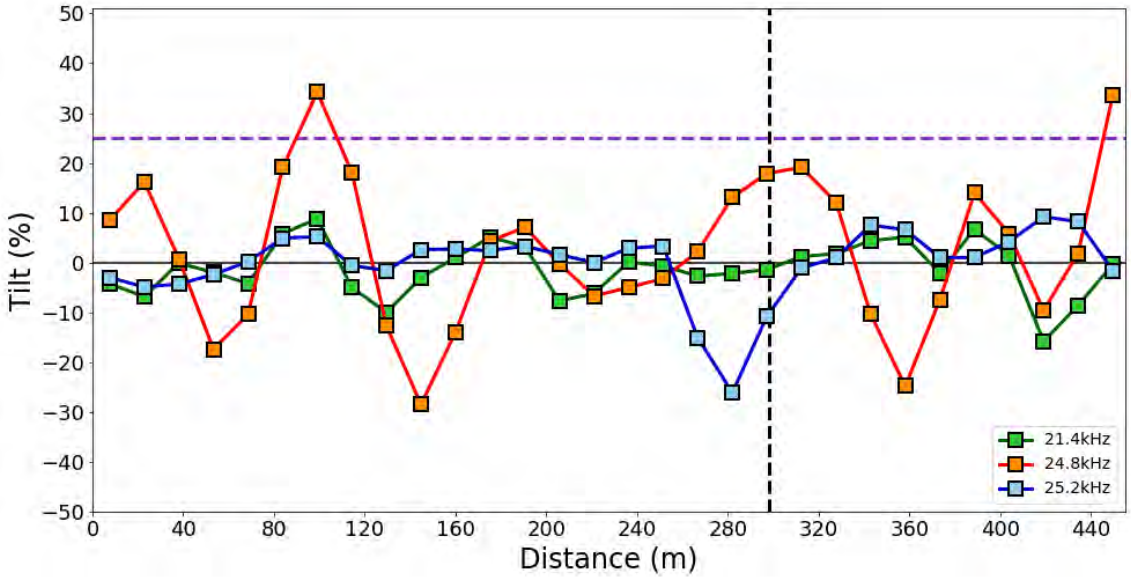

Figure 38: Fraser filtered in-phase tilt components for VLF profile A. All symbology as in Figure 34.

Profiles A (Figure 38) and B (Figure 37) are outside of the region covered by the magnetic data, but produce results that can be correlated with the other VLF profiles within the area. Along profile B, a peak of 24% 50 m along the profile is spatially aligned with similar highs along profiles C, D, and a moderate high at the beginning of profile A. At 100 m along profile A there is a prominent peak of 34% tilt that is aligned with a moderate peak of 20% at 160 meters along profile B and with another significant peak at profile C. Along the mapped location of the prospective fault zone profile A has a peak of 20% directly over the suspected fault location. Profile B has no response along the mapped fault, but further along the profile there is a peak of 20%. From Figure 33 profiles A - D possess significant peaks that align in a north-west trend, but it is unknown if the linear magnetic low aligned with the high VLF tilt angles of profiles C and D continues north-west towards profiles A and B.

Surveying done across the north-east trending fault zone produced little to no significant signal response in the VLF data. Profiles F through N were taken south-west of the spring and, with exception of profile I, all show similar results. Figure 39 shows VLF profile L, which is largely representative of the results of the other nearby profiles. VLF tilt readings

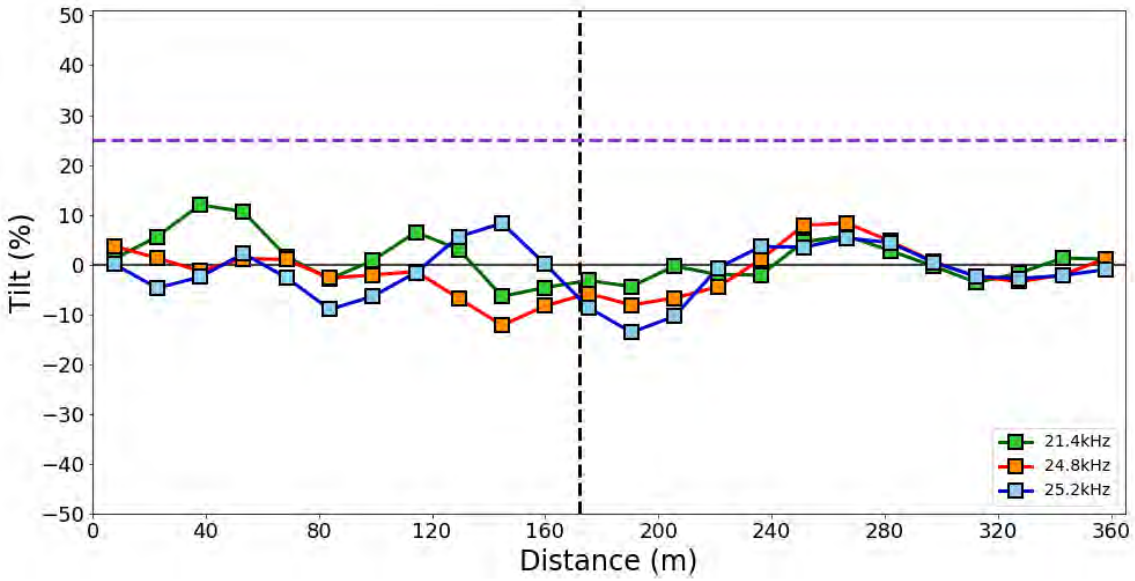

Figure 39: Fraser filtered in-phase tilt components for VLF profile L. All symbology as in Figure 34.

at 25.2 kHz show minor responses across the length of the profile with no significant peaks greater than 25% present. The highest peak in the 25.2 kHz range is a tilt angle of 8% at 145 m along the profile 25 m off from the location of the proposed fault zone. From Figure 33 there are similar signal responses at similar positions along other adjacent profiles. As previously noted, it is possible that minor signal responses as low as 5% could indicate a buried conducting body. Dailey et al. (2015) associated such minor tilt response in the 5% - 15% range with observed fault structures in their study of the western Mojave. However, there is no visible structure in the magnetic data that can be correlated with this minor response. In fact, there is a linear magnetic feature that passes almost completely perpendicular to the north-east trending fault zone. This linear feature better matches a significant signal response in profile E, suggesting that feature may be associated with a conducting body aligned along a similar strike to the nearby prospective north-west trending fault zone.

Aside from the minor responses in the 5% - 12% range, VLF profile I has the most significant tilt peaks of the surveying south-west of the spring. From Figure 40, there is a moderate signal of 15% tilt 220 m along the profile, near the hypothesized location of the fault zone, that aligns similarly with minor peaks on nearby profiles. There is also a more significant peak of 28% tilt 145 m along the profile path. Based on this large response and the minor responses from adjacent profiles, it is possible that there is a weaker conducting structure present near the mapped trace of the fault zone. Because there is also a large response in the 24.8 kHz frequency, it is possible that a structure is observed that is oriented with a more north-west strike. However, as previously discussed, the magnetic data that is overlain by VLF results in Figure 33 does not show any structure that corresponds with a linear feature oriented as the VLF data would suggest. An alternative interpretation is that the VLF profiling done in this area, especially for profiles G - J, is indicative of a structure other than the expected north-east trending fault zone. Figure 33 indicates that there is a linear zone of magnetic lows stretching from VLF profile E towards the south-east with a similar strike as the north-west trending fault zone. It continues until the edge of

available magnetic data and passes through VLF profiles G - J. If the linear magnetic low represents some subsurface structure, then the minor to significant tilt responses in those profiles within that magnetic low might be responses to that structure. Signal response strength is largely dependent on orientation of a conducting body relative to the VLF signal source, as well as orientation of the VLF profile. It may be the case that a subsurface conductor has been measured and is eliciting a relatively weak anomaly, because these profiles are closer to parallel to the potential conductor than perpendicular.

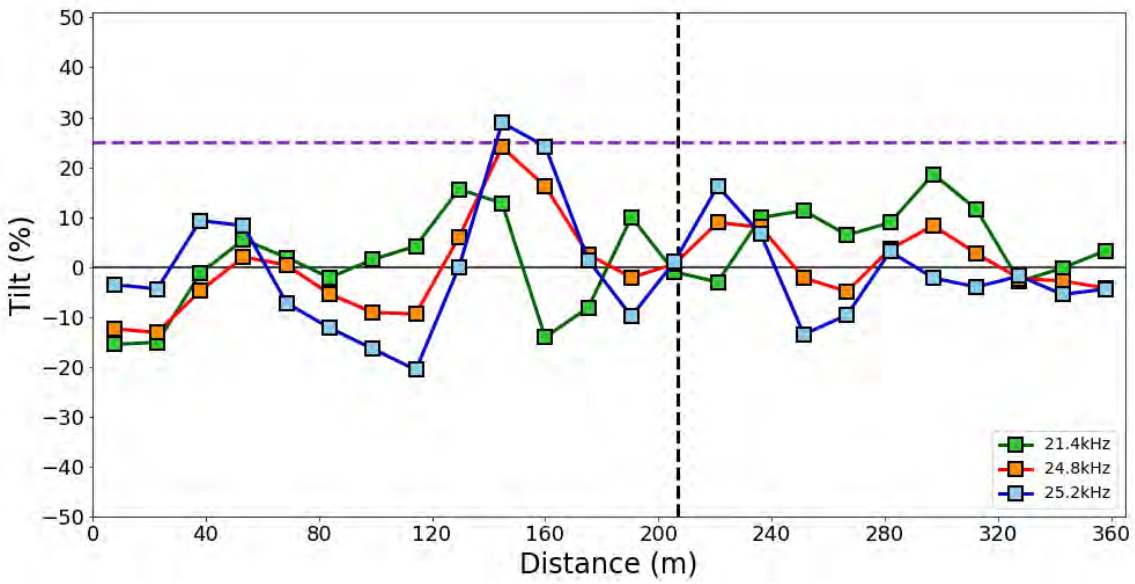

Figure 40: Fraser filtered in-phase tilt components for VLF profile I. All symbology as in Figure 34.

Two final profiles were taken across the north-east trending potential fault zone to the north-west of Bonanza Springs. Profiles O (Figure 41) and P (Figure 42) generally have similar results to the rest of the profiles taken across this fault zone: mostly low amplitude signal with a few moderate and significant responses. Based on the 25.2 kHz data, profile O has a significant tilt response of 27% at 205 m along profile length, while profile P has a moderate tilt response of 15% at 205 m along its length. These tilt signals align with each other and occur at similar points that may suggest a linear subsurface feature could be responsible. The magnetic data, however, does not appear to show any linear magnetic lows that would suggest a water saturated fault zone. However, these profiles were taken

at elevations roughly 40 m higher than the previous VLF profiles and the elevation of the spring itself. If the potentiometric surface of the groundwater that recharges the spring was near constant, there is the potential that this portion of the fault zone would not have become sufficiently weathered sufficiently close to the surface, to impart a prominent low magnetic anomaly in the data.

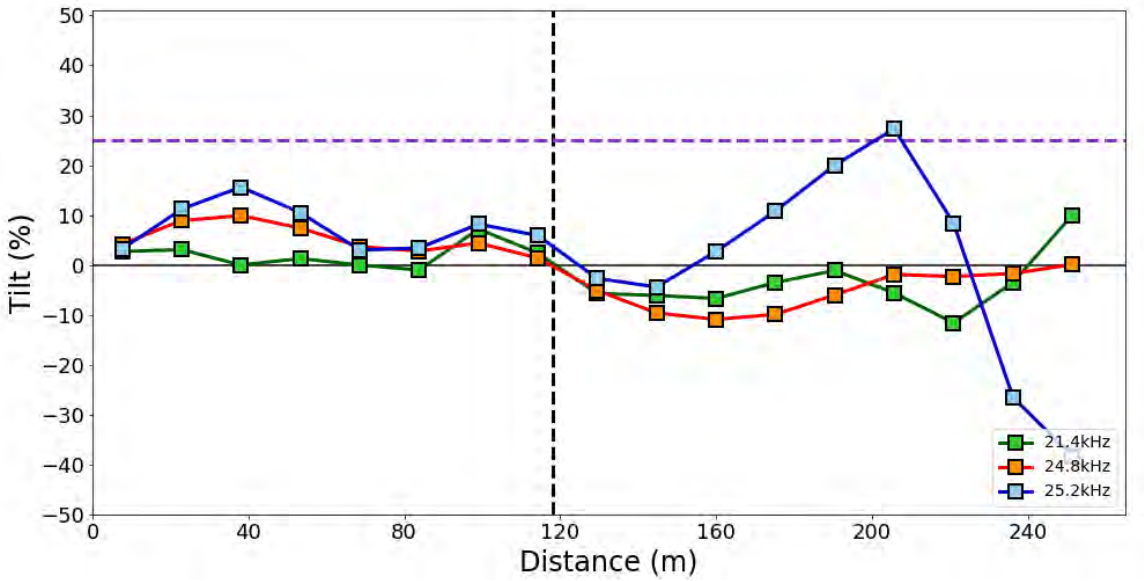

Figure 41: Fraser filtered in-phase tilt components for VLF profile O. All symbology as in Figure 34.

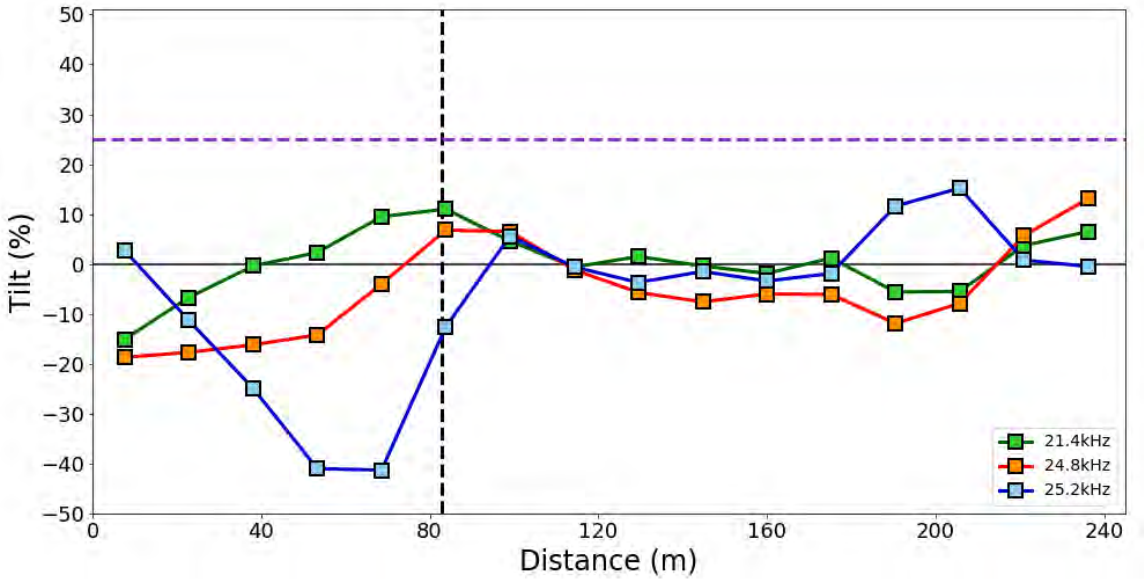

Figure 42: Fraser filtered in-phase tilt components for VLF profile P. All symbology as in Figure 34.

3.3 Resistivity

Resistivity surveys allowed for additional imaging of potential fault zone structures and the exploration of groundwater levels near the spring. Although difficulties were encountered during surveying, several profiles were successfully collected. The uneven terrain and numerous washes made finding an area where a full continuous profile could be laid out challenging. Additionally, the soil conditions of the study area were less than ideal and proved problematic for this type of surveys. Resistivity surveys require the ground to be somewhat conductive in order to carry current through the subsurface along the profile. The surface is composed of mostly unconsolidated alluvium and colluvium washed down from the hills to the north that is loosely cemented into a poorly sorted mixture of pebbles and

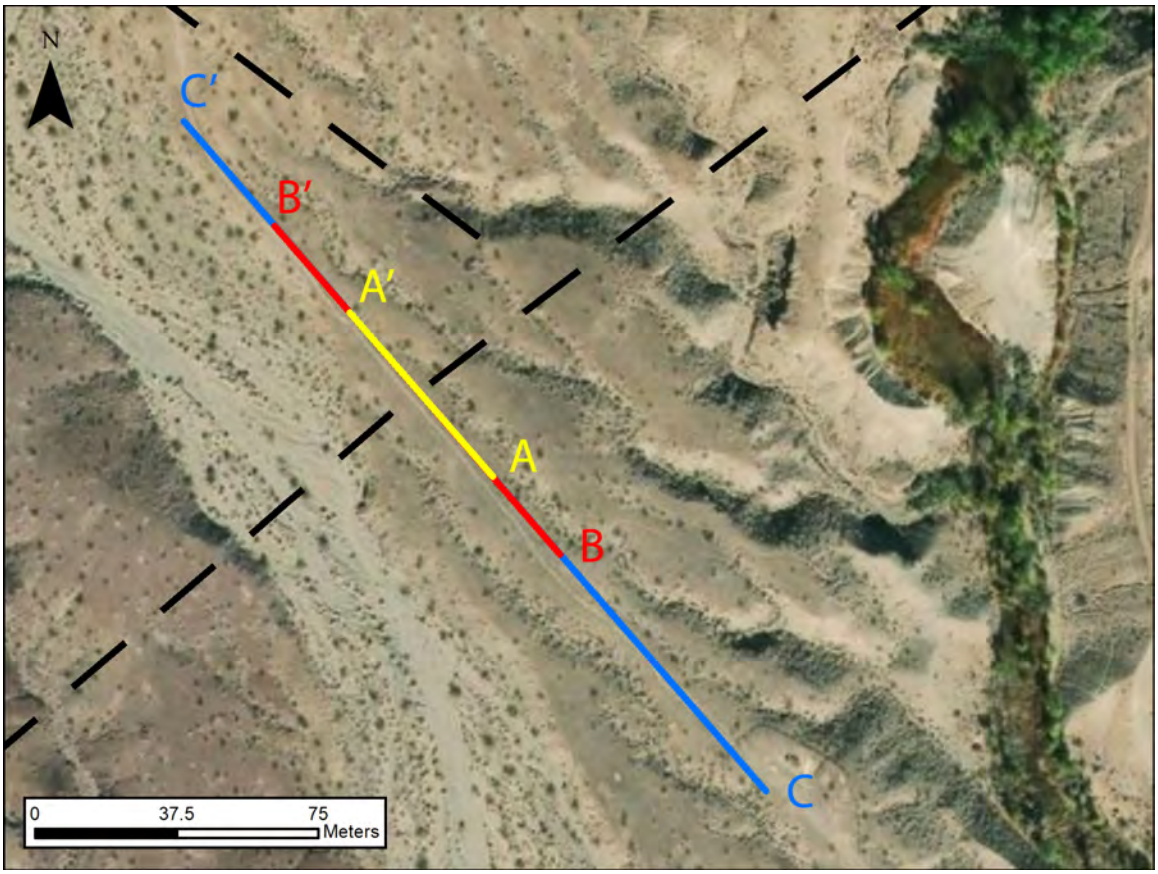

Figure 43: Map of resistivity surveys conducted at Bonanza Springs, same area as indicated by the red box in Figure 8. Dashed black lines represent the projected fault systems; resistivity profiles were performed across the north-east trending fault zone. Blue, red, and yellow lines represent resistivity surveys at electrode spacings of 10 m, 5 m, and 2.5 m respectively. A portion of the spring is visible in the upper right.

cobbles. The composition of the surface regolith made insertion of electrodes extremely difficult and labor intensive, limiting the depth the electrodes could be implanted into the ground. Additionally, a lack of recent precipitation in the area resulted in extremely dry soil conditions. The limited depth of electrode insertion and the arid conditions of the surface deposits made it difficult for electrode pairs to properly couple during surveying. Despite these limitations, data was obtained from resistivity surveys of the area. After several possible locations for resistivity profiles were attempted, and resulted in inadequate data, a relatively flat and even strip of land just to the west of the spring was found. This provided a suitable area for surveying and allowed for resistivity profiles directly across the north-east trending fault zone. Figure 43 shows the location of three resistivity surveys that were successfully completed at electrode spacings of 2.5 m, 5 m, and 10 m. The survey profiles were conducted across the mapped trace of the suspected north-east trending fault zone. The profiles at 2.5 m and 5 m electrode spacing were oriented so the center of each profile was directly over the mapped location of the fault from Kenney and Foreman (2018). Similar placement was attempted with the 10 m electrode spacing profile, but was ultimately prevented by a small cliff just to the north-west of the profile. Instead, it was relocated farther to the south-east to accommodate a continuous 230 m length of the profile.

Figure 44 shows the Res2DInv software model results for the resistivity profile across the north-east trending fault zone at 2.5 m electrode spacing. The profile had a total length of 57.5 m and the model that resulted from the inversion reaches a maximum depth of about 10 m. The predictions match the measurements well with an Root Mean Square (RMS) error (determined from a comparison of predicted resistivity values with the measurements) of 3.4%. Resistivity values range from 10 to 263 Ω·m with the relatively high resistivity values located near the surface. The upper 4 m of the resistivity model indicates a mostly continuous layer of material with a resistivity value of about 200 Ω·m. A small area towards the end of the profile has values of around 263 Ω·m and extends about 1.8 m into the subsurface. From about 4 - 5 m in the subsurface, there appear to be thin stratified lay-

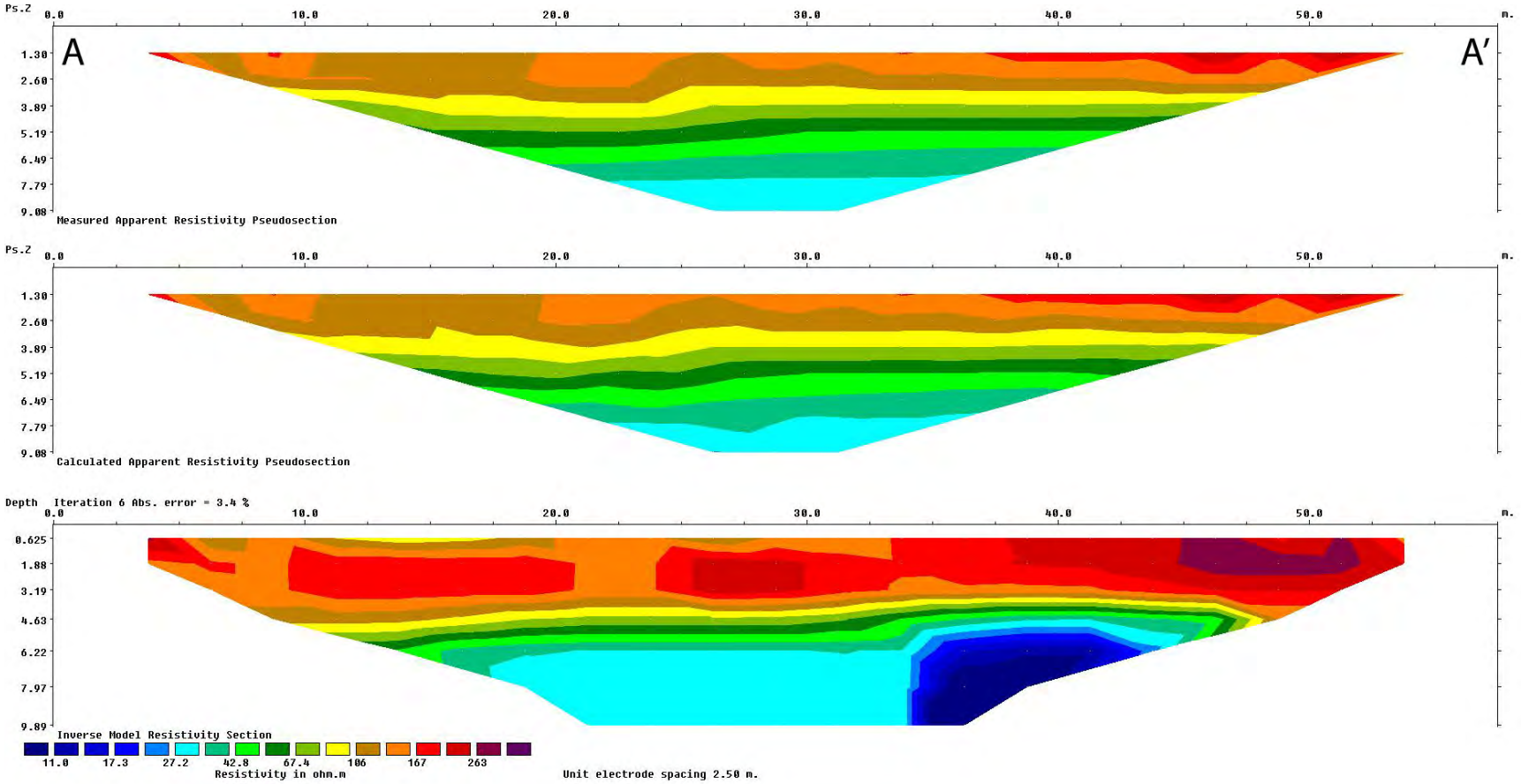

Figure 44: Res2DInv inversion model results for a resistivity profile conducted across the north-east trending fault zone with 2.5 m electrode spacing. Profile location visible in Figure 43 and running from the south-east towards the north-west. Cross-sections explained in detail in the caption for Figure 24.

ers of decreasing resistivity with depth; likely sedimentary layers that are possibly lightly saturated. At depths greater than 5 m down to the bottom of the model, relatively low resistivity of about 27 Ω·m potentially represents an region of saturated sediments and the depth to groundwater. The elevation of this profile is approximately 5 m above the spring. Therefore, if groundwater is discharging at the surface to feed the spring, it is highly likely this profile is viewing the water table or at least a heavily saturated zone.

Figure 45 shows additional model results for a profile across the north-east trending fault zone at 5 m electrode spacing. This profile had the same position as the previous one, as can be seen in Figure 43, but with a total survey length of 115 m. The previous midpoint was kept the same and positioned on top of the mapped location of the fault zone. 5 m of electrode spacing allowed for a depth of penetration of approximately 20 m, granting observations at double the depth of the 2.5 m spaced profile. Though an increased electrode spacing allows for greater depth of penetration, it also results in a lower model resolution. Despite the increase in distance between electrodes and the dry conditions of near surface regolith, the inversion model had a low error of 2.1%. The resistivity model at the bottom of Figure 45 shows similar structures as observed in the previous profile. There is 4 m thick zone near the surface in the 196 - 263 Ω·m range, followed by a thin stratified 1.5 - 2 m zone of decreasing resistivity values with depth, consistent with Figure 44. At a depth of 6.4 m within the model, resistivity values drop to around 27 Ω·m, though the layer containing this value is not as thick as in the previous profile, possibly due to a loss of near surface resolution due to the increase in electrode spacing. Instead, resistivity values rapidly drop to around 17 Ω·m and remain in that range until 20 m of depth where the model ends. The small zone of very low resistivity (11 - 17 Ω·m) seen in Figure 44 is instead a continuous layer that extends for about 14 m in this profile. The fairly continuous low resistivity values in Figure 45 are further indications of a depth to groundwater of around 6 m. Additionally, the shape of the low resistivity feature in the previous profile's depth model is not present in the profile with 5 m of electrode spacing, but now appears as a continuous layer extending

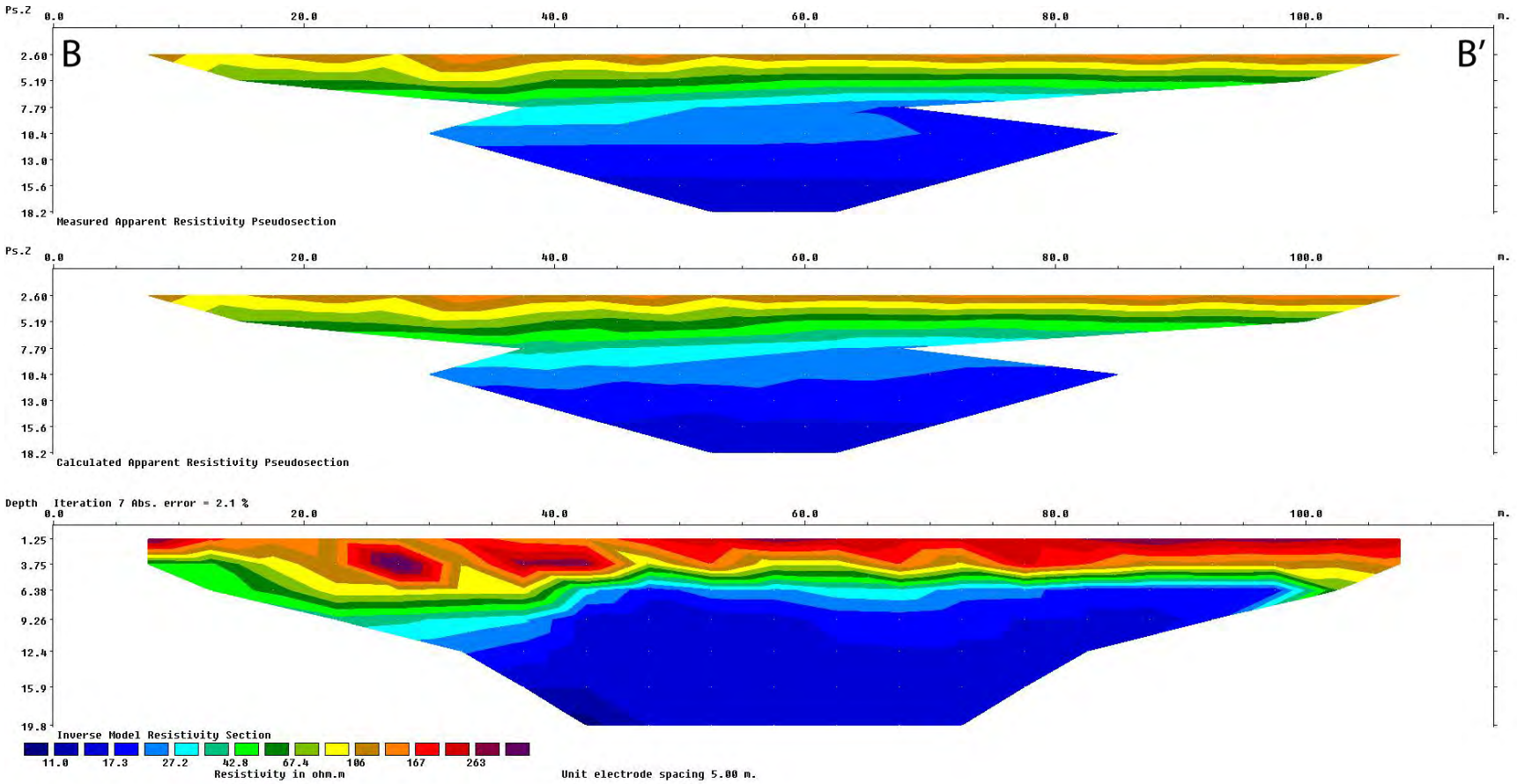

Figure 45: Res2DInv inversion model results for a resistivity profile conducted across the north-east trending fault zone with 5 m electrode spacing. Profile location visible in Figure 43 and runs from the south-east to the north-west. Model sections described in Figure 24. Missing ”slices” in the top two pseudo-sections due to the removal of low quality data points.

further down. The shape of that feature in Figure 44 may be due to edge effects and a lack of data below or adjacent to that area in the model inversion.

A third resistivity survey line was run at an electrode spacing of 10 m for a profile length of 230 m. This 230 m profile was intended to have the same mid point as the two previous surveys, but this placement was prevented by a small cliff with a steep drop north-west of the profile. As an alternative, the profile was moved farther south-east by approximately 20 m, but kept at the same trend as the previous two resistivity lines. Unfortunately the data quality for this profile was significantly lower than the previous two profiles and the model suffered from poor measurements that resulted in odd patterns of resistivity and high standard deviations. Figure 46 is a comparison of apparent resistivity values as a function of midpoint distance for profiles at three different electrode spacings. Standard deviations are plotted as error bars and for most points in the shorter spacing profiles, deviations are sufficiently small as to be obscured by the data symbols. After removal of very high deviations values via automatic filtering through the prosysII software many points with high deviations remain for the 10 m electrode spacing profile. Despite additional removal of data points with high standard deviations, the inversion model had an absolute error of 26.8% and the apparent resistivity predictions of the model do not match well with the measurements (Figure 47). Of note is one portion near the surface with values around 1,106 Ω·m and a portion at the very end of the profile of 7,520 Ω·m; values significantly higher than anything previously observed at similar depths. It is likely that the already poor site conditions for resistivity surveying were exacerbated by the increased distance between electrodes for this profile. Greater distance between electrodes results in increased current penetration, but also decreased current density resulting in low quality measurements if electrode coupling with the surface material is also poor.

The data that was not filtered out reveals data points with low q factors and consistently high resistivity values in the 1,000 - 2,000 Ω·m range. If the quality of the data is good and consistent, then potentially some highly resistive body is present and is distorting current

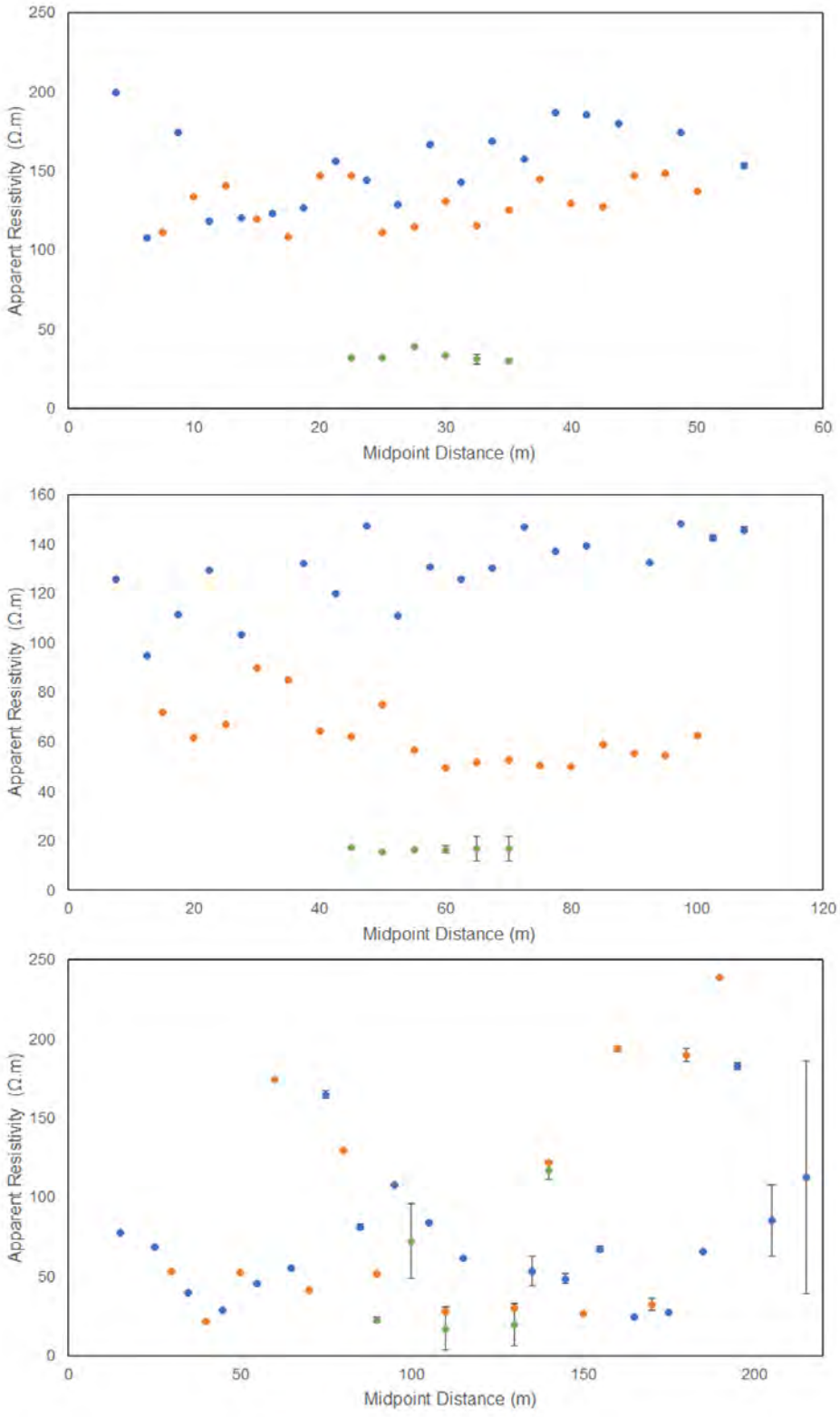

Figure 46: Apparent resistivity as a function of midpoint distance along profile for 2.5 m (Top) 5 m (Middle) and 10 m (Bottom) of electrode spacing. Error bars represent standard deviation for each measurement point. Colored points represent the first three depth levels 1 (Blue), 2 (Orange), and 3 (Green) for each profile. Depth level (n) approximates depth of current penetration as described in section 2.3.1.

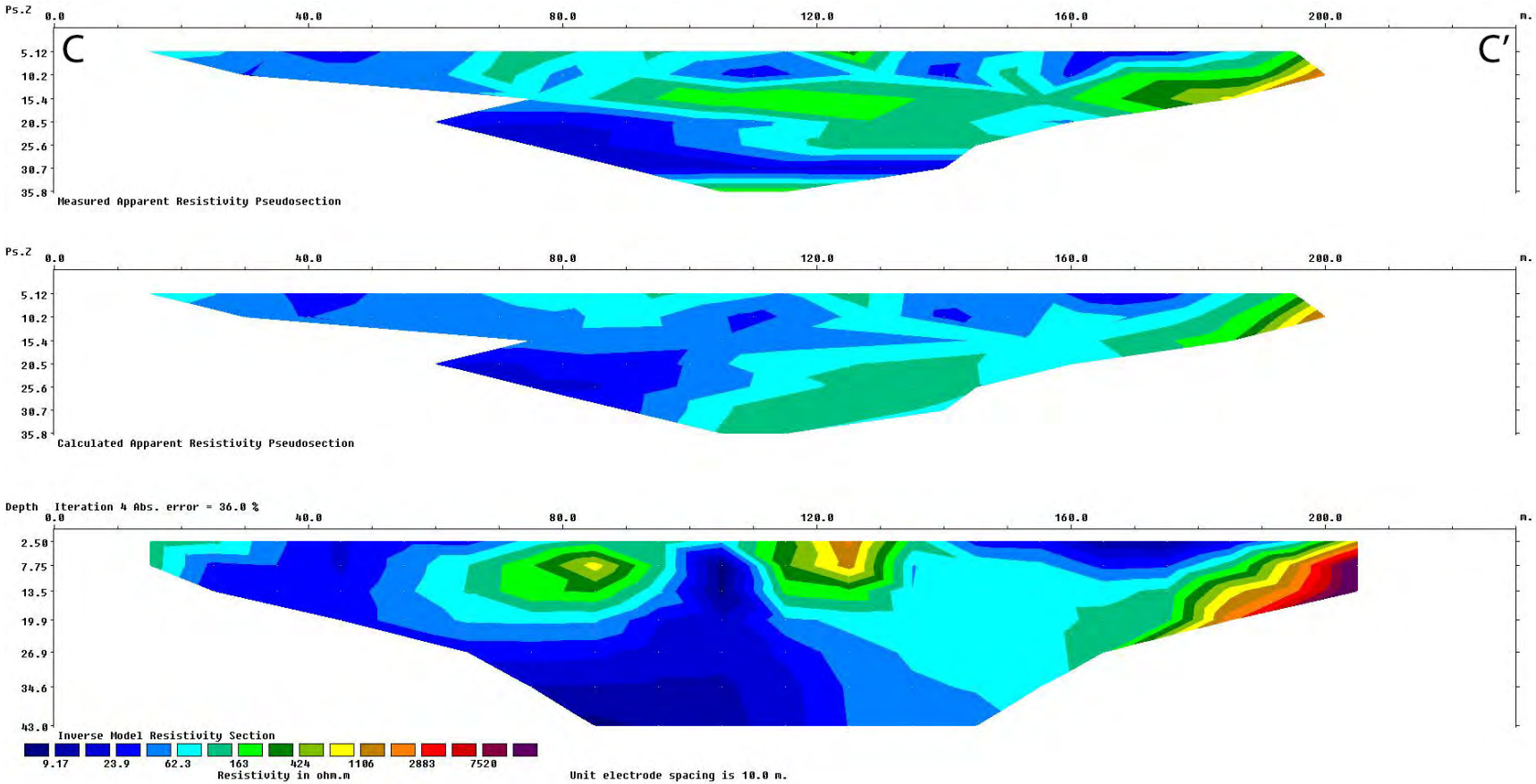

Figure 47: Res2DInv inversion model results for a resistivity profile conducted across the north-east trending fault zone with 10 m electrode spacing. Profile location visible in Figure 43 and runs from the south-east to the north-west. Model sections described in Figure 24. Missing ”slices” in the top two pseudo-sections due to the filtering out of low quality data points. Note the high absolute error in the inversion depth model.

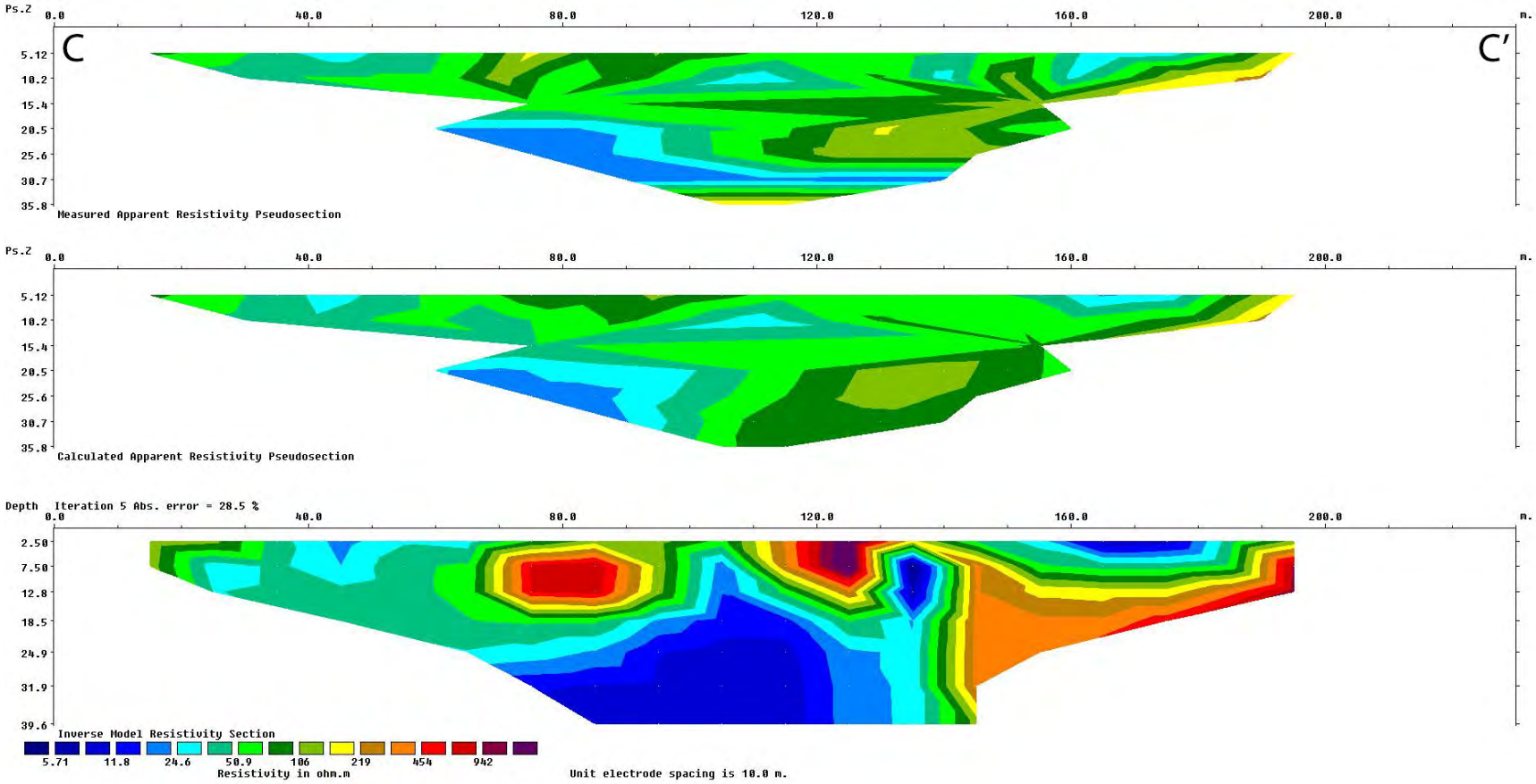

Figure 48: Res2DInv inversion model results for the same profile as Figure 47 but with another pass of filtering applied to remove abnormally high resistivity values. Improved filtering resulted in a reduction in absolute error of approximately 8%.

paths, such that parts of the subsurface are not well mapped. In an attempt to better examine the resistivity of the subsurface, several points with very high resistivity values ($>$ 900 Ω·m) were manually removed from the dataset, in addition to those already filtered out by the inversion software. A subsequent inversion resulted in Figure 48 with marginally better results in the depth model and an absolute error of 28.5%, a reduction in the absolute error of about 8%. From this figure, more discernible structures can be observed in the subsurface. Two large bodies of highly resistive material near the surface remain in this model, but with values closer to the high resistivity layers seen in the previous profiles, but still fairly high at 400 - 800 Ω·m. There is an area of low resistivity material in the 11 - 24 Ω·m range similar to what was seen in Figures 44 and 45, however it is not an even layer as in those profiles. Also now present, is a prominent vertical feature at approximately 145 m along the profile. This vertical feature acts as a sharp transition from highly resistive material of about 454 Ω·m to 50 and eventually 24 Ω·m. The additional removal of data points helps to observe structures in the model, though the significant error of 28.5% should be noted when interpreting observed structures in this inversion model.

Figure 49 shows the depth models for all three profiles with dashed lines representing the location of the north-east trending fault zone along the profile line. The top most model of Figure 49 is of the resistivity profile with 2.5 m of electrode spacing. From the surface to about 4 m is a zone of highly resistive material ranging from 106 - 167 Ω·m as well as an area near the surface of about 263 Ω·m that is 50 m along the profile length. This highly resistive layer is most likely representative of dry loosely consolidated sediments. At greater depths in the model are what appear to be stratified sedimentary layers with resistivity continuing to decrease with depth, suggesting this a zone of variably saturated material. Of particular interest in this profile is a small zone of very low resistivity around 17 Ω·m found 30.4 m along the profile and beginning at about 6 m beneath the surface. The low resistivity values suggest highly saturated material and based on its shape and proximity to the mapped fault location, it could potentially represent mounding of groundwater behind

a fault. Alternatively, due to it occurring on the edge of the model and the structure not being represented in the 5 m electrode spacing model, it could be an edge effect generated during the inversion.

Looking at the middle model of Figure 49 gives a deeper view into the subsurface to about 20 m. The layers of dry and variably saturated sediments are again visible at consistent depths of 0 - 4 m and 4 - 6 m. What previously appeared to be mounding behind a fault, now looks like a continuous layer of saturated material with resistivity values of 11 - 17 Ω·m. There is no significant structural change in the layers of the depth model near the mapped location of the fault. However, at around 20 m along the profile there is a vertical drop off in the 42 Ω·m layers of about 3.5 m, that could represent slight vertical offset. Additionally, at 40 m along the profile, the highly saturated layer sees a drop off from 6 m - 11 m. This could show a minor amount of mounding behind a fault structure that would indicate a minor to moderate hydraulic barrier causing a drop in the potential groundwater elevation.

The bottom model of Figure 49 is of the profile with 10 m of electrode spacing and additional filtering to remove very high resistivity values. The thick near surface layer of high resistivity values is not seen in this depth model. Instead, there are two large areas near the surface composed of highly resistive material. Given the geology of the study area, the source of these highly resistive bodies is potentially large igneous cobbles buried the subsurface as the resistivity values in Figure 47 do match the lower range for igneous rock units (Figure 22. The vertical feature at 140 m along the profile matches the mapped location of the fault zone and said feature does cause a sharp change in resistivity across it. However, considering the orientation of the profile is from south-east to north-west, the right side of the fault in the model would be the expected location of lower resistive material as groundwater would originate from the recharge basin to the north and flow south. From the depth model the opposite is true, with low resistive material to the south and high resistive material to the north. Unfortunately the arid nature of the top of the soil,

the highly resistive material near the surface, and the large distance between electrodes likely disrupted current flow in the subsurface making imaging difficult for this survey line. Though this third model was included with the other two in Figure 49, it is inconsistent with the findings of the shorter spacing depth models. The 10 m electrode spacing inversion model was included with the other two for completeness, but differs greatly from the other profiles, showing different patterns with depth. The high error in this depth model does not provide confidence in these results, as compared to the other two profiles. The consistent shallow groundwater levels within the resistivity data support a scenario of uninterrupted groundwater flow across the proposed north-east trending zone. There could be other mechanisms occurring that control the location of the spring such as a contact spring system where high permeability material overlies low permeability or impermeable material. Groundwater may exist in shallow igneous units exhibiting secondary porosity features and at the contact with an adjacent impervious unit, that groundwater is then forced to the surface.

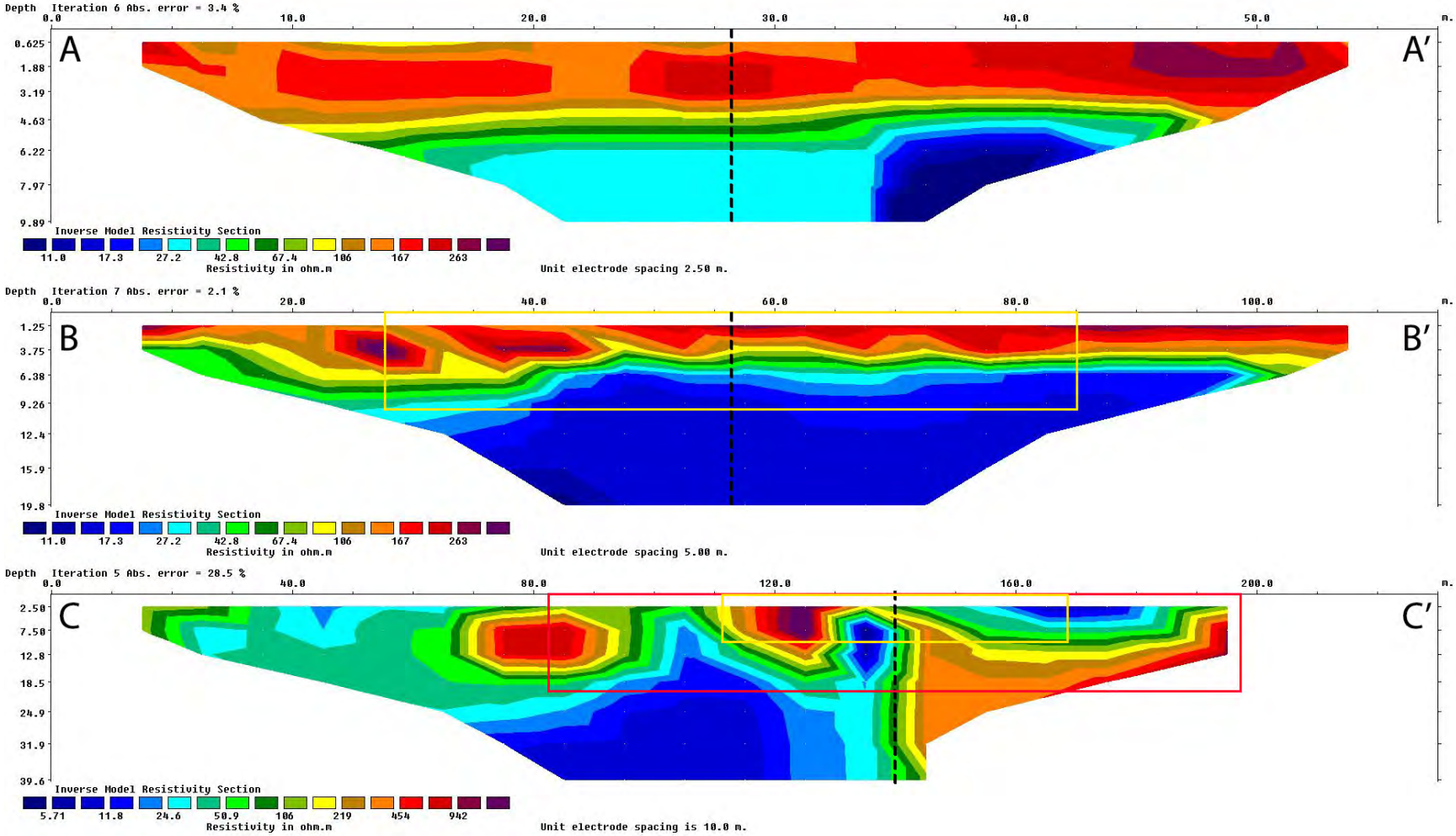

Figure 49: Comparison of the three depth models generated from resistivity profiling at 2.5 m (top), 5 m (middle), and 10 m (bottom) electrode spacings. Black dashed line represents approximate location of mapped fault zone along the profile length. Yellow box in middle and bottom depth models represents the area of extent of the top model, while the red box in the bottom model represents the area of extent of the middle model.

4 Conclusions

Bonanza Springs is a natural desert spring in the eastern Mojave that relies on annual precipitation recharge from a catchment basin in the Clipper Mountains to its immediate north. There are currently plans to extract groundwater from the Fenner Valley alluvial aquifer, approximately 15 km to the south, that may by hydraulically connected to the spring. The goal of this study was to examine the proposed existence of two potential fault zones that may converge near the spring and are suspected to act as hydraulic barriers to groundwater flow. A series of geophysical surveys were performed to image any subsurface structures with magnetic, VLF, and resistivity surveys taken across the proposed locations of both fault zones. Filtered total field intensity data from the magnetic surveying found a linear magnetic low that follows the north-west trending fault zone. Conversely, no trends in magnetic anomalies were discovered along the area of the proposed north-east trending fault zone. VLF data largely supports the findings of the magnetic surveys. Several moderate to high tilt anomalies were found along the north-west trending zone on or near the expected location of the fault. The VLF profiles taken across the north-east trending zone, however, show minor or no responses along the mapped location of the fault.

Resistivity profiles at electrode spacings of 2.5 m and 5 m show a sharp gradient to low resistivity values at about 5 m depth that likely indicates depth to groundwater. Additionally, some minor shallow structures were visible at depths of 6 - 7 m that show slight dipping in subsurface layers and gradual changes in resistivity values. Minor changes in resistivity values in the shorter profiles suggest the structure observed in the data may be due to stratigraphic changes rather than faulting offset.

Magnetics and VLF data showed consistent responses when profiling across the supposed location of the north-west trending fault zone, likely from the existence of a fault there. Gradual small changes in resistivity indicate no or a weak hydraulic barrier across the north-east trending potential fault. This and the lack of visible structures in the VLF

and mag data support the lack of a fault zone trending north-east across the spring. Consistent shallow groundwater levels strongly suggest that there is an uninterrupted flow of groundwater across the proposed north-east trending zone and there is likely no hydraulic barrier at this location. There are possible alternative mechanisms for the location of the spring such a contact spring system where porous rock overlies impermeable material. Additional surveying and future work would be necessary to determine the exact mechanism responsible for the spring's location.

5 Suggestions for Future Work

Magnetic and VLF surveys performed as part of this study covered most of the immediate area around Bonanza Springs. While careful and thorough efforts were made to obtain total coverage of the study area, the uneven terrain made this difficult to achieve. Future surveying that makes use of drone based magnetics would allow for navigation over areas of terrain unsuitable for walking magnetic surveys and allow for coverage of a larger area. Such an approach would also produce higher resolution data than traditional regional aeromagnetic surveys provide.

Identification of a possible fault along the proposed north-west trending fault zone was made through the use of magnetic and VLF surveying. Resistivity surveys done across this north-west trending zone would also provide insight into subsurface conditions along this zone. Similar surveying was done along the north-east trending zone, but surveys to greater depths experienced issues with data collection. Due to poor soil quality and the arid conditions of the site, additional surveys would prove difficult. For this reason, it is recommended that future surveys be performed during or soon after the wet winter months, when the ground is more saturated and electrode coupling can more easily occur during profiling. Additional methods of exploration geophysics may also prove useful for imaging the subsurface. Reflection surveys across the two suspected fault zones would provide data on any significant subsurface interfaces or the presence of any buried fault systems in the survey area. Ground Penetrating Radar (GPR) surveys would also provide valuable insight into shallow subsurface structures and any potential damage zones around the faults.

References

Ball, L. B., Ge, S., Caine, J. S., Revil, A., & Jardani, A. (2010). Constraining fault-zone hydrogeology through integrated hydrological and geoelectrical analysis. *Hydrogeology journal*, *18*(5), 1057–1067.

Baranov, V., & Naudy, H. (1964). Numerical calculation of the formula of reduction to the magnetic pole. *Geophysics*, *29*(1), 67–79.

Bense, V., Gleeson, T., Loveless, S., Bour, O., & Scibek, J. (2013). Fault zone hydrogeology. *Earth-Science Reviews*, *127*, 171–192.

Bense, V., & Person, M. (2006). Faults as conduit-barrier systems to fluid flow in siliciclastic sedimentary aquifers. *Water Resources Research*, *42*(5).

Bense, V., Van Balen, R., & De Vries, J. (2003). The impact of faults on the hydrogeological conditions in the roer valley rift system: an overview. *Netherlands Journal of Geosciences*, *82*(1), 41–54.

Bense, V., Van den Berg, E., & Van Balen, R. (2003). Deformation mechanisms and hydraulic properties of fault zones in unconsolidated sediments; the roer valley rift system, the netherlands. *Hydrogeology Journal*, *11*(3), 319–332.

Benson, R. C., Glaccum, R. A., & Noel, M. R. (1983). *Geophysical techniques for sensing buried wastes and waste migration*. Environmental Monitoring Systems Laboratory, Office of Research and Development, US Environmental Protection Agency.

Blakely, R. J., Connard, G. G., & Curto, J. B. (2016). Tilt derivative made easy. *Geosoft Technical Publications*, *4*, 30.

Bosch, F. P., & Müller, I. (2001). Continuous gradient vlf measurements: a new possibility for high resolution mapping of karst structures. *First Break*, *19*(6), 343–350.

Brown, A. (2013). *Review of the groundwater hydrology of the cadiz project* (Tech. Rep.). Aquilogic Inc.

Caine, J. S., Evans, J. P., & Forster, C. B. (1996). Fault zone architecture and permeability structure. *Geology*, *24*(11), 1025–1028.

Caine, J. S., & Minor, S. A. (2009). Structural and geochemical characteristics of faulted sediments and inferences on the role of water in deformation, rio grande rift, new mexico. *Geological Society of America Bulletin*, *121*(9-10), 1325–1340.

Carpenter, P., Ding, A., & Cheng, L. (2012). Identifying groundwater contamination using resistivity surveys at a landfill near maoming. *China. Nature Education Knowledge*, *3*(7), 20.

Chester, F., & Logan, J. M. (1986). Implications for mechanical properties of brittle faults from observations of the punchbowl fault zone, california. *Pure and applied geophysics*, *124*(1-2), 79–106.

Clark, D., & Emerson, D. (1991). Notes on rock magnetization characteristics in applied geophysical studies. *Exploration Geophysics*, *22*(3), 547–555.

Dailey, D., Sauck, W., Sultan, M., Milewski, A., Ahmed, M., Laton, W., ... Al Harbi, T. (2015). Geophysical, remote sensing, gis, and isotopic applications for a better understanding of the structural controls on groundwater flow in the mojave desert, california. *Journal of Hydrology: Regional Studies*, *3*, 211–232.

Evans, J. P., Forster, C. B., & Goddard, J. V. (1997). Permeability of fault-related rocks, and implications for hydraulic structure of fault zones. *Journal of structural Geology*, *19*(11), 1393–1404.

Faulkner, D., Jackson, C., Lunn, R., Schlische, R., Shipton, Z., Wibberley, C., & Withjack, M. (2010). A review of recent developments concerning the structure, mechanics and fluid flow properties of fault zones. *Journal of Structural Geology*, *32*(11), 1557–1575.

Foreman, T. (2010). *Groundwater management, monitoring, and mitigation plan* (Tech. Rep.). CH2M Hill.

Fraser, D. (1969). Contouring of vlf-em data. *Geophysics*, *34*(6), 958–967.

Henkel, H., & Guzman, M. (1977). Magnetic features of fracture zones. *Geoexploration*, *15*(3), 173–181.

Heynekamp, M. R., Goodwin, L. B., Mozley, P. S., & Haneberg, W. C. (1999). Controls on fault-zone architecture in poorly lithified sediments, rio grande rift, new mexico: Implications for fault-zone permeability and fluid flow. *Washington DC American Geophysical Union Geophysical Monograph Series*, *113*, 27–49.

Hrvoic, I. (1996). Requirements for obtaining high accuracy with proton magnetometers. In *Proceedings of the vith workshop on geomagnetic observatory instruments data acquisition and processing, dourbes, belgium* (pp. 4–10).

Illman, W. A., Liu, X., Takeuchi, S., Yeh, T.-C. J., Ando, K., & Saegusa, H. (2009). Hydraulic tomography in fractured granite: Mizunami underground research site, japan. *Water resources research*, *45*(1).

Kenney, M. D., & Foreman, T. L. (2018). *Updated assessment of cadiz water projects potential impacts to bonanza springs* (Tech. Rep.). Cadiz, Inc.

Krásny, J., & Sharp Jr, J. M. (2007). Introductory paper: Hydrogeology of fractured rocks from particular fractures to regional approaches: State-of-the-art and future challenges. In *Groundwater in fractured rocks* (pp. 17–46). CRC Press.

Loera, H. L., Leal, J. A. R., Harris, P. D., Gaytan, D. E. T., Ruiz, V. J. M., & Gogichaishvili, A. (2015). Geophysical exploration of fractured-media aquifers at the mexican mesa central: Satellite city, san luis potosí, mexico. *Surveys in Geophysics*, *36*(1), 167–184.

Loke, M. (2000). Electrical imaging surveys for environmental and engineering studies. *A practical guide to 2-D and 3-D surveys*, *2*.

Lopez-Loera, H., Urrutia-Fucugauchi, J., & Alva-Valdivia, L. M. (2010). Magnetic characteristics of fracture zones and constraints on the subsurface structure of the colima volcanic complex, western mexico. *Geosphere*, *6*(1), 35–46.

Love, A. H., & Zdon, A. (2018). Use of radiocarbon ages to narrow groundwater recharge

estimates in the southeastern mojave desert, usa. *Hydrology*, *5*(3), 51.

Marler, J., & Ge, S. (2003). The permeability of the elkhorn fault zone, south park, colorado. *Groundwater*, *41*(3), 321–332.

McNeill, J., & Labson, V. (1991). Geological mapping using vlf radio fields. In *Electromagnetic methods in applied geophysics: Volume 2, application, parts a and b* (pp. 521–640). Society of Exploration Geophysicists.

Miller, D. M., Miller, R. J., Nielsen, J. E., Wilshire, H. G., Howard, K. A., & Stone, P. (2007). Geologic map of the east mojave national scenic area, california. *USGS Bulletin*, *2160*, 48–64.

Miller, D. M., & Yount, J. C. (2002). Late cenozoic tectonic evolution of the north-central mojave desert inferred from fault history and physiographic evolution of the fort irwin area, california. *Geologic evolution of the Mojave Desert and southwestern basin and range: Geological Society of America Memoir*, *195*, 173–198.

Nabighian, M. N., Grauch, V., Hansen, R., LaFehr, T., Li, Y., Peirce, J., ... Ruder, M. (2005). The historical development of the magnetic method in exploration. *Geophysics*, *70*(6), 33ND–61ND.

Oldenburg, D. W., Li, Y., Farquharson, C. G., Kowalczyk, P., Aravanis, T., King, A., ... Watts, A. (1998). Applications of geophysical inversions in mineral exploration. *The Leading Edge*, *17*(4), 461–465.

Palacky, G. (1988). Resistivity characteristics of geologic targets. *Electromagnetic methods in applied geophysics*, *1*, 53–129.

Parsekian, A., Singha, K., Minsley, B. J., Holbrook, W. S., & Slater, L. (2015). Multiscale geophysical imaging of the critical zone. *Reviews of Geophysics*, *53*(1), 1–26.

Phillips, W., & Richards, W. (1975). Study of the effectiveness of the vlf method for the location of narrow-mineralized fault zones. *Geoexploration*, *13*(1-4), 215–226.

Rawling, G. C., & Goodwin, L. B. (2006). Structural record of the mechanical evolution of mixed zones in faulted poorly lithified sediments, rio grande rift, new mexico, usa.

Journal of Structural Geology, *28*(9), 1623–1639.

Reynolds, R., Fishman, N. S., & Hudson, M. R. (1991). Sources of aeromagnetic anomalies over cement oil field (oklahoma), simpson oil field (alaska), and the wyoming-idaho-utah thrust belt. *Geophysics*, *56*(5), 606–617.

Rogers, M., Cassidy, J., & Dragila, M. (2005). Ground-based magnetic surveys as a new technique to locate subsurface drainage pipes: a case study. *Applied Engineering in Agriculture*, *21*(3), 421–426.

Roux, A. (1967). The application of geophysics to gold exploration in south africa. *Mining and groundwater geophysics*, 425–438.

Saydam, A. S. (1981). Very low-frequency electromagnetic interpretation using tilt angle and ellipticity measurements. *Geophysics*, *46*(11), 1594–1605.

SMWD. (2011). *Cadiz valley water conservation, recovery, and storage project draft environemntal impact review* (Tech. Rep.). Santa Margarita Water District.

Spaid-Reitz, M. K., & Eick, P. (1998). Hram as a tool for petroleum system analysis and trend exploration: A case study of the mississippi delta survey, southeast louisiana. *Canadian Journal of Exploration Geophysics*, *34*(1-2), 83–96.

Stermer, D., & Matull, S. (2003). *Atlas of the biodiversity of california*. Department of Fish and Game.

Swain, C. (1976). A fortran iv program for interpolating irregularly spaced data using the difference equations for minimum curvature. *Computers & Geosciences*, *1*(4), 231–240.

Timur, E. (2012). Vlf-r studies in the agora of magnesia archaeological site, aydin, turkey. *Journal of Geophysics and Engineering*, *9*(6), 697–710.

USGS. (2000). *Review of the cadiz groundwater storage and dry-year supply program draft environmental planning technical report* (Vol. III). Needles CA USA: U. S. Geological Survey.

Vanneste, K., Verbeeck, K., & Petermans, T. (2008). Pseudo-3d imaging of a low-slip-

rate, active normal fault using shallow geophysical methods: The geleen fault in the belgian maas river valleyimaging a slow active normal fault in 3d. *Geophysics*, *73*(1), B1–B9.

Zdon, A., Davisson, M. L., & Love, A. H. (2015). Testing the established hydrogeologic model of source water to the amargosa river basin, inyo and san bernardino counties, california. *Environmental Forensics*, *16*(4), 344–355.

Zhang, Y., Schaubs, P., Zhao, C., Ord, A., Hobbs, B., & Barnicoat, A. (2008). Fault-related dilation, permeability enhancement, fluid flow and mineral precipitation patterns: numerical models. *Geological Society, London, Special Publications*, *299*(1), 239–255.

Zietz, I., & Andreasen, G. (1967). Remanent magnetization and aeromagnetic interpretation. *Mining geophysics*, *2*(1967), 569–590.

APPENDIX A

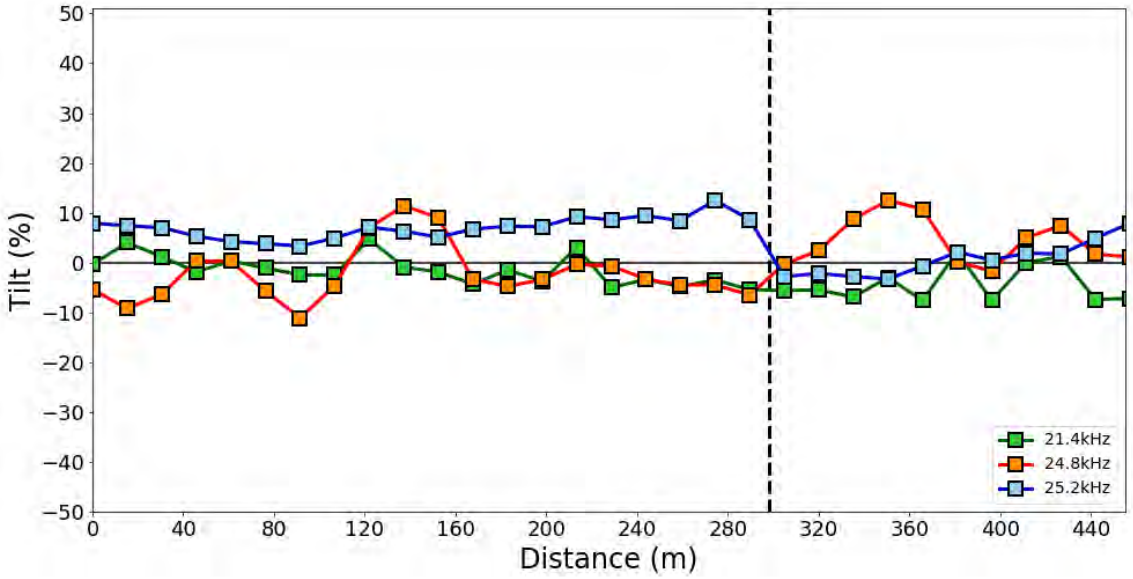

Figure 50: VLF profile A across north-west trending fault zone with the in-phase tilt components of three different frequencies collected. Green, orange, and blue squares with connecting lines are collected data points at frequencies of 21.4 kHz, 24.8 kHz, and 25.2 kHz respectively and represent the unfiltered VLF signal response. VLF points spaced approximately 15 m apart. Dashed vertical black line represents location of suspected fault zone along profile.

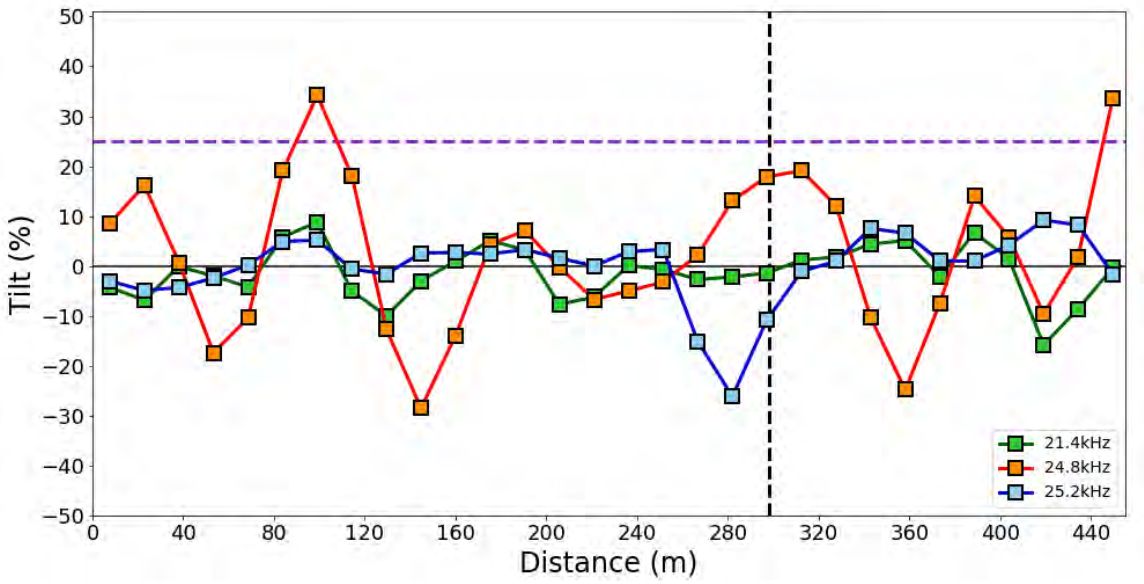

Figure 51: Fraser filtered in-phase tilt components for VLF profile A across north-west trending fault zone. Green, orange, and blue squares with connecting lines are the Fraser filtered VLF data points at frequencies of 21.4 kHz, 24.8 kHz, and 25.2 kHz respectively and represent the Fraser filtered signal response. Fraser filtered points spaced in between consecutive VLF data points as discussed in section 2.1.2. Dashed vertical black line represents location of suspected fault zone along profile. Dashed horizontal purple line indicates significant VLF measurement at >25% tilt.

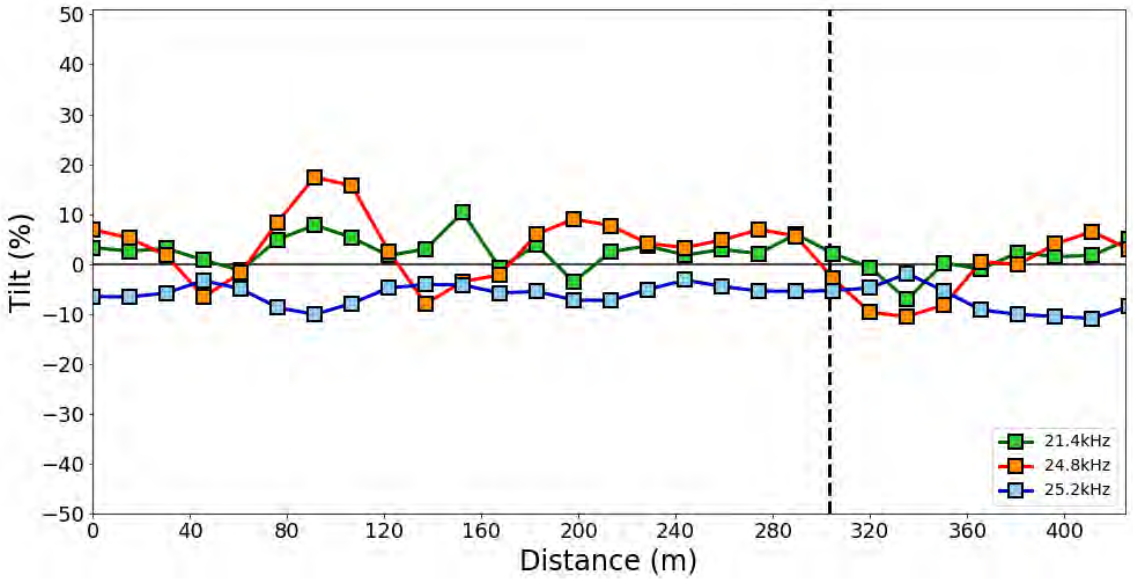

Figure 52: VLF profile B across north-west trending fault zone with the in-phase tilt components of three different frequencies collected. Same symbology and profile spacing as Figure 50.

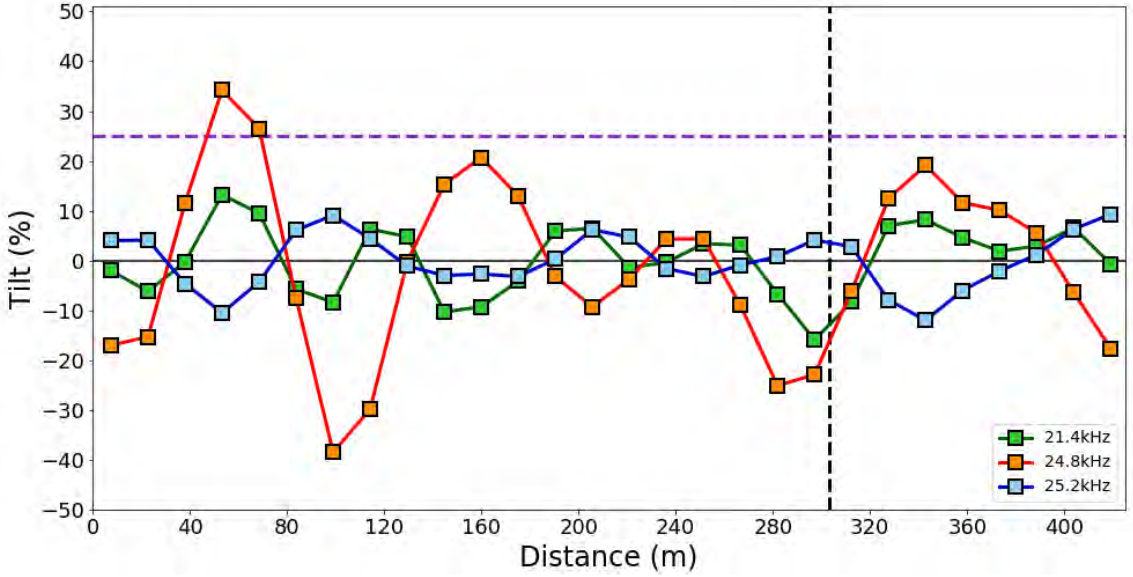

Figure 53: Fraser filtered in-phase tilt components for VLF profile B across north-west trending fault zone. Same symbology and point spacing as in Figure 51.

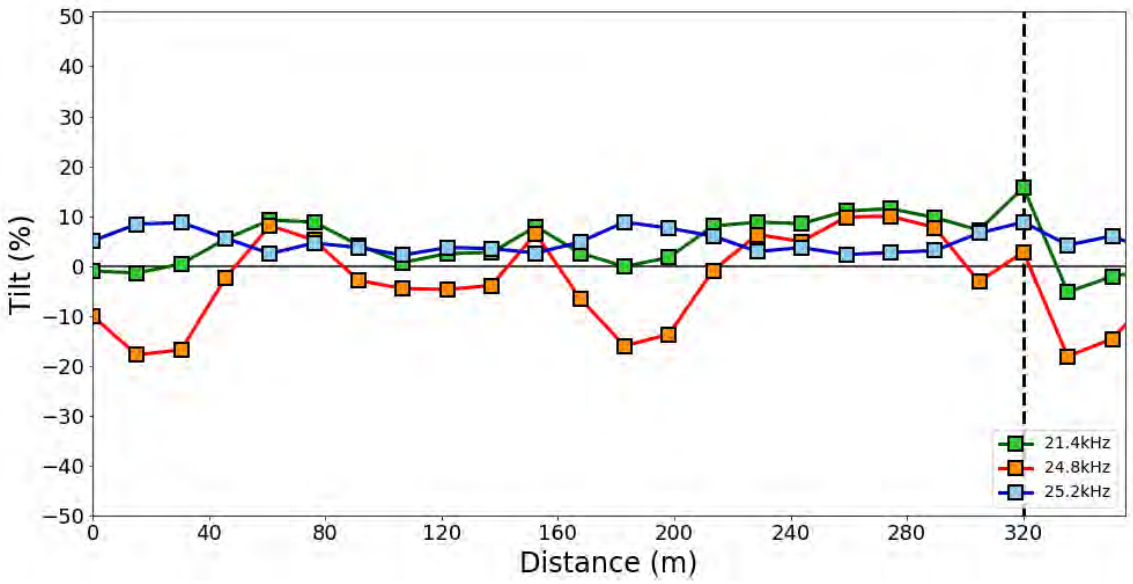

Figure 54: VLF profile C across north-west trending fault zone with the in-phase tilt components of three different frequencies collected. Same symbology and profile spacing as Figure 50.

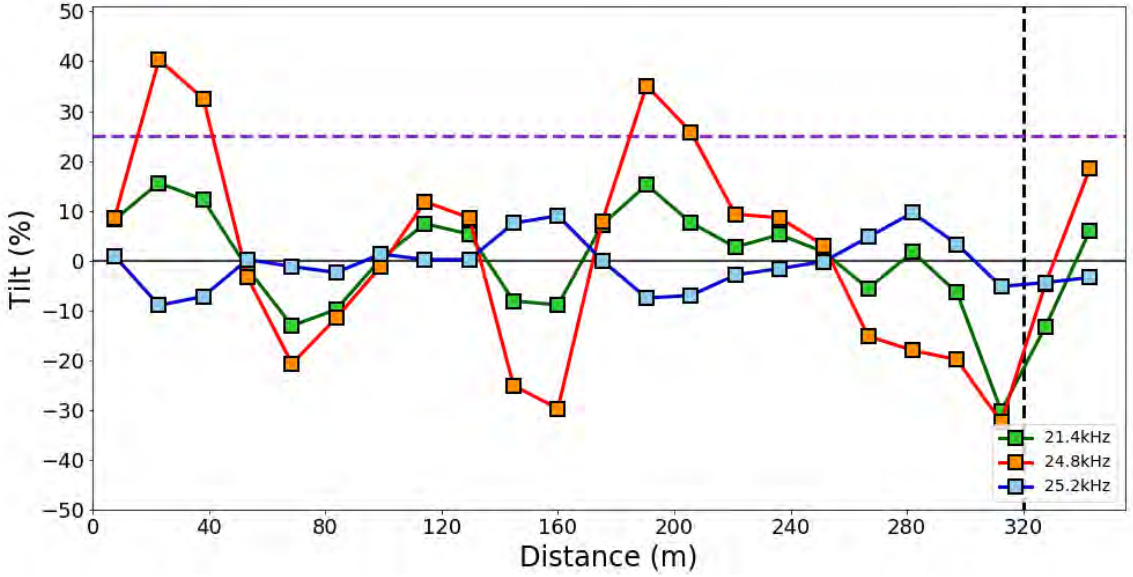

Figure 55: Fraser filtered in-phase tilt components for VLF profile C across north-west trending fault zone. Same symbology and point spacing as in Figure 51.

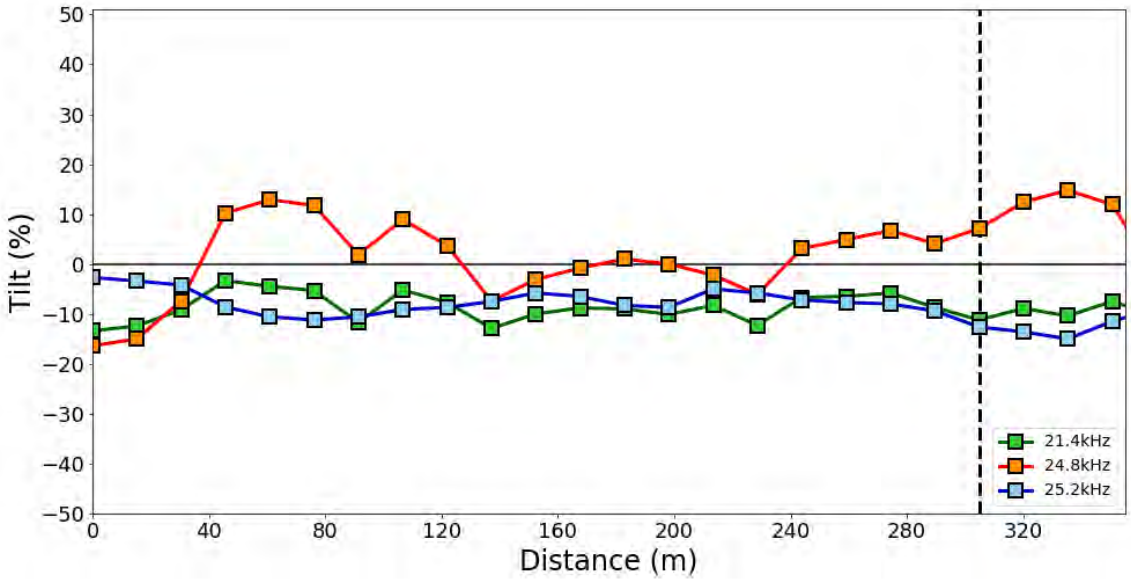

Figure 56: VLF profile D across north-west trending fault zone with the in-phase tilt components of three different frequencies collected. Same symbology and profile spacing as Figure 50.

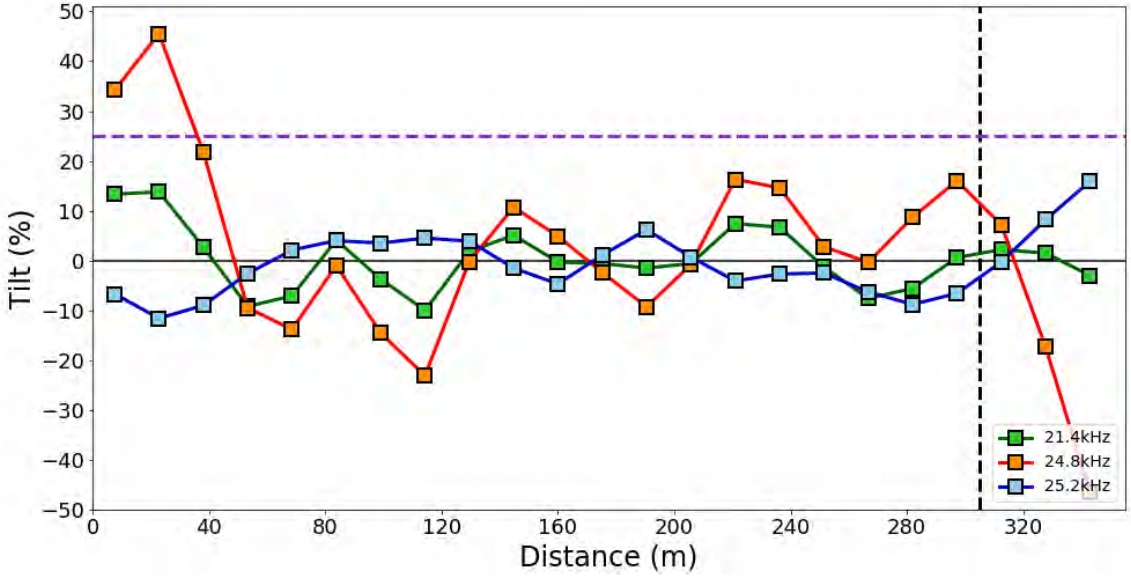

Figure 57: Fraser filtered in-phase tilt components for VLF profile D across north-west trending fault zone. Same symbology and point spacing as in Figure 51.

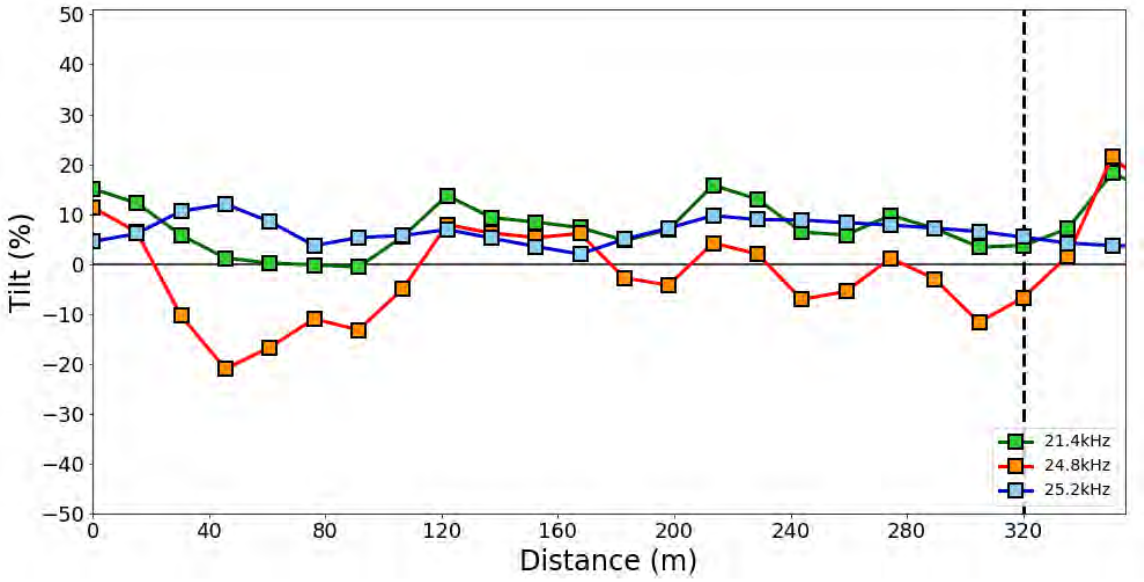

Figure 58: VLF profile E across north-west trending fault zone with the in-phase tilt components of three different frequencies collected. Same symbology and profile spacing as Figure 50.

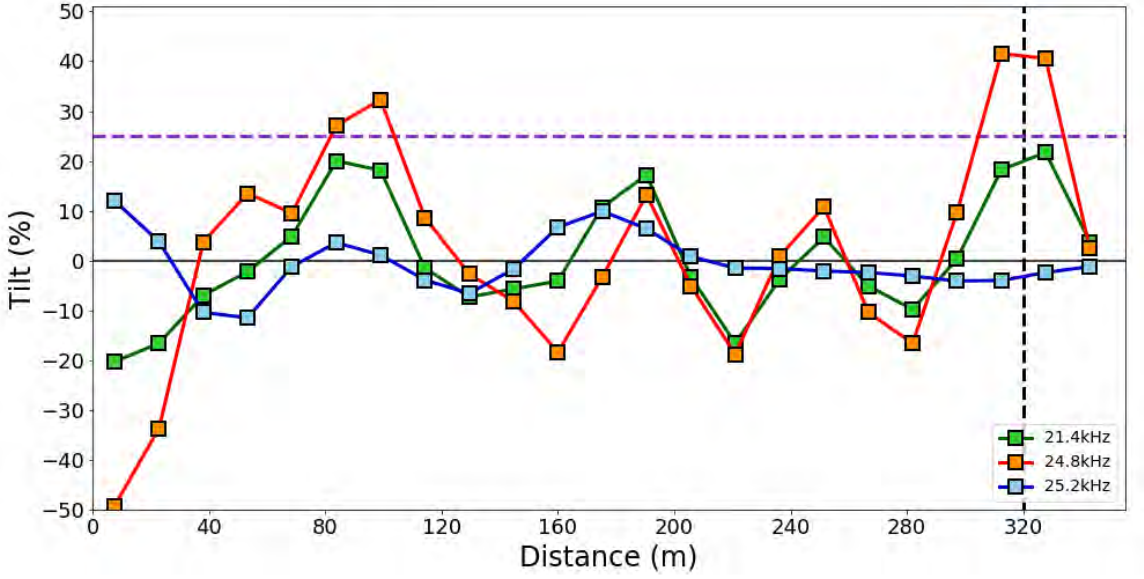

Figure 59: Fraser filtered in-phase tilt components for VLF profile E across north-west trending fault zone. Same symbology and point spacing as in Figure 51.

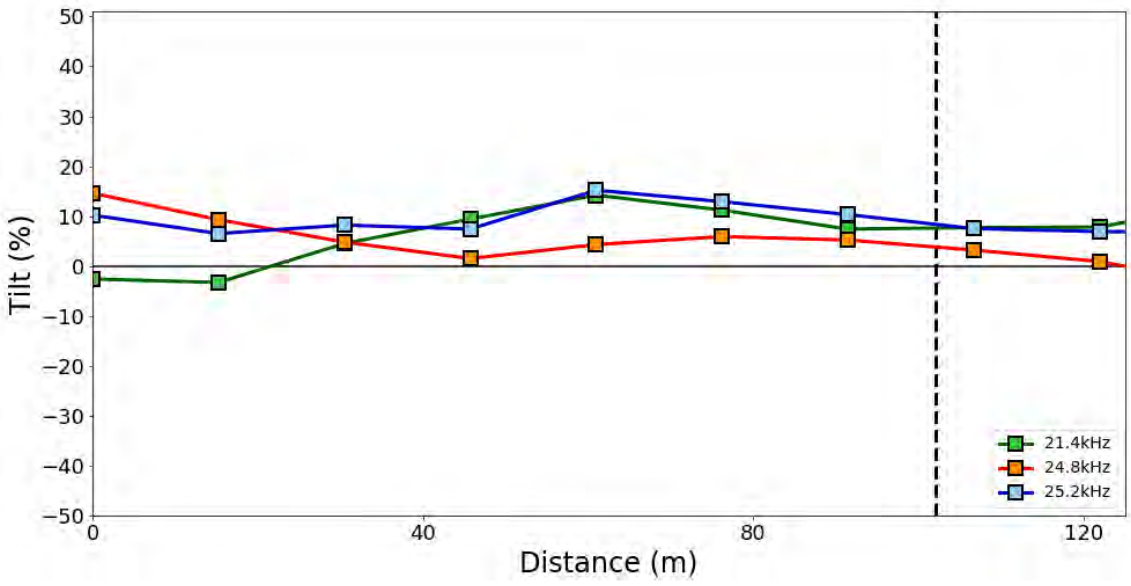

Figure 60: VLF profile F across north-east trending fault zone with the in-phase tilt components of three different frequencies collected. Same symbology and profile spacing as Figure 50.

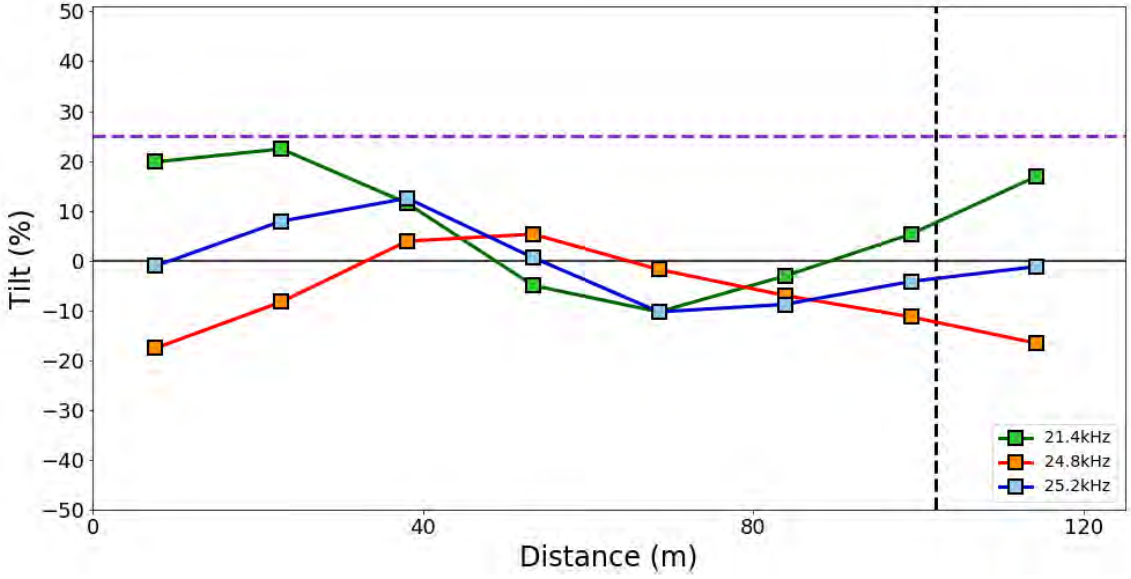

Figure 61: Fraser filtered in-phase tilt components for VLF profile F across north-east trending fault zone. Same symbology and point spacing as in Figure 51.

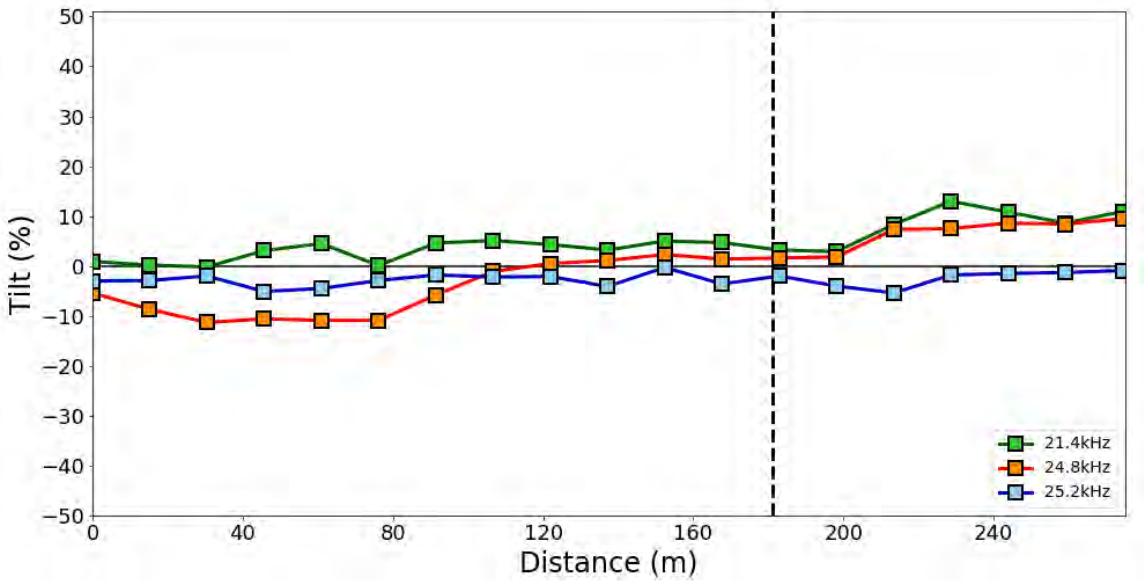

Figure 62: VLF profile G across north-east trending fault zone with the in-phase tilt components of three different frequencies collected. Same symbology and profile spacing as Figure 50.

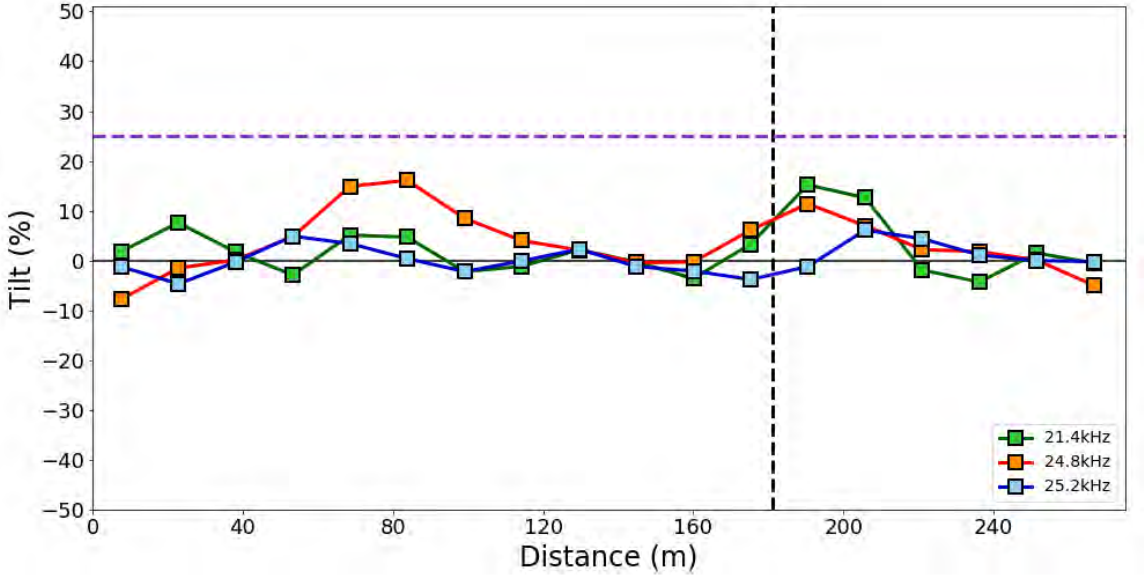

Figure 63: Fraser filtered in-phase tilt components for VLF profile G across north-east trending fault zone. Same symbology and point spacing as in Figure 51.

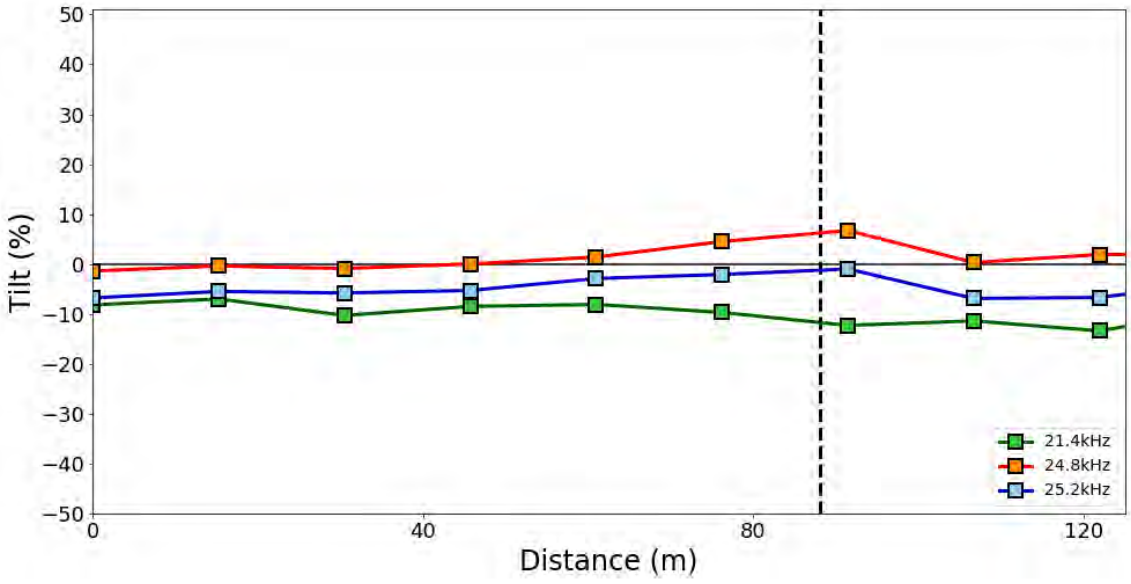

Figure 64: VLF profile H across north-east trending fault zone with the in-phase tilt components of three different frequencies collected. Same symbology and profile spacing as Figure 50.

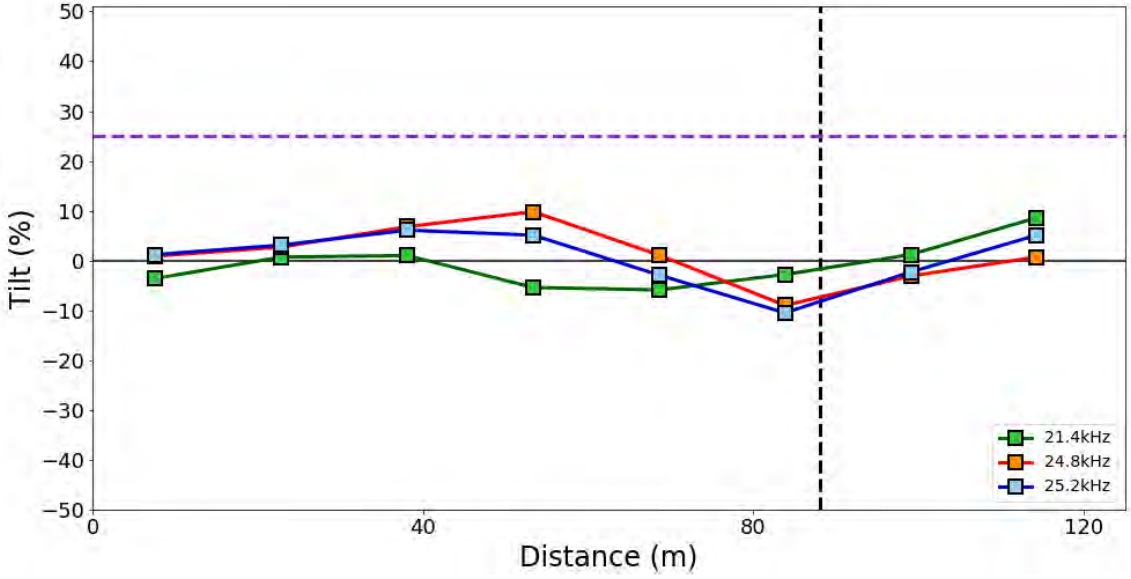

Figure 65: Fraser filtered in-phase tilt components for VLF profile H across north-east trending fault zone. Same symbology and point spacing as in Figure 51.

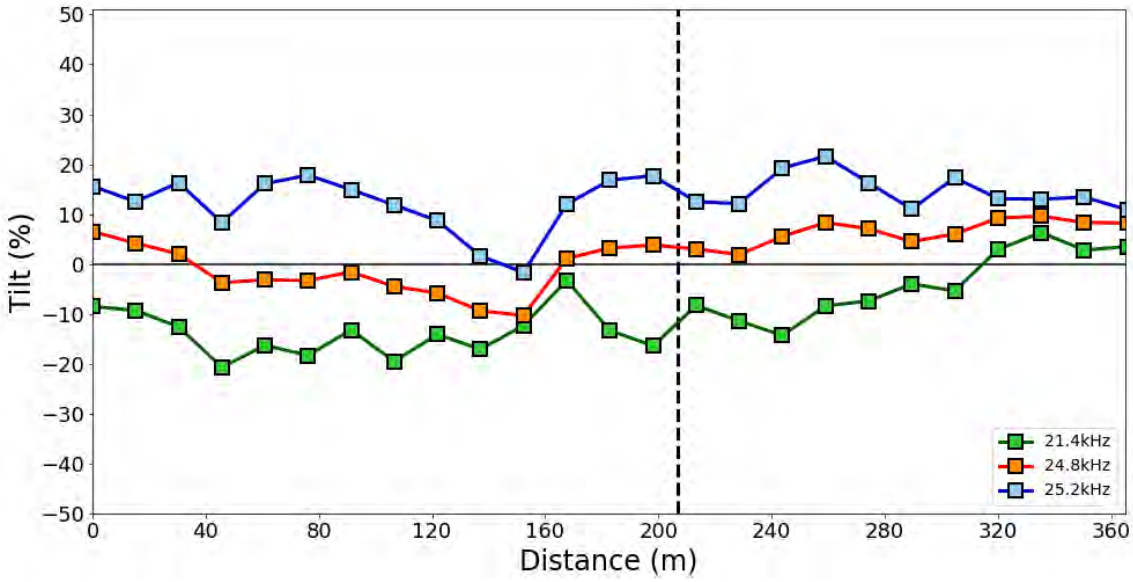

Figure 66: VLF profile I across north-east trending fault zone with the in-phase tilt components of three different frequencies collected. Same symbology and profile spacing as Figure 50.

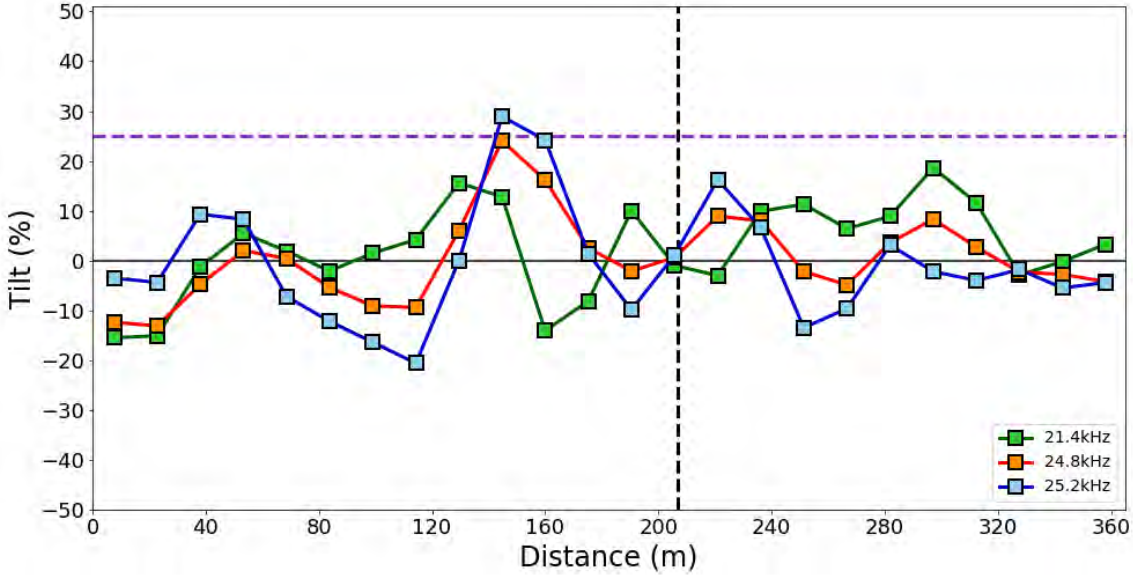

Figure 67: Fraser filtered in-phase tilt components for VLF profile I across north-east trending fault zone. Same symbology and point spacing as in Figure 51.

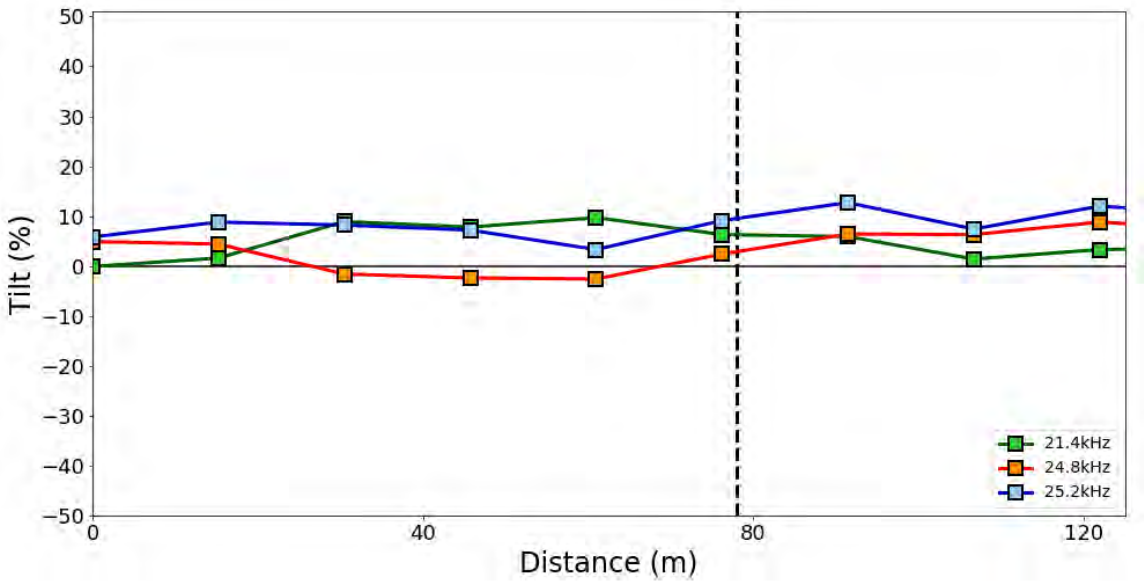

Figure 68: VLF profile J across north-east trending fault zone with the in-phase tilt components of three different frequencies collected. Same symbology and profile spacing as Figure 50.

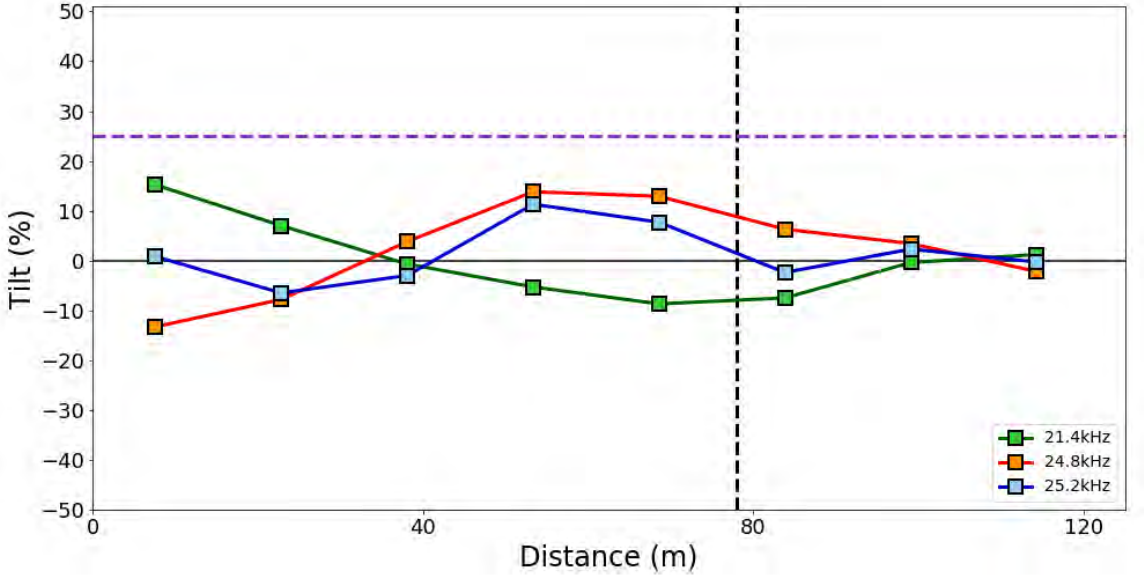

Figure 69: Fraser filtered in-phase tilt components for VLF profile J across north-east trending fault zone. Same symbology and point spacing as in Figure 51.

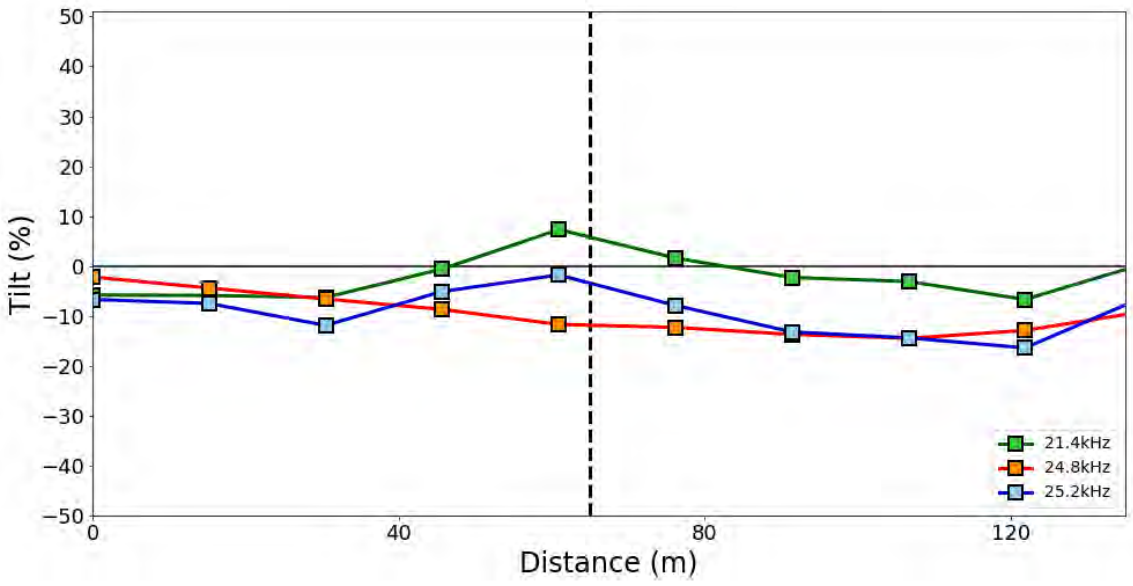

Figure 70: VLF profile K across north-east trending fault zone with the in-phase tilt components of three different frequencies collected. Same symbology and profile spacing as Figure 50.

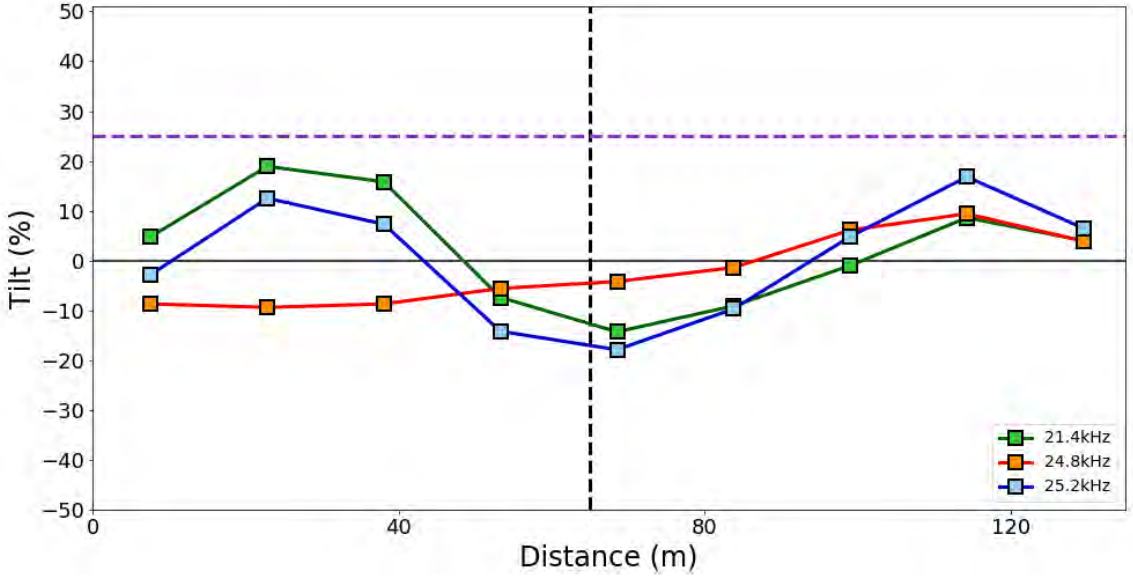

Figure 71: Fraser filtered in-phase tilt components for VLF profile K across north-east trending fault zone. Same symbology and point spacing as in Figure 51.

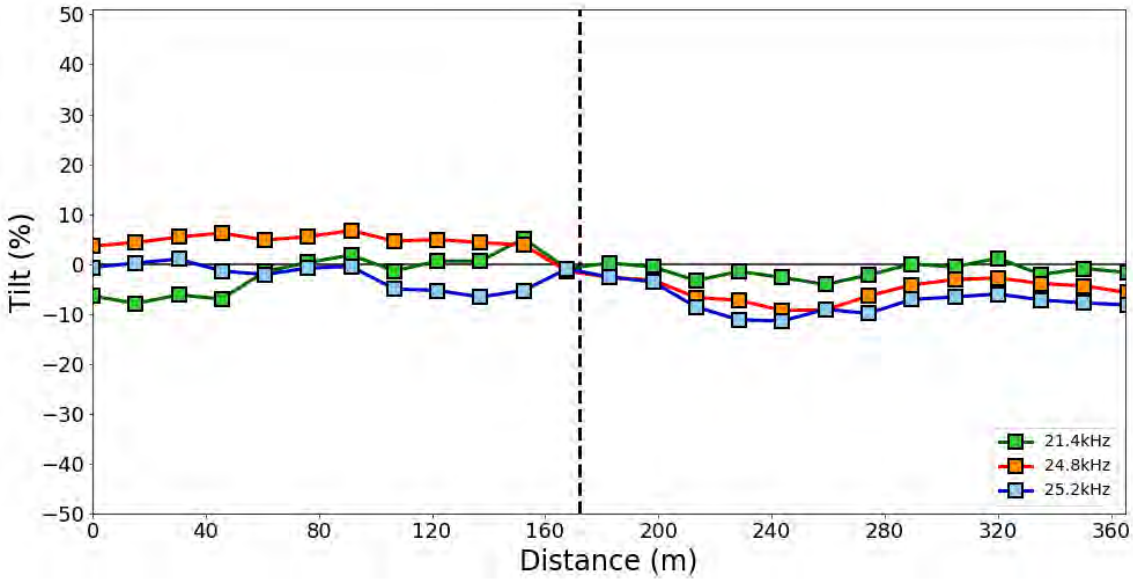

Figure 72: VLF profile L across north-east trending fault zone with the in-phase tilt components of three different frequencies collected. Same symbology and profile spacing as Figure 50.

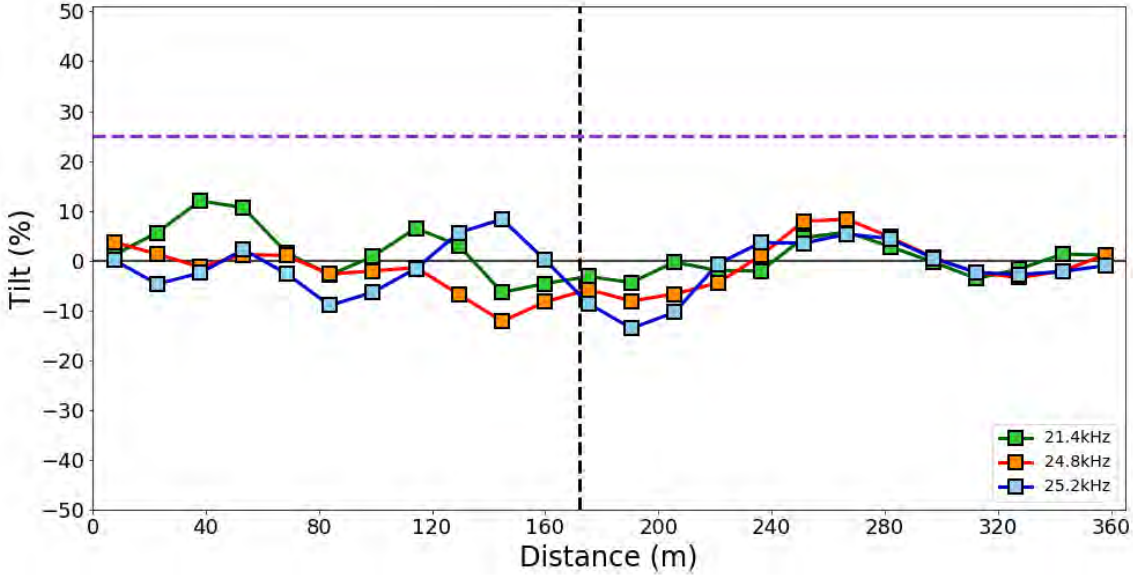

Figure 73: Fraser filtered in-phase tilt components for VLF profile L across north-east trending fault zone. Same symbology and point spacing as in Figure 51.

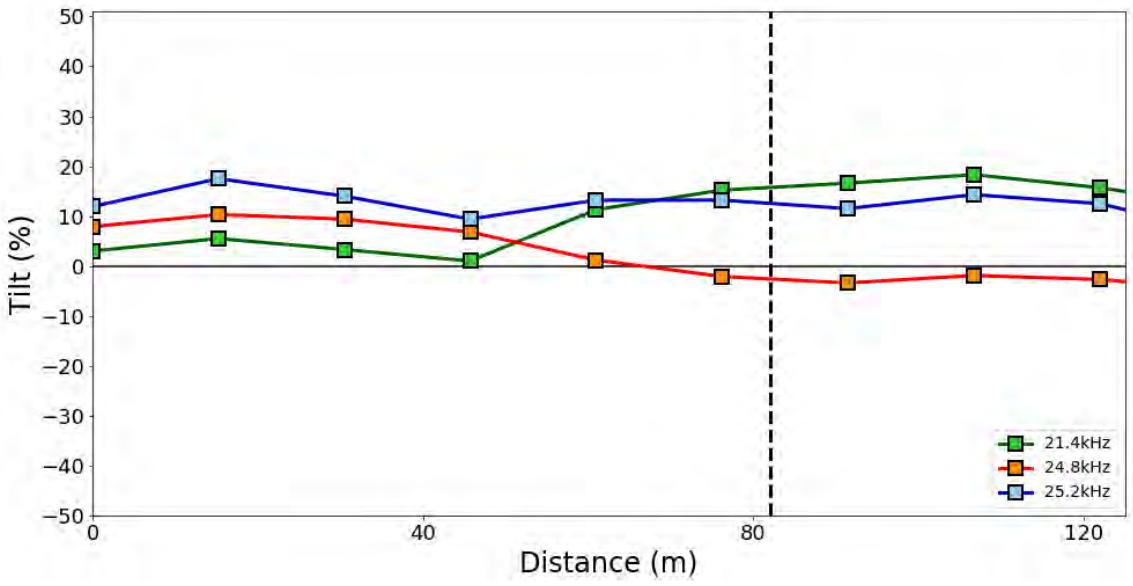

Figure 74: VLF profile M across north-east trending fault zone with the in-phase tilt components of three different frequencies collected. Same symbology and profile spacing as Figure 50.

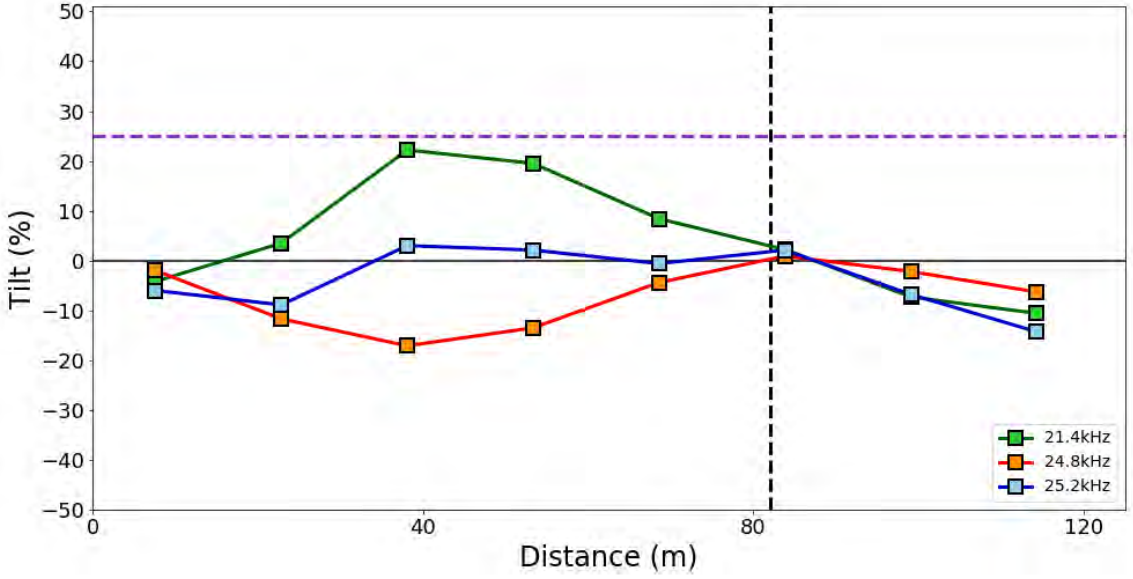

Figure 75: Fraser filtered in-phase tilt components for VLF profile M across north-east trending fault zone. Same symbology and point spacing as in Figure 51.

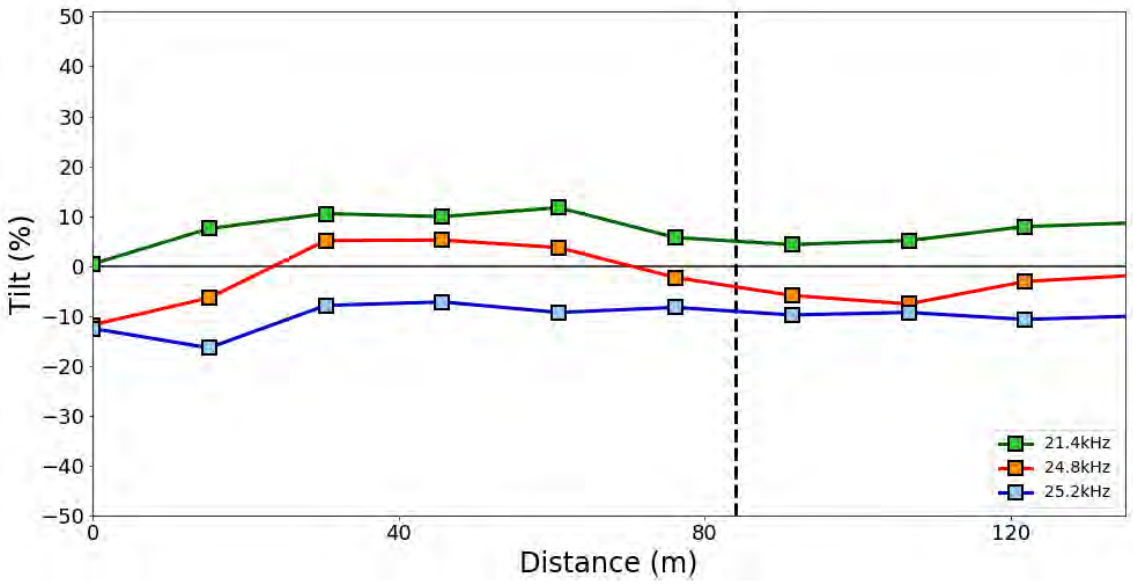

Figure 76: VLF profile N across north-east trending fault zone with the in-phase tilt components of three different frequencies collected. Same symbology and profile spacing as Figure 50.

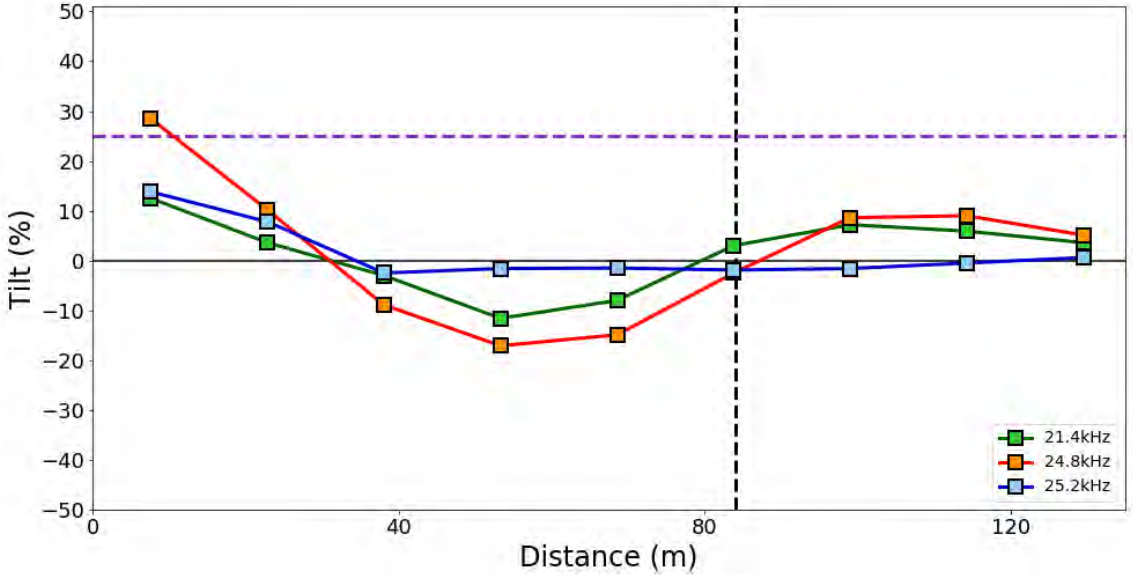

Figure 77: Fraser filtered in-phase tilt components for VLF profile N across north-east trending fault zone. Same symbology and point spacing as in Figure 51.

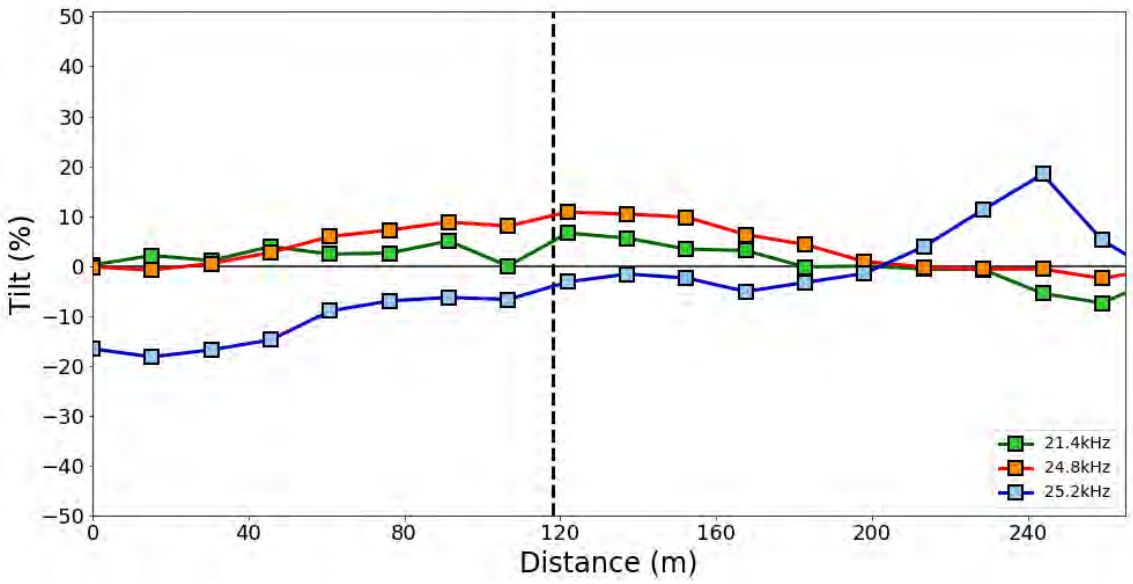

Figure 78: VLF profile O across north-east trending fault zone with the in-phase tilt components of three different frequencies collected. Same symbology and profile spacing as Figure 50.

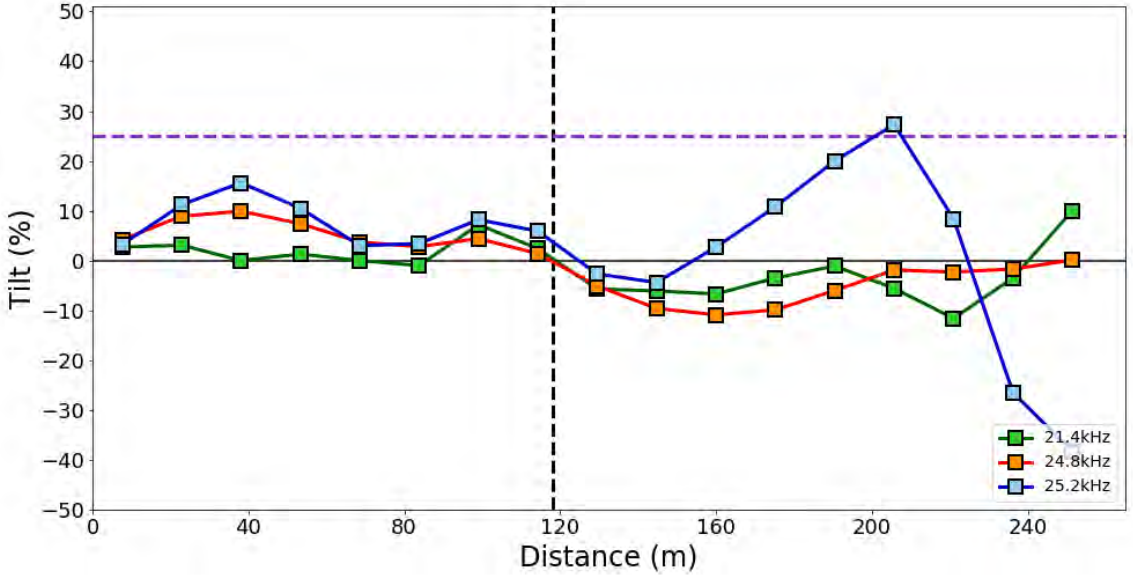

Figure 79: Fraser filtered in-phase tilt components for VLF profile O across north-east trending fault zone. Same symbology and point spacing as in Figure 51.

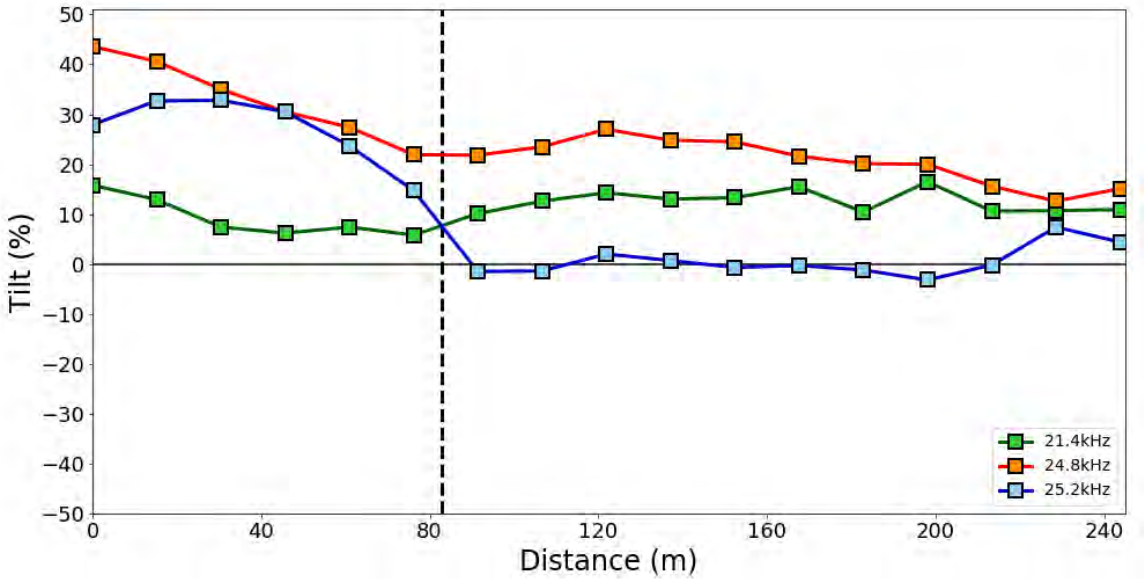

Figure 80: VLF profile P across north-east trending fault zone with the in-phase tilt components of three different frequencies collected. Same symbology and profile spacing as Figure 50.

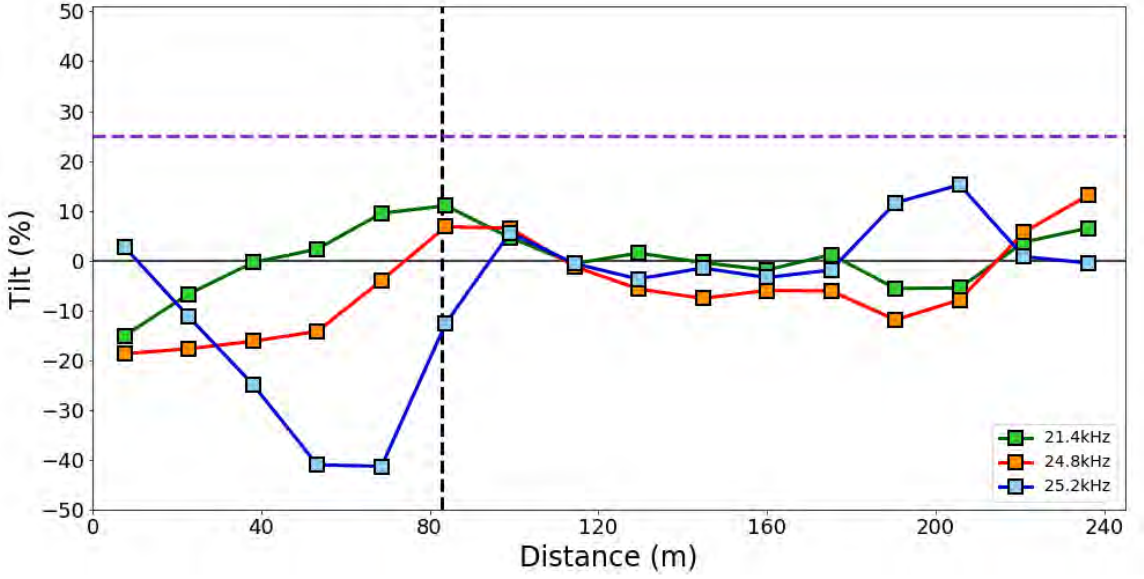

Figure 81: Fraser filtered in-phase tilt components for VLF profile P across north-east trending fault zone. Same symbology and point spacing as in Figure 51.